STUDIES OF POTENTIAL ENERGY SURFACES OF NEUTRAL, PROTONATED, NEGATIVELY CHARGED WATER CLUSTERS.

by

Tae Hoon Choi

BS, Ajou University, 1999

MS, Seoul National University, 2001

Submitted to the Graduate Faculty of

the Department of Chemistry in partial fulfillment

of the requirements for the degree of

Doctor of Philosophy

University of Pittsburgh

2010

UNIVERSITY OF PITTSBURGH

CHEMISTRY DEPARTMENT

This dissertation was presented

by

Tae Hoon Choi

It was defended on

February 18th 2010

and approved by

Kenneth D. Jordan, Chemistry Department

David Earl, Chemistry Department

Geoffrey Hutchison, Chemistry Department

Jeffry Madura, Duquesne University, Chemistry Department

Dissertation Director: Kenneth D. Jordan, Chemistry Department

STUDIES OF POTENTIAL ENERGY SURFACES OF NEUTRAL, PROTONATED, NEGATIVELY CHARGED WATER CLUSTERS.

Tae Hoon Choi, PhD

University of Pittsburgh, 2010

Analytical gradients of the OEPM-GTO (one electron polarizable model - Gaussian-type orbital) and OEPM-DVR (discrete variable representation) methods have been implemented, and used in combination with the basin-hopping Monte Carlo, doubly-nudged elastic band and eigenvector-following methods to characterize small $(H_2O)_n^-$ clusters. The self-consistent-charge density-functional tight-binding (SCC-DFTB) electronic structure method has been used in conjunction with the basin hopping Monte Carlo method to optimize low-lying minima of $(H_2O)_8$, $H^+(H_2O)_{21}$, and $H^+(H_2O)_{22}$. In addition, parallel-tempering Monte Carlo simulations were used to characterize the finite temperature behavior of the $(H_2O)_8$ cluster.

TABLE OF CONTENTS

LIST OF TABLES

LIST OF FIGURES

PREFACE

First, I thank Prof. Kenneth D. Jordan for his excellent mentorship. Five years is not long enough to learn all he has to teach. To the members of the Jordan Group, I thank you for all your help and encouragement these last five years. Also, I thank my parents and sisters for their tireless support of all my endeavors. Finally, I thank god for giving me hope in my life.

1.0 INTRODUCTION

Negatively charged, neutral, and protonated water clusters have been the subject of numerous theoretical studies. [1, 2, 3, 4, 5, 6, 7, 8, 9, 10, 11, 12, 13, 14, 15, 16, 17, 18, 19, 20, 21, 22, 23, 24, 25, 26, 27, 28, 29, 30, 31, 32, 33, 34, 35, 36, 37, 38, 39, 40, 41, 42, 43, 44, 45, 46, 47, 48, 49, 50, 51, 52, 53, 54, 55, 56, 57, 58, 59, 60, 61, 62, 63, 64] The research presented in this dissertation focuses on the study of the potential energy surfaces (PES) of $(H_2O)_n^-$ cluster systems, the finite temperature behavior of the $(H_2O)_8$ cluster, and the low-lying energy minima of the $H^+(H_2O)_{21}$ and $H^+(H_2O)_{22}$ clusters.

The one electron polarization model (OEPM) [33] has been employed for investigating the PESs of small water cluster anions. This model is close related to our earlier Drude-model approach for $(H_2O)_n^-$ cluster systems, [65, 27, 28, 29, 30, 31, 32] and the total energy is given by the sum of the energy of the neutral water cluster as described by the distributed point polarizable site (DPP) water model [66] and the electron binding energy (EBE), calculated using a one-electron Hamiltonian including explicit polarization of the water monomers by the excess electron. The methodology involved in calculating analytical gradients of $(H_2O)_n^-$ clusters described by the OEPM-GTO method is presented.

This approach is applied to characterize the local minima and transition states of $(H_2O)_n^-$, $n = 6$, 7, and 8 using a combination of the basin-hopping Monte Carlo, [67, 34, 68] doubly-nudged elastic band [69, 70] and eigenvector-following methods. [71, 72] These results are then used to represent the potential energy landscapes in terms of disconnectivity graphs. [73, 74, 75] These clusters have been chosen for study because they have been characterized experimentally by means of vibrational predissociation spectroscopy. [10, 13, 14] Interestingly,

$(H_2O)_6^-$ and $(H_2O)_7^-$ appear in high intensity in $(H_2O)_n^-$ mass spectra, while $(H_2O)_8^-$ is either absent or very low intensity. [14] A large number of theoretical studies have characterized selected local minima for these clusters, [15,16,17,18,19,20,21,22,23,24,25,26,27,28,29,30,31,32] but only a few of studies for rearrangement pathways have been investigated up to this time, which has restricted analysis of the experimental observations. The implications of the minimum energy pathways for the experimental studies of these clusters are discussed.

For large systems, the energy and gradient evaluations of the OEPM method using GTO basis sets are computationally demanding. For such systems there are significant advantages to using a discrete variable representation (DVR) grid basis set. [76,77,78,79,80,81,82,83,84,85,86,87,88,89,90] Our group has implemented a DVR version of the OEPM code. As part of this thesis research analytical gradients of the DVR approach have been implemented. Calculations on $(H_2O)_6^-$ and $(H_2O)_{45}^-$ clusters are used to decide the optimal box size and grid spacing for the OEPM-DVR approach. The computational times for the DVR- and GTO-based approaches are compared.

The self-consistent-charge density-functional tight binding (SCC-DFTB) method [91,92,93,94,95,96,97,98,99] is applied to both neutral and protonated water clusters. This approach is comparable in computational speed to traditional semiempirical methods, but, in general, provides a more accurate description of geometries and relative energies of chemical species. The water octamer is selected as a system to test three variations of the SCC-DFTB method. This system is chosen because it has been characterized by other theoretical methods. In particular, we calculate the thermodynamic properties of the $(H_2O)_8$ cluster by using the parallel tempering Monte Carlo (PTMC) simulation method. [47,48,49] Excess protons in water play an important role in many chemical and biological processes. To test the applicability of the SCC-DFTB method for protonated water clusters, we apply it to $H^+(H_2O)_{21}$ which is of interest as it is a magic number cluster in the $H^+(H_2O)_n$ mass spectra, and also to $H^+(H_2O)_{22}$. Local minima are located using basin hopping Monte Carlo calculations. [67,34,68] The results are compared with those of density functional Becke3LYP [100] calculations.

2.0 ANALYTICAL GRADIENT FOR GEOMETRY OPTIMIZATIONS OF $(H_2O)_N^-$ CLUSTERS AS DESCRIBED BY THE OEPM-GTO MODEL

This work has been published as Ref. [101]

2.1 INTRODUCTION

The interaction of excess electrons with water clusters has been the subject of numerous experimental and theoretical studies [2,3,4,5,6,102,7,8,103,20,21,22,9,10,12,13,14,23,24,25,26]. Recently, our group has derived [33] a family of one-electron polarization models for $(H_2O)_n^-$ cluster systems by applying an adiabatic separation to our previously introduced quantum Drude model [65,27,28,29,30,31,32]. In the polarization model, the total energy of a $(H_2O)_n^-$ cluster is given by the sum of the energy of the neutral water cluster as described by the distributed point polarizable site (DPP) water model [66] and the electron binding energy (EBE) calculated using a one-electron Hamiltonian including explicit polarization of the water monomers by the excess electron.

To date, analytical gradients have not been presented for the Drude or associated polarization potential approaches. As a result, geometry optimization using these approaches have been carried out numerically, and simulations have been carried out using the Monte Carlo rather than molecular dynamics algorithms [65, 27, 28, 29, 30, 31]. For optimizing the geometries and for carrying out simulations of the dynamics of large $(H_2O)_n^-$ clusters, analytical gradients are required. In this work, we present the expressions for analytical gradients

of the PM1 polarization model [33] and apply these to optimize the geometries of clusters as large as $(H_2O)_{45}^-$.

2.2 THEORY

In the PM1 model, the energy of the anion is given as the sum of the energy of the neutral water cluster plus the electron binding energy obtained from a model Hamiltonian. The DPP water model employed in the PM1 model employs three point charges, three atom-centered, mutually interacting point polarizable sites, damped dispersion interactions between O atoms, and exponential repulsive interactions between atoms of different monomers. The model Hamiltonian for the excess electron includes interactions of the electron with the three-point charges, the induced dipoles resulting from water-water induction, and monomer-centered short-range repulsive potentials. In addition, the Hamiltonian includes terms that allow for the polarization of the water monomers by the excess electron.

2.2.1 Model Hamiltonian

The model Hamiltonian for an excess electron interacting with a water cluster is given (in atomic units) by

$$\mathbf{H} = -\frac{1}{2}\nabla^2 - \sum_i \frac{Q_i}{r_i} + \sum_j \frac{\boldsymbol{\mu}_j \cdot \mathbf{r}_j}{r_j^3} f_{ind}(r_j) + V_{rep} - \sum_j \frac{\alpha}{2r_j^4} f_{pol}(r_j), \tag{2.1}$$

where the second and third terms correspond to the interactions of the electron with the DPP point charges and the induced dipoles from intermolecular induction, respectively, the fourth term accounts for the short-range repulsive interactions of the excess electron with each monomer, and the last term incorporates the polarization of the monomers by the excess electron. For water the polarizability is approximately isotropic, and the experimental value 1.45 Å^3 of the isotropic polarizability of water is employed in Eq. (2.1). The electron-water

polarization is described by point polarizable centers located at the M site of each monomer (The M site is located on the rotational axis, and displaced 0.25 Å from the O atom toward the H atoms). In Eq. (2.1) μ_j is the induced dipole moment located at the M site of the j^{th} molecule and obtained by a vector sum of the three atom-centered induced dipole moments on the monomer resulting from the electronic field from the other monomers. It should be noted that the "collapse" of the three induced dipoles on each monomer to a single dipole is not essential, and is made simply for computational speed. $f_{ind}(r_j)$=1−exp($-b_1 r_j^2$) and $f_{pol}(r_j)$=(1−exp($-b_2 r_j^3$))^2 are factors that damp the short-range interactions of the excess electron with the induced dipoles (due to intermolecular induction) and polarizable sites, respectively. The damping is required to remove the r → 0 divergences in the resulting integrals. The calculated energies are relatively insensitive to the precise functional forms of the damping factors. V_{rep} is constructed using the procedure of Wang and Jordan [28] which closely follows the approach of Schnitker and Rossky [104]. The excess electron is described using a set of s and p Gaussian-type functions, both monomer-centered and floating, with the latter being located at the center of mass of the cluster.

2.2.2 Analytical Gradient of OEPM method

The analytical gradient of the energy assoicated with a closed-shell Hartree-Fock wave-function can be written as [105]:

$$\frac{\partial E}{\partial R} = \sum_{\mu v} P_{\mu v} \frac{\partial H_{\mu v}^{core}}{\partial R} + \frac{1}{2} \sum_{\mu v \lambda \sigma} P_{v\mu} P_{\lambda \sigma} \frac{\partial \langle \mu v || \sigma \lambda \rangle}{\partial R} - \sum_{\mu v} Q_{\mu v} \frac{\partial S_{\mu v}}{\partial R}, \tag{2.2}$$

where **P** is the density matrix defined in terms of the molecular orbital coefficients,

$$P_{\mu v} = 2 \sum_{a}^{m/2} C_{\mu a} C_{va}, \tag{2.3}$$

and **Q** is the energy-weighted density matrix given by

$$Q_{\mu v} = 2 \sum_{a}^{m/2} \varepsilon_a C_{\mu a} C_{va}. \tag{2.4}$$

In Eq. (2.3) and (2.4), the sum is over the occupied orbitals and ε_a is an orbital energy. $H_{\mu v}^{core}$ is a matrix element of the one-electron core Hamiltonian,

$$H_{\mu v}^{core} = \langle \phi_\mu | - \frac{1}{2}\nabla^2 - \sum_\alpha \frac{Z_\alpha}{r_\alpha} | \phi_v \rangle, \tag{2.5}$$

and $S_{\mu v}$ is an overlap matrix element, $S_{\mu v} = \langle \phi_\mu | \phi_v \rangle$. Thus the gradient of the Hartree-Fock energy can be calculated using the molecular orbital energies and LCAO-MO coefficients, together with the derivatives of the core Hamiltonian, the overlap matrix, and the two-electron integrals, $\langle \mu v || \sigma \lambda \rangle = \langle \mu v | \sigma \lambda \rangle - \frac{1}{2} \langle \mu \lambda | \sigma v \rangle$.

For the adiabatic polarization potential model described in the previous section, only a single electron is considered explicitly, and the gradient for the ground electronic state of the excess electron may be expressed as

$$\frac{\partial E}{\partial R} = \sum_{\mu v} P_{\mu v} \frac{\partial H_{\mu v}}{\partial R} - \sum_{\mu v} Q_{\mu v} \frac{\partial S_{\mu v}}{\partial R}, \quad (P_{\mu v} = C_{\mu 1} C_{v1}, Q_{\mu v} = \varepsilon_1 C_{\mu 1} C_{v1}), \tag{2.6}$$

where the Hamiltonian matrix elements $H_{\mu v} = \langle \phi_\mu | \mathbf{H} | \phi_v \rangle$ have only one electron contributions, and only a single orbital energy and associated orbital coefficient are required. In general, there can be more than one bound excess electron state, and the subscript "1" on the orbital energy and coefficients refers to the ground anionic state. The derivative of the Hamiltonian matrix is

$$\frac{\partial H_{\mu v}}{\partial R} = \langle \frac{\partial \phi_\mu}{\partial R} | \mathbf{H} | \phi_v \rangle + \langle \phi_\mu | \mathbf{H} | \frac{\partial \phi_v}{\partial R} \rangle + \langle \phi_\mu | \frac{\partial \mathbf{H}}{\partial R} | \phi_v \rangle. \tag{2.7}$$

There are twelve derivatives associated with the x, y, z coordinates of the three atoms and of the M site, for each water molecule. The derivatives of the basis functions with respect to the coordinates associated with the M sites are zero as there are no basis functions located on the M sites. Hence the Pulay terms [106,107] only require derivatives with respect to the atomic coordinates.

The nonzero contributions to the gradients of the Hamiltonian (*i.e.*, the third term in Eq. (2.7)) are summarized in Table 1, where V_{pc} involves the interaction of the excess electron

with the point charges of the DPP water model, and V_{ind} and V_{pol} correspond to the fourth and fifth terms in Eq. (2.1).

The greatest challenge in evaluating the gradients in the PM1 model is presented by the terms involving the interaction of the excess electron with the induced dipoles resulting from intermolecular induction. This term may be expanded as

$$\begin{aligned} \langle\phi_\mu|\frac{\partial V_{ind}}{\partial R}|\phi_v\rangle &= \langle\phi_\mu|\sum_k \frac{\partial}{\partial R}\left[\frac{\mathbf{r}_k}{r_k^3}\left(1-e^{-br_k^2}\right)\right]\cdot\boldsymbol{\mu}_k|\phi_v\rangle \\ &+ \langle\phi_\mu|\sum_k \frac{\mathbf{r}_k}{r_k^3}\left(1-e^{-br_k^2}\right)\cdot\frac{\partial\boldsymbol{\mu}_k}{\partial R}|\phi_v\rangle, \end{aligned} \tag{2.8}$$

where $\mathbf{r}_k$ is the vector from the electron to the induced dipole $\boldsymbol{\mu}_k$ located on the M site associated with molecule k, and use has been made of the fact that in the current implementation of the PM1 model, the intermolecular induced dipole moment vector is independent of the electron coordinates. The derivative of the first term in Eq. (2.8) depends only on the M site, but the derivative of the induced dipole moments in the second term depends on both the atomic sites and the M site. The procedure for calculating the derivatives of the induced dipole moments is discussed in the next section.

2.2.3 Derivative of the Induced Dipole Moment

The induced dipole moment at atomic site i resulting from the interactions with the charges on the other monomers is given by [36]:

$$\boldsymbol{\mu}_i = \alpha_i\left(\mathbf{E}_i^0 + \sum_{j\neq i}\tilde{\mathbf{T}}_{ij}\cdot\boldsymbol{\mu}_j\right), \tag{2.9}$$

where $\mathbf{E}_i^0$ is the electric field at site i produced by the fixed charges on the other monomers, α_i is the polarizability of site i, and $\tilde{\mathbf{T}}_{ij}$ is the dipole tensor.

$$\mathbf{E}_i^0 = \sum_{j\neq i}\frac{q_j\mathbf{R}_{ij}}{R_{ij}^3}f_1(R_{ij}),\quad \tilde{\mathbf{T}}_{ij} = \frac{1}{R_{ij}^3}\left(\frac{3\mathbf{R}_{ij}\mathbf{R}_{ij}}{R_{ij}^2}f_2(R_{ij}) - f_1(R_{ij})\right). \tag{2.10}$$

In Eq. (2.10), $f_1(R_{ij})$ and $f_2(R_{ij})$ are damping functions used in the DPP water model. The induced dipoles are calculated iteratively.

The derivatives of the induced dipole moments are evaluated by differentiating Eq. (2.9):

$$\frac{\partial \boldsymbol{\mu}_i}{\partial R_k} = \alpha_i \frac{\partial \mathbf{E}_i^0}{\partial R_k} + \alpha_i \sum_{j \neq i} \frac{\partial \tilde{\mathbf{T}}_{ij}}{\partial R_k} \cdot \boldsymbol{\mu}_j + \alpha_i \sum_{j \neq i} \tilde{\mathbf{T}}_{ij} \cdot \frac{\partial \boldsymbol{\mu}_j}{\partial R_k}. \tag{2.11}$$

The derivatives in Eq. (2.11) could be solved iteratively, but this would require $12N$ SCF procedures, and it is computationally faster to use the inverse matrix approach, *i.e.*, rewriting Eq. (2.11) as

$$\tilde{\mathbf{M}} \frac{\partial \boldsymbol{\mu}_i}{\partial R_k} = \mathbf{C}_k, \quad \frac{\partial \boldsymbol{\mu}_i}{\partial R_k} = \tilde{\mathbf{M}}^{-1} \mathbf{C}_k \tag{2.12}$$

where, $\mathbf{C}_k$ is $9N$ component vector, and $\tilde{\mathbf{M}}$ is a $9N \times 9N$ matrix:

$$\tilde{\mathbf{M}} = \begin{pmatrix} -1 & 0 & 0 & \alpha_1 T_{12xx} & \alpha_1 T_{12xy} & \alpha_1 T_{12xz} & \cdots \\ 0 & -1 & 0 & \alpha_1 T_{12yx} & \alpha_1 T_{12yy} & \alpha_1 T_{12yz} & \cdots \\ 0 & 0 & -1 & \alpha_1 T_{12zx} & \alpha_1 T_{12zy} & \alpha_1 T_{12zz} & \cdots \\ \alpha_2 T_{21xx} & \alpha_2 T_{21xy} & \alpha_2 T_{21xz} & -1 & 0 & 0 & \cdots \\ \alpha_2 T_{21yx} & \alpha_2 T_{21yy} & \alpha_2 T_{21yz} & 0 & -1 & 0 & \cdots \\ \alpha_2 T_{21zx} & \alpha_2 T_{21zy} & \alpha_2 T_{21zz} & 0 & 0 & -1 & \cdots \\ \alpha_3 T_{31xx} & \alpha_3 T_{31xy} & \alpha_3 T_{31xz} & \alpha_3 T_{32xx} & \alpha_3 T_{32xy} & \alpha_3 T_{32xz} & \cdots \\ \alpha_3 T_{31yx} & \alpha_3 T_{31yy} & \alpha_3 T_{31yz} & \alpha_3 T_{32yx} & \alpha_3 T_{32yy} & \alpha_3 T_{32yz} & \cdots \\ \alpha_3 T_{31zx} & \alpha_3 T_{31zy} & \alpha_3 T_{31zz} & \alpha_3 T_{32zx} & \alpha_3 T_{32zy} & \alpha_3 T_{32zz} & \cdots \\ \vdots & \vdots & \vdots & \vdots & \vdots & \vdots & \ddots \end{pmatrix} \tag{2.13}$$

where N is the number of monomers, and T_{ijxx}, T_{ijxy}, T_{ijxz}, $\cdots$, T_{ijzz} are the nine elements of the dipole tensor, $\tilde{\mathbf{T}}_{ij}$. Once available, the inverse of $\tilde{\mathbf{M}}$ can be used for calculating the derivative of the induced dipole moments with respect to any degree of freedom.

The $\mathbf{C}_k$ vector is expressed as

$$\mathbf{C}_k = \begin{pmatrix} -\alpha_1 \sum_{j\neq 1} \left(\frac{\partial E^0_{1x}}{\partial R_k} + \frac{\partial T_{1jxx}}{\partial R_k}\mu_{jx} + \frac{\partial T_{1jxy}}{\partial R_k}\mu_{jy} + \frac{\partial T_{1jxz}}{\partial R_k}\mu_{jz} \right) \\ -\alpha_1 \sum_{j\neq 1} \left(\frac{\partial E^0_{1y}}{\partial R_k} + \frac{\partial T_{1jyx}}{\partial R_k}\mu_{jx} + \frac{\partial T_{1jyy}}{\partial R_k}\mu_{jy} + \frac{\partial T_{1jyz}}{\partial R_k}\mu_{jz} \right) \\ -\alpha_1 \sum_{j\neq 1} \left(\frac{\partial E^0_{1z}}{\partial R_k} + \frac{\partial T_{1jzx}}{\partial R_k}\mu_{jx} + \frac{\partial T_{1jzy}}{\partial R_k}\mu_{jy} + \frac{\partial T_{1jzz}}{\partial R_k}\mu_{jz} \right) \\ -\alpha_2 \sum_{j\neq 2} \left(\frac{\partial E^0_{2x}}{\partial R_k} + \frac{\partial T_{2jxx}}{\partial R_k}\mu_{jx} + \frac{\partial T_{2jxy}}{\partial R_k}\mu_{jy} + \frac{\partial T_{2jxz}}{\partial R_k}\mu_{jz} \right) \\ -\alpha_2 \sum_{j\neq 2} \left(\frac{\partial E^0_{2y}}{\partial R_k} + \frac{\partial T_{2jyx}}{\partial R_k}\mu_{jx} + \frac{\partial T_{2jyy}}{\partial R_k}\mu_{jy} + \frac{\partial T_{2jyz}}{\partial R_k}\mu_{jz} \right) \\ -\alpha_2 \sum_{j\neq 2} \left(\frac{\partial E^0_{2z}}{\partial R_k} + \frac{\partial T_{2jzx}}{\partial R_k}\mu_{jx} + \frac{\partial T_{2jzy}}{\partial R_k}\mu_{jy} + \frac{\partial T_{2jzz}}{\partial R_k}\mu_{jz} \right) \\ \vdots \end{pmatrix}, \tag{2.14}$$

where E^0_{ix}, E^0_{iy}, and E^0_{iz} are the components of the electric field at site i produced by the fixed charges, and μ_x, μ_x, and μ_x are the components of the induced dipole moments, $\boldsymbol{\mu}$.

In the paper of Sommerfeld *et al*. [33] four different polarization potentials were presented. In this work we have adopted the PM1 model in which the undamped polarization potential terms are of the form $\alpha/2r_k^4$. The integrals involving the $\alpha/2r_k^4$ operator cannot be done analytically. To overcome this difficulty, the polarization operator associated with each monomer, including the associated damping factor, can be least squares fit to Gaussian-type functions (GTF) centered at the M site to give [33]:

$$V_{pol} \simeq -\sum_k a_k \mathrm{GTF}_k, \tag{2.15}$$

where the a_k are the coefficients of the fit. The analytical derivatives of this term are straightforward to evaluate. In Ref. [33] the fit made use of six d-type Gaussians. This fit, together with a smaller three s-type Gaussian fit, will be used in the calculations presented in this paper. Moreover, because the polarization potentials in the four polarization models of Ref. [33] are all fit to GTF's, the gradient program works without change with all four models.

2.2.4 Treatment of Constraints

The present implementation of the PM1 electron-water model is based on the DPP rigid monomer water model. Although Euler angle coordinates are commonly used for maintaining the geometrical constraints in such models, we have opted instead to use Cartesian coordinates in evaluating the gradients both due to the difficulties posed by the M site for an Euler angle representation and because of our plans to transition to a flexible monomer model in the future. The rigid monomer constraints were then imposed by transforming the derivatives from Cartesian coordinates to the Euler angle coordinates, ϕ, θ, and ψ.

For a given monomer, the derivatives in Euler angle coordinates corresponding to the translations are associated with the sum of the derivatives in Cartesian coordinates of the various atomic sites. The derivatives for the rotations in Euler angle coordinates are described by using the torque vector with respect to the centers of mass (CM) of the monomers [108].

$$\boldsymbol{\tau}_i = \Delta\mathbf{R}_{\mathrm{O}_i} \times \mathbf{F}_{\mathrm{O}_i} + \Delta\mathbf{R}_{\mathrm{H1}_i} \times \mathbf{F}_{\mathrm{H1}_i} + \Delta\mathbf{R}_{\mathrm{H2}_i} \times \mathbf{F}_{\mathrm{H2}_i} + \Delta\mathbf{R}_{\mathrm{M}_i} \times \mathbf{F}_{\mathrm{M}_i} \tag{2.16}$$

where, $\mathbf{F}_{\mathrm{O}}$, $\mathbf{F}_{\mathrm{H}}$, and $\mathbf{F}_{\mathrm{M}}$ represents the forces at a O, H atoms, and the M site, respectively, and $\Delta\mathbf{R}_{\mathrm{O}_i}$ is the displacement vector given by $\mathbf{R}_{\mathrm{O}_i}$ - $\mathbf{R}_{\mathrm{CM}_i}$, with $\Delta\mathbf{R}_{\mathrm{H1}_i}$, $\Delta\mathbf{R}_{\mathrm{H2}_i}$, and $\Delta\mathbf{R}_{\mathrm{M}_i}$ being calculated in an analogous manner. The derivatives with respect to ϕ, θ, and ψ are then given by

$$\begin{pmatrix} \dfrac{\partial E}{\partial R_{i\phi}} \\ \dfrac{\partial E}{\partial R_{i\theta}} \\ \dfrac{\partial E}{\partial R_{i\psi}} \end{pmatrix} = \begin{pmatrix} 0 & 0 & 1 \\ -\sin\phi & \cos\phi & 0 \\ \sin\theta\cos\phi & \sin\theta\sin\phi & \cos\theta \end{pmatrix} \begin{pmatrix} -\tau_{ix} \\ -\tau_{iy} \\ -\tau_{iz} \end{pmatrix} \tag{2.17}$$

2.3 PERFORMANCE

In implementing the gradients of the PM1 model, care was taken to identify contributions that are zero or are related to other contributions, and to exploit this information to minimize the computational time. In order to check the efficiency of the analytical gradient code, it is instructive to compare timings with those for numerical evaluation of the gradients. The numerical gradients were evaluated both in a "brute force" manner which requires $12N$ times more CPU time than a single-point energy evaluation, and by a "modified" implementation that evaluates only those integrals that are changed upon specific displacements. It should be noted that numerical geometry optimizations in most *ab initio* electronic structure codes require $9N$ times more CPU time than single-point energy calculations as all integrals are evaluated for each atomic displacement.

Fig. 1 compares the computational time to calculate numerically and analytically the gradients for several water cluster anions. For a $(H_2O)_{16}^-$ cluster, the evaluation of the gradient analytically is roughly nine times faster than the "brute force" numerical gradient and three times faster than the modified numerical gradient For the $(H_2O)_{45}^-$ cluster, analytical evaluation of the gradient is fifty times faster than the "brute force" numerical gradient and about five times faster than using the modified numerical evaluation of the gradient. With this speedup, optimization of the geometries of various isomers of a cluster the size of $(H_2O)_{45}^-$ can be rapidly accomplished, but with our standard Gaussian-type orbital (GTO) basis set, which employs both monomer-centered and additional functions at the center of mass, the time to evaluate the gradient is still too long to permit long-time molecular dynamics simulations. Specifically, for $(H_2O)_{45}^-$, our standard GTO basis set contains 287 primitive functions, and a single-point energy calculation takes 36 sec., and the corresponding gradient requires 393 sec. on a 2.6 GHz opteron processor. There are several strategies for reducing the CPU time required for both the energy and gradient evaluations. These include (1) using a three s GTF rather than a six d GTF fit of the polarization potentials, (2) prescreening integrals

and evaluating only these that are estimated to be greater in magnitude than some threshold, (3) combining the repulsive and polarization potential, and (4) replacing the present atom-centered basis set with a 3D grid of s Gaussians, which would eliminate the Pulay terms. Through a combination of these strategies, it should be possible to reduce the CPU time for a gradient evaluation of a cluster the size of $(H_2O)_{45}^-$ as described by the PM1 model by as much as a factor of 50, which would permit long-time MD simulations. For example, we have found that use of a 6×6×6 grid of s Gausians rather than the present monomer centered + $5s4p$ floating set of GTO's gives accurate electron binding energies for $(H_2O)_{45}^-$ while resulting in a five-fold reduction in the CPU time required for the analytical gradient compared to that required with our standard GTO basis set.

2.4 CONCLUSIONS

Analytical gradients have been implemented for the PM1 model for $(H_2O)_n^-$ clusters. The PM1 model is based on the DPP water model and allows for both intramolecular induction and polarization of the water molecule by the excess electron. The availability of analytical gradients will greatly facilitate use of the PM1 model in carrying out molecular dynamics simulations on large $(H_2O)_n^-$ clusters. When the six d GTF representation of the polarization potential is used, the derivatives involving this term are the most time-consuming part of the calculation. With the smaller three s GTF fit to the polarization potential, the most time consuming step in the gradient evaluation is due to the terms involving the interaction of the excess electron with the induced dipoles from intermolecular induction. We note also that with our standard monomer-centered basis set, about one half of the time of the gradient evaluation is due to the Pulay terms. By switching to a 6×6×6 grid of s GTF functions for the electronic basis set, the Pulay terms are eliminated and the CPU time required to evaluate the analytical gradient for a cluster the size of $(H_2O)_{45}^-$ is reduced about five fold.

With the adoption of the smaller three s GTF fit of the polarization potential and the use of the 6×6×6 grid of s GTFs for the basis set, MD simulations for tens of psec. are feasible for clusters of this size when carried out on a single CPU, and for a few nsec. when carried out in parallel.

Table 1: Nonzero derivatives of the Hamiltonian in the PM1 model for an excess electron interacting with a water cluster.

Coordinate	$\frac{\partial V_{pc}}{\partial R}$	$\frac{\partial V_{rep}}{\partial R}$	$\frac{\partial V_{ind}}{\partial R}$	$\frac{\partial V_{pol}}{\partial R}$
$R = R_{\mathrm{O}}$	0	$\frac{\partial V_{rep}}{\partial R_{\mathrm{O}}}$	$\frac{\partial V_{ind}}{\partial R_{\mathrm{O}}}$	0
$R = R_{\mathrm{H}}$	$\frac{\partial V_{pc}}{\partial R_{\mathrm{H}}}$	$\frac{\partial V_{rep}}{\partial R_{\mathrm{H}}}$	$\frac{\partial V_{ind}}{\partial R_{\mathrm{H}}}$	0
$R = R_{\mathrm{M}}$	$\frac{\partial V_{pc}}{\partial R_{\mathrm{M}}}$	0	$\frac{\partial V_{ind}}{\partial R_{\mathrm{M}}}$	$\frac{\partial V_{pol}}{\partial R_{\mathrm{M}}}$

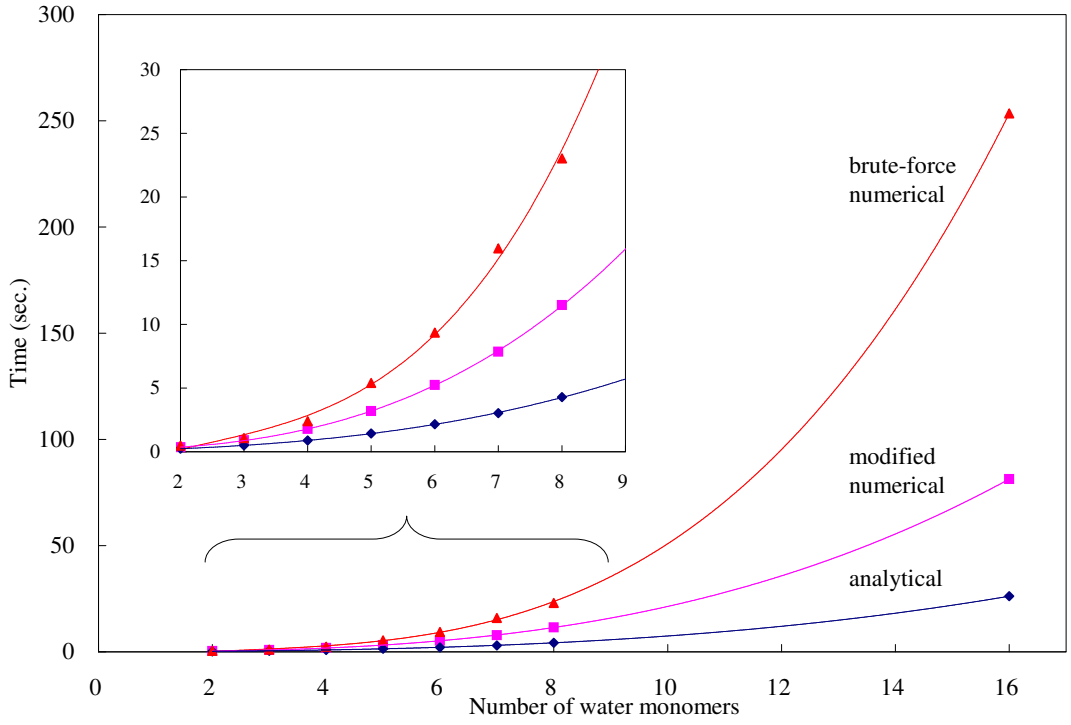

Figure 1: Time required to calculate the gradient in one optimization step for several water cluster anions as described by the PM1/DPP model. The calculations were carried out on a 2.6 GHz opteron CPU.

Table 2: CPU time to evaluate the energy and gradient of the $(H_2O)_{45}^-$ cluster

term[a]	CPU time (sec.)		
	Pulay	non-Pulay	Total
$\frac{\partial V_{NN}}{\partial R}$	N/A	0.7	0.7
$\frac{\partial S_{\mu v}}{\partial R}$	4.1	N/A	4.1
$\frac{\partial (V_{kin})_{\mu v}}{\partial R}$	12.6	N/A	12.6
$\frac{\partial (V_{pc})_{\mu v}}{\partial R}$	28.8	11.7	40.5
$\frac{\partial (V_{rep})_{\mu v}}{\partial R}$	39.0	27.8	66.8
$\frac{\partial \boldsymbol{\mu}}{\partial R}$	N/A	3.0	3.0
$\frac{\partial (V_{ind})_{\mu v}}{\partial R}$	58.0	59.2	117.2
$\frac{\partial (V_{pol})_{\mu v}}{\partial R}$	56.6	91.8	148.4[b]
Total	199.1	194.2	393.3
Energy			35.8

[a] $\frac{\partial (A)_{\mu v}}{\partial R}$ is a shorthand notation of $\langle \frac{\partial \phi_\mu}{\partial R} | A | \phi_v \rangle + \langle \phi_\mu | A | \frac{\partial \phi_v}{\partial R} \rangle + \langle \phi_\mu | \frac{\partial A}{\partial R} | \phi_v \rangle$

[b] The tabulated results are for a six d Gaussian function representation of the polarization potential. The total time to evaluate the $\frac{\partial (V_{pol})_{\mu v}}{\partial R}$ contributions is reduced from 148.4 to 31.3 sec. if a three s GTF fit is used in place of the six d GTF fit. The CPU time for the energy evaluation is reduced from 35.8 to 17.1 sec.

3.0 POTENTIAL ENERGY LANDSCAPE OF THE $(H_2O)_6^-$ CLUSTER

This work has been published as Ref. [109]

3.1 INTRODUCTION

Negatively charged water clusters have been the subject of numerous studies [1,2,3,4,5,6,7,8,9,10,11,12,13,14,15,16,17,18,19,20,21,22,23,24,25,26,27,28,29,30,31,32,33] since their discovery mass spectroscopically in 1984. [102,110] In recent years, vibrational predissociation spectroscopy [9,10,11,12,13,14] has provided considerable insight into the nature of the electron binding motifs of small $(H_2O)_n^-$ clusters, and a large number of theoretical studies [15,16,17,18,19,20,21,22,23,24,25,26,27,28,29,30,31,32,33] have characterized selected local minima for these species. However, very little is known about the pathways for interconversion between different isomers, which has hampered interpretation of the experimental data. The main obstacle to computationally mapping out isomerization pathways of $(H_2O)_n^-$ clusters has been the absence of a computationally fast, reliable method for exploring the potential energy surfaces. *Ab initio* methods cannot be used for this purpose, for any but the smallest clusters, due to the need to include electron correlation effects, preferably at the CCSD(T) level [111,112], and, at a minimum, at the MP2 level [113], together with the need to employ large, flexible basis sets.

Our group has recently introduced a one-electron polarization model (OEPM) [33] de-

rived from our earlier Drude-model approach [27] for $(H_2O)_n^-$ cluster systems. We have demonstrated that the OEPM approach gives electron binding energies and geometries of $(H_2O)_n^-$ clusters in close agreement with the results of high-level *ab initio* methods. In a subsequent publication, we described the implementation of analytical gradients for the OEPM method [101], which means that we now have the computational tools for mapping out in detail the rearrangement pathways of $(H_2O)_n^-$ clusters.

In this present study, we use the OEPM method to investigate the potential energy landscape of $(H_2O)_6^-$. This cluster has been chosen for study because it has been characterized experimentally by means of vibrational predissociation spectroscopy [10] and computationally by means of parallel-tempering Monte Carlo (PTMC) simulations. [31] In addition, it is the largest $(H_2O)_n^-$ cluster for which the neutral precursor for the dominant form of the anion observed experimentally is known. [11] A combination of techniques, described in the computational methods section, are used to locate the local minima and first-order transition states and to map out the pathways between the transition states and local minima. These results are then used to express the potential energy landscapes in terms of disconnectivity graphs. [73,74,75] The experimental results for $(H_2O)_6^-$ are discussed in light of the detailed knowledge of the potential energy surfaces gained in the present study.

3.2 COMPUTATIONAL METHODS

3.2.1 Model potential

In the OEPM approach, the total energy of the water cluster anion is given by the sum of the energy of the netural water cluster, described by the distributed point polarizable site (DPP) water model [66], and the electron binding energy (EBE) obtained from a one-electron model Hamiltonian, which includes the interactions of the excess electron with the point charges and the induced dipoles, as described by the OEPM model, as well as with

the monomer-centered, short-range repulsive and polarization potentials. [33] The excess electron is described by a basis set of diffuse s and p Gaussians, [29] and the polarization potential on each monomer is represented by a fit to a six d-type Gaussian functions centered at the M site of the DPP model to permit analytical evaluation of the resulting integrals. The OEPM model and the associated analytical gradients are described in References 33 and 39, respectively.

3.2.2 Methods used to locate the stationary points

Basin-hopping Monte Carlo simulations [67, 68, 114, 115] were used to locate a subset of the low-lying minima of $(H_2O)_6^-$. This approach combines Monte Carlo walks and gradient based optimizations to locate local minima of the potential energy surface with Monte Carlo sampling being based on the energies of the optimized minima. A modified version of the limited-memory, quasi-Newton routine (LBFGS) of Nocedal [116] was employed for the minimizations. The basin-hopping calculations were run for 4000 steps at a reduced temperature of 2.0 kJ/mol, the value used in an earlier study of protonated water clusters. [115]

The low-lying minima found in the basin-hopping Monte Carlo calculations were used to initiate searches of transition states (TS) using the doubly-nudged elastic band (DNEB) procedure, [69, 70] followed by refinement of the TSs using the eigenvector-following algorithm, [71, 72, 117, 118] with the second derivatives being calculated by finite differences of analytical first derivatives. For each TS located, the minima to which it is connected were identified by LBFGS optimizations. Whenever these optimizations located a new local minimum, it was then used to initiate new TS searches. The transition states, minima, and the pathway information were used to conduct disconnectivity graphs [73, 74, 75] which provide a compact representation of the accessibility of different portions of the potential energy surface as a function of excess energy. The optimizations were done with the OPTIM program [119] which we interfaced with our OEPM code.

3.3 RESULTS

A total of 266 minima and 469 transition states for $(H_2O)_6^-$ were located. Essentially all the transition state structures and many of the local minima are new, *i.e.*, have not been previously reported in the literature. Figure 2(a) shows the resulting disconnectivity graph of $(H_2O)_6^-$, and Figure 2(b) presents a blowup of the low-energy portion of the graph containing 41 local minima. For each minimum in Figure 2(b), the magnitude of the electron binding energy (EBE) is indicated, and the binding motif is identified as AA or non-AA, where AA denotes structures with a double-acceptor water monomer with two dangling OH groups. The double-acceptor species are especially relevant as the dominant $(H_2O)_6^-$ isomers observed experimentally fall in this class. [10, 11, 12] In addition, the minima are classified as book (BK), prism (PR), cage (CA), and open prism (OP) species. The OP isomers differ from the PR species in that they have one broken H-bond. This naming scheme follows that used in Reference 31.

For the most part, the disconnectivity graph shown in Figure 2(a) resembles a "palm tree" in the terminology of Wales. [74] For an "ideal" palm tree-type disconnective graph, efficient relaxation to the global minimum is expected. [74, 75] However, for $(H_2O)_6^-$ the two lowest energy minima, designated PR1 and CA1, are on different branches and are separated by a pathway with a overall barrier of $\sim$7 kJ/mol, which makes their interconversion difficult at low temperatures. Only three of the 41 low-lying local minima have AA structures. These are denoted as OP1-AA, OP2-AA, and BK2-AA, and have calculated EBEs in excess of 400 meV. The observed vibrational predissociation spectrum of $(H_2O)_6^-$ is due to the structurally similar OP1-AA and OP2-AA isomers (see Figure 3) which are calculated to lie energetically about 5 kJ/mol above the non-AA CA1 and PR1 isomers. The remaining 38 low-energy minima have non-AA structures with low ($\leq$ 250 meV) electron binding energies. The isomers labeled PR-N and BK-N have structures very similar to the neutral prism and book isomers, respectively, and EBEs $\leq$ 50 meV.

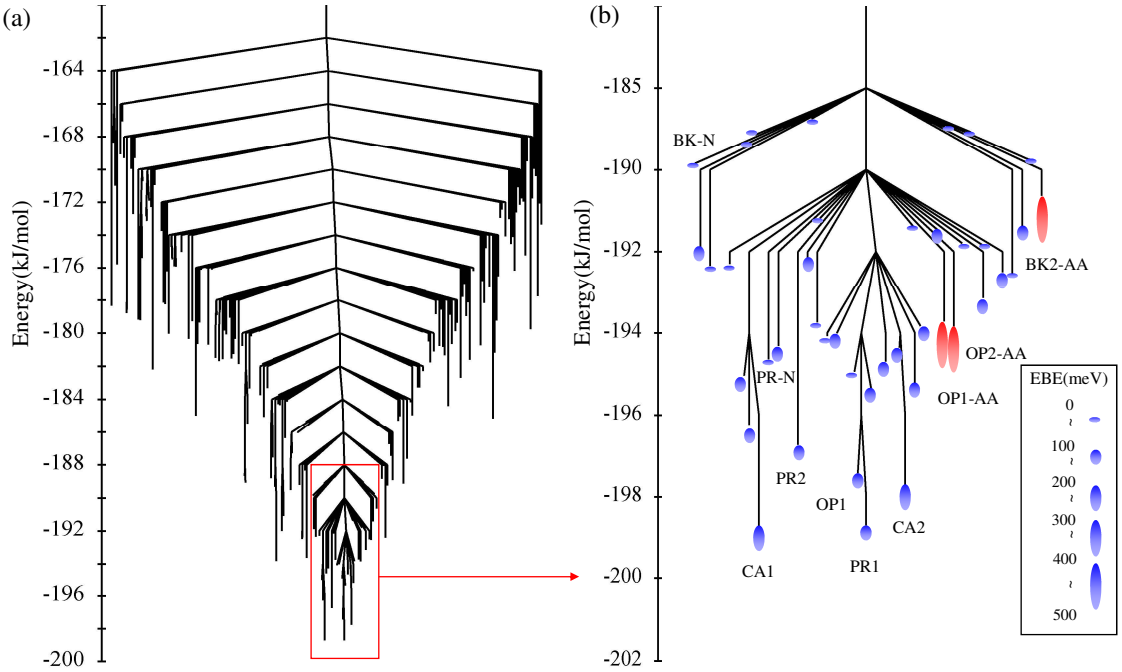

Figure 2: Disconnectivity graph of the $(H_2O)_6^-$ cluster: (a) disconnectivity graph of all stationary points identified in the work, and (b) an expanded view of the low-energy portion of the disconnectivity diagram. The oval figures indicate the magnitudes of the electron binding energies of the minima. Red and blue colors denote the AA minima and non-AA minima, respectively.

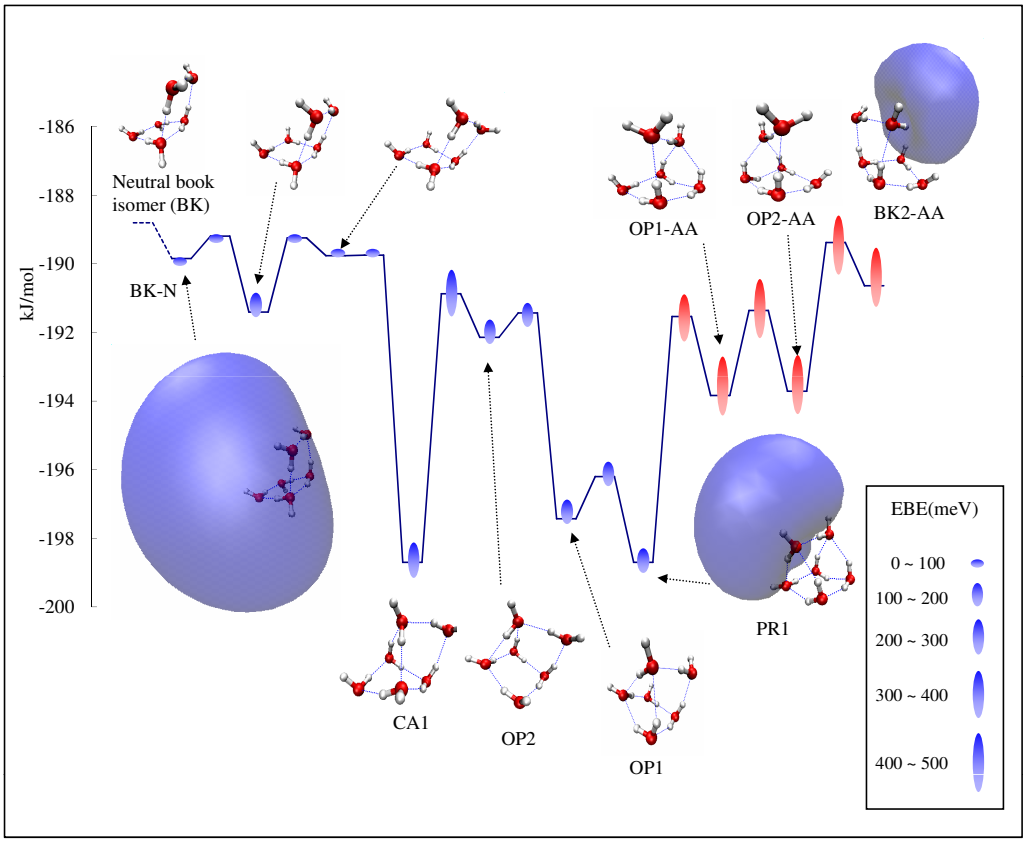

Figure 3: The lowest energy pathway between the neutral book isomer (BK) and the OP1-AA, OP2-AA, and BK2-AA isomers of the $(H_2O)_6^-$ cluster

These results raise the question as to the nature of the minimum energy pathways connecting the low-energy AA and non-AA isomers. Moreover, since experimental studies have identified the neutral book isomer as the precursor to the observed AA anions, [11] it is also of interest to examine the minimum energy pathways from the neutral book isomer plus a free electron to the low-energy AA structures. The latter pathway, shown in Figure 3, starts with a flip of a free OH group of the book form of the neutral cluster, giving the weak electron binding BK-N isomer, and then proceeds through the highly stable PR2, CA1, OP1, OP2, and CA2 non-AA species. In other words, the minimum energy pathway between the most stable AA and non-AA isomers of the anion occurs on the pathway from the neutral book to the AA species. The neutral book isomer has a dipole moment of 2.25 D and does not bind an excess electron in the OEPM model. (With a larger basis set this species would give very weak electron binding in the Born-Oppenheimer (BO) approximation [120], but probably would not bind the electron were non-BO corrections included.) The flip of one free OH group (see Figure 3), causes the dipole moment to increase to 4.01 D, and the cluster (BK-N) now weakly binds the excess electron. The overall barrier to go from BK-N isomer to the OP1-AA and OP2-AA species is calculated to be only about 1.2 kJ/mol, and is due to a flip of a second free OH group; the overall barrier to go from the OP1-AA and OP2-AA species to the OP1 and PR1 non-AA species is calculated to be only 2.5 kJ/mol.

As seen from Figure 3, OP1-AA and OP2-AA differ only in terms of which water monomer on the four-membered ring "base" is H-bonded to the AA monomer in the water "dimer" on top the tetramer. As a result, OP1-AA and OP2-AA have nearly the same energy and have very similar vibrational spectrum, and it is likely that both isomers contribute to the spectral signatures measured experimentally for the AA-type anion.

Thus far, we have focused on the pathways to go between geometrically distinct isomers of $(H_2O)_6^-$. It is also of interest to examine pathways for scrambling of water molecules within the OP1-AA and OP2-AA isomers. Such rearrangement pathways are accessible experimentally by examining isotopologues such as $[(H_2O)_5(HOD)]^-$ or $[(D_2O)_5(HOD)]^-$. [121] In Figure 4(a), we report one such pathway for OP1-AA. The lowest energy pathway

located goes through six intermediate local minima, including the highly stable PR1 and OP1 non-AA isomers. The overall activation energy for this process is calculated to be only about 3.1 kJ/mol, which means that it should be possible to drive the isomerization from OP1-AA or OP2-AA to PR1 and OP1 by excitation of an OH(OD) stretch or water bend vibration.

Given that the highly stable non-AA species are on the minimum energy pathways between the neutral book and the observed AA isomers, as well as for monomer scrambling in the low-energy AA species, it is surprising that only a small population of non-AA species is seen in the experiments of the Johnson group. [10] It may be that, following electron capture, the clusters do sample the highly stable non-AA isomers, but that the internal energies of these species are great enough that the resulting anions decay by electron ejection. This then raises the question as to how the cluster evolves from the neutral book isomer to the OP1-AA and OP2-AA isomers. The above analysis has focused on minimum energy pathways. Given the complexity of the $(H_2O)_6^-$ potential energy surface, it is anticipated that there are many higher lying pathways, some of which may bypass the stable non-AA species and be less prone to electron autoionization. One such pathway is illustrated in Figure 4(b). This specific pathway has an overall activation energy of 17.6 kJ/mol, and, interestingly, goes through the "tweezers" transition state which was first identified in the theoretical study of Kim and co-workers. [18] This particular pathway is probably not important experimentally, given the large barrier height, but is relevent as it indicates that there are indeed pathways that bypass the highly stable non-AA species.

3.4 CONCLUSIONS

In this work a one-electron polarization model was used to characterize the potential energy surface of $(H_2O)_6^-$. The minimum energy pathway proceeding from the neutral book

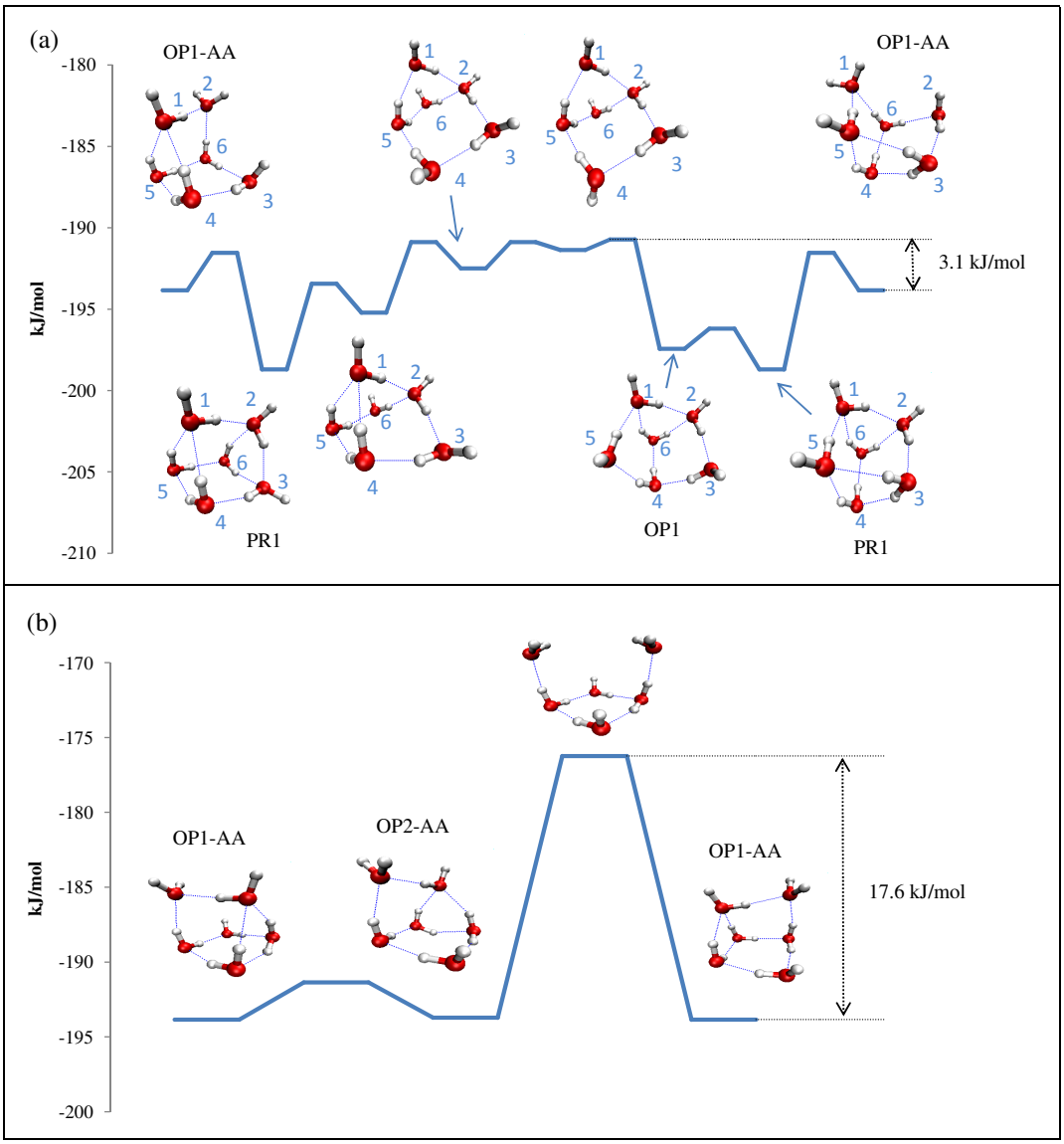

Figure 4: Energy pathways for rearranging the OP1-AA isomer. (a) lowest energy pathway located; (b) example of a pathway that bypass the highly stable non-AA isomers.

isomer to the observed AA isomers proceeds through highly stable, but weak electron binding non-AA species. Since non-AA species do not occur in high population in experimental studies, this result suggests that under experimental conditions the AA isomers may be formed via higher energy pathways that are less prone to electron detachment. Additional experimental and theoretical studies are required to establish the detailed mechanism for formation of the AA anions, as well.

4.0 POTENTIAL ENERGY LANDSCAPES OF THE $(H_2O)_7^-$ AND $(H_2O)_8^-$ CLUSTERS

Manuscript in preparation, Tae Hoon Choi and Kenneth D. Jordan.

4.1 INTRODUCTION

The accomodation of excess electrons by water clusters has been the subject of numerous experimental and theoretical studies. [1, 2, 3, 4, 5, 102, 110, 6, 7, 8, 9, 10, 11, 12, 13, 14, 15, 16, 17, 18, 122, 19, 20, 21, 22, 23, 24, 25, 26, 27, 28, 29, 30, 31, 32, 33, 101, 109, 123] Most of the theoretical work has forcussed on local minima and, with the exception of a recent study of $(H_2O)_6^-$ by our group, [109] little is known about the transition states and rearrangement pathways.

In the present study, we expand our pathway studies to include the $(H_2O)_n^-$, $n = 7$ and 8, clusters. Both of these clusters have been studied experimentally by means of vibrational predissociation spectroscopy, [13, 14] and the $(H_2O)_7^-$ has been studied computationally by means of the parallel tempering Monte Carlo (PTMC) simulations. [32] $(H_2O)_7^-$ appears in high intensity in $(H_2O)_n^-$ mass spectra, while $(H_2O)_8^-$ is either absent or very low intensity. [14] The potential energy landscapes of $(H_2O)_7^-$ and $(H_2O)_8^-$ are explored using the one-electron polarization model (OEPM) method developed in our group. [33] The local minima and transition states are characterized and used to construct rearrangement pathways and disconnectivity graphs, [73, 74] which provide a compact representation of the accessibility of different portions of the potential energy surface.

4.2 MODEL POTENTIAL AND SIMULATION METHODS

The OEPM describes the energy of a $(H_2O)_n^-$ cluster as a sum of the energy of the neutral water cluster, as described by the distributed point polarizable site (DPP) water model [66], and the binding energy of the excess electron. The electron binding energy (EBE) is calculated using a one-electron model Hamiltonian, which includes the interactions of the excess electron with the point charges and the induced dipoles of the DPP model, as well as with monomer-centered, short-range repulsive and longer ranged polarization potentials. [33] The EBEs for the OEPM are calculated using a basis sets of diffuse s and p Gaussians. [29] The polarization potential on each monomer is represented by a fit to six d-type Gaussian functions centered at the M site of the DPP model to permit analytical evaluation of the resulting integrals. The OEPM model and the associated analytical gradients have been described in Ref. 34 and 37, respectively.

Basin-hopping Monte Carlo simulations [67, 68, 114, 115] were used to locate low-lying minima. These minima were then used to initiate searches of transition states (TS) using the doubly-nudged elastic band (DNEB) procedure, [69, 70] followed by refinement of the TSs using the eigenvector-following algorithm, [71, 72, 117, 118] with the second derivatives being calculated by finite differences of analytical first derivatives. For each TS located, the minima to which it is connected were identified by LBFGS optimizations. [116] Whenever the optimizations located a new local minimum, it was then used to initiate new TS searches. The transition states, minima, and the pathway information were used to conduct disconnectivity graphs. [73, 74, 75] The optimizations were done with the OPTIM program [119] interfaced with the OEPM code.

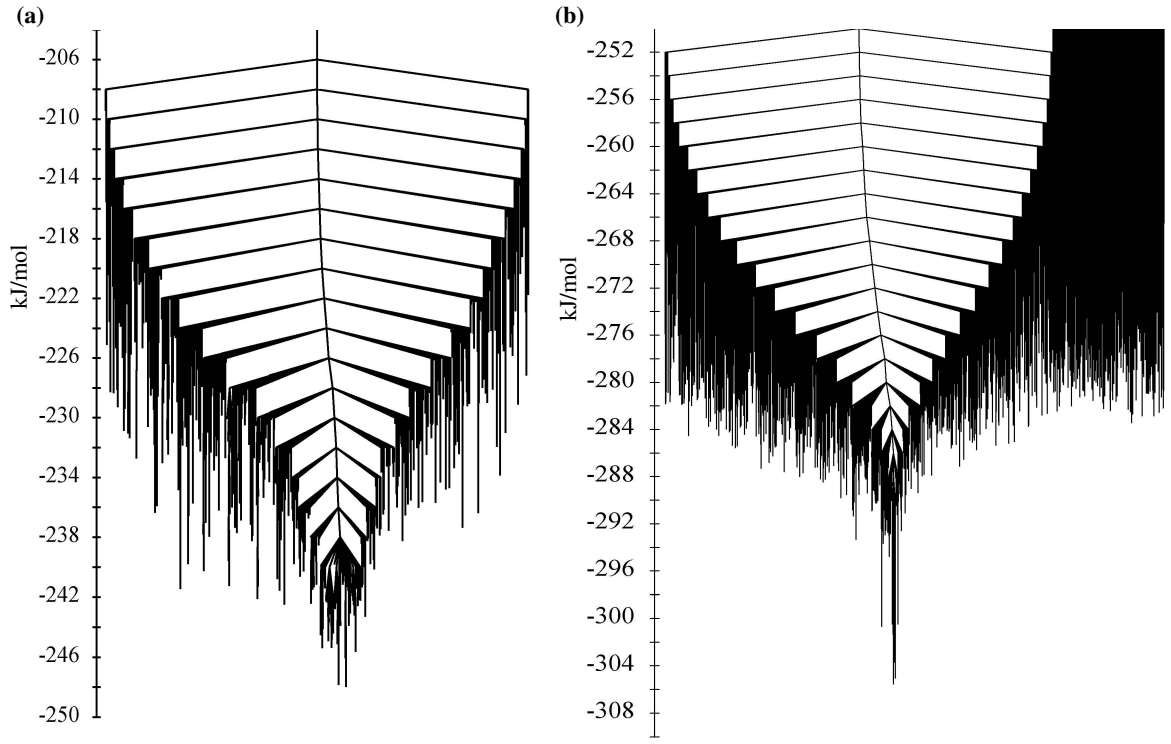

Figure 5: Disconnectivity graphs of the (a) $(H_2O)_7^-$ and (b) $(H_2O)_8^-$ clusters calculated using the OPTIM program [119] with the OEPM.

4.3 RESULTS

Fig. 5 reports the disconnectivity graphs of the $(H_2O)_7^-$ and $(H_2O)_8^-$ clusters. About 700 minima and 1200 TSs were located for the $(H_2O)_7^-$ cluster, and about 4500 minima and 6000 TSs were located for the $(H_2O)_8^-$ cluster. The low-lying portion of the disconnectivity graph of $(H_2O)_7^-$ resembles a "banyan tree", while the low-lying portion of the disconnectivity graph of the the $(H_2O)_8^-$ cluster resembles a "willow tree" in the terminology of Wales. [74] In contrast the low lying portion of the disconnectivity graph of $(H_2O)_6^-$ resembles a "palm tree". [109] The different topologies of the potential energy surfaces of these three clusters sugest that they will have very different relaxation dynamics.

4.3.1 $(H_2O)_7^-$

Fig. 6 presents a blowup of the low-energy portion of the disconnectivity graph of $(H_2O)_7^-$. This figure includes 92 minima, the lowest 80 of which have non-AA structures. For previously identified isomers, the labeling scheme used in Refs. 15 and 21 is employed. Of the twelve of AA structures, eight have been identified in the earlier theoretical studies. [122,13] The four new AA structures are labeled new1-AA to new4-AA, and are depicted in Fig. 7.

For $(H_2O)_7^-$ most of the AA structures have high electron binding energies, and most of the non-AA structures have low EBEs. However, in contrast to the $(H_2O)_6^-$ cluster, some of the low-lying non-AA structures of the $(H_2O)_7^-$ cluster have electron binding energies over 350 meV. Fig. 8 reports the structures of these isomers and the charge distributions of the excess electron. All of these structures have six or seven OH groups pointing in roughly the same direction, which results in large dipole moments and the high EBEs.

Fig. 9 reports the low-energy pathways between the two lowest-energy non-AA structures, Pr-b and Pr-c, and several low-lying AA structures. The figure also includes the lowest energy isomer of the neutral cluster. From this figure it is seen that the low energy W7pr isomer of the neutral cluster can evolve directly to a non-AA $(H_2O)_7^-$ isomer, following electron capture, from which the highly stable non-AA isomers, Pr-b and Pr-c, and several AA

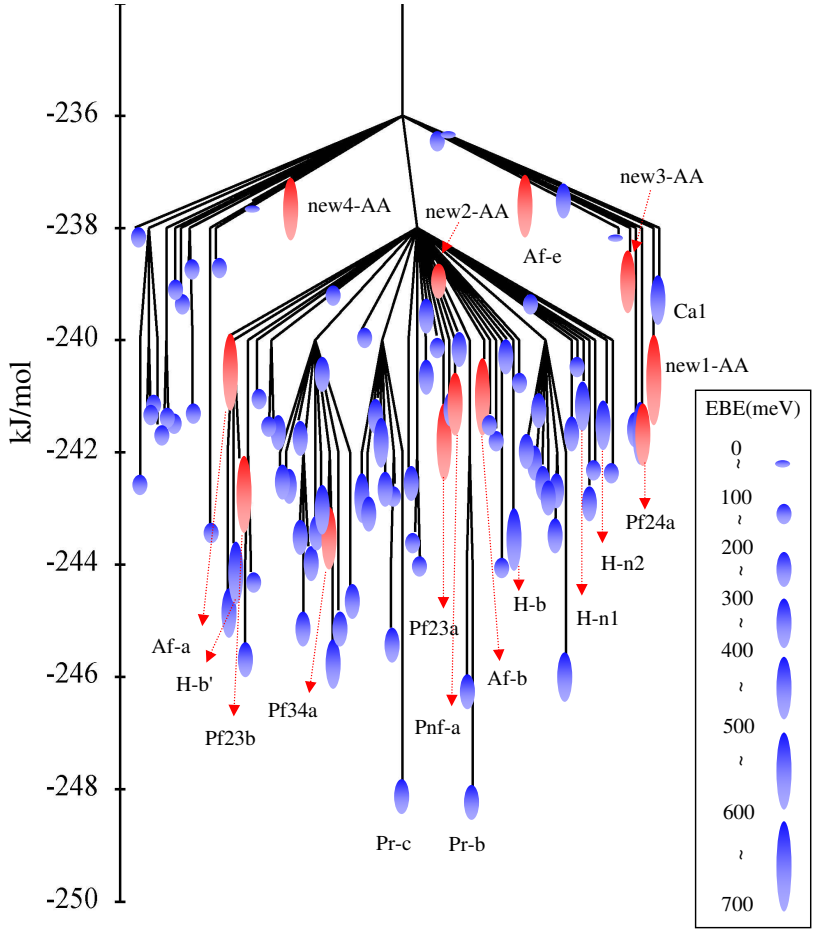

Figure 6: Low energy portion of the disconnectivity graph of $(H_2O)_7^-$. The ovals indicate schematically the magnitudes of the electron binding energies, with blue and red colors denoting the non-AA minima and AA minima, respectively.

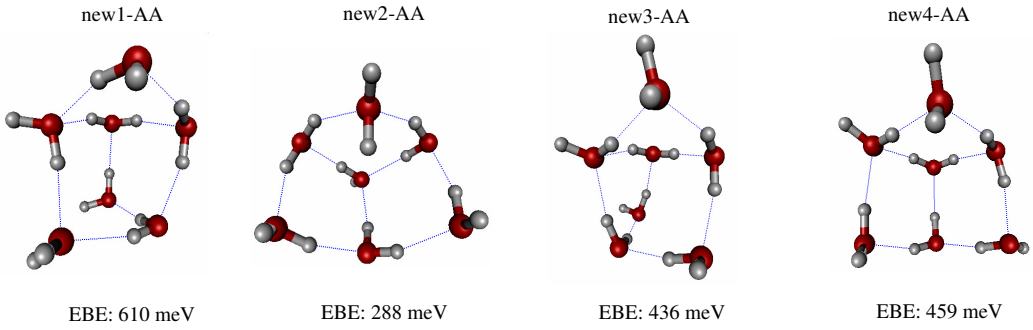

Figure 7: Four new AA structures of $(H_2O)_7^-$ and their EBEs.

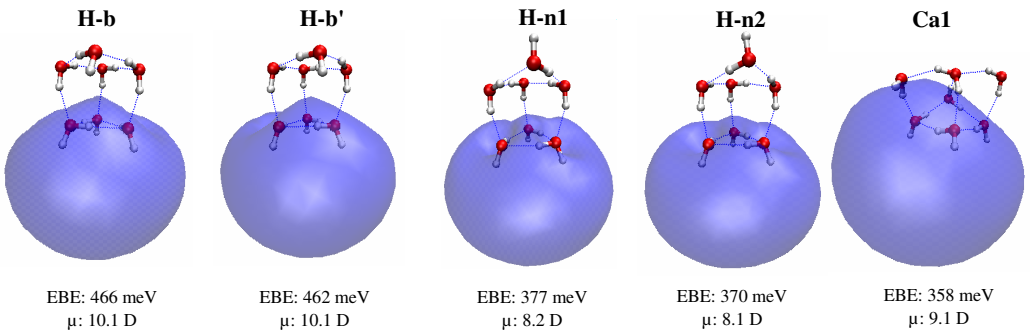

Figure 8: High EBE non-AA isomers of the $(H_2O)_7^-$ cluster. Isosurfaces containing 80% of the excess electron density are plotted. The EBEs and the dipole moments of the neutral $(H_2O)_7$ frameworks are also indicated.

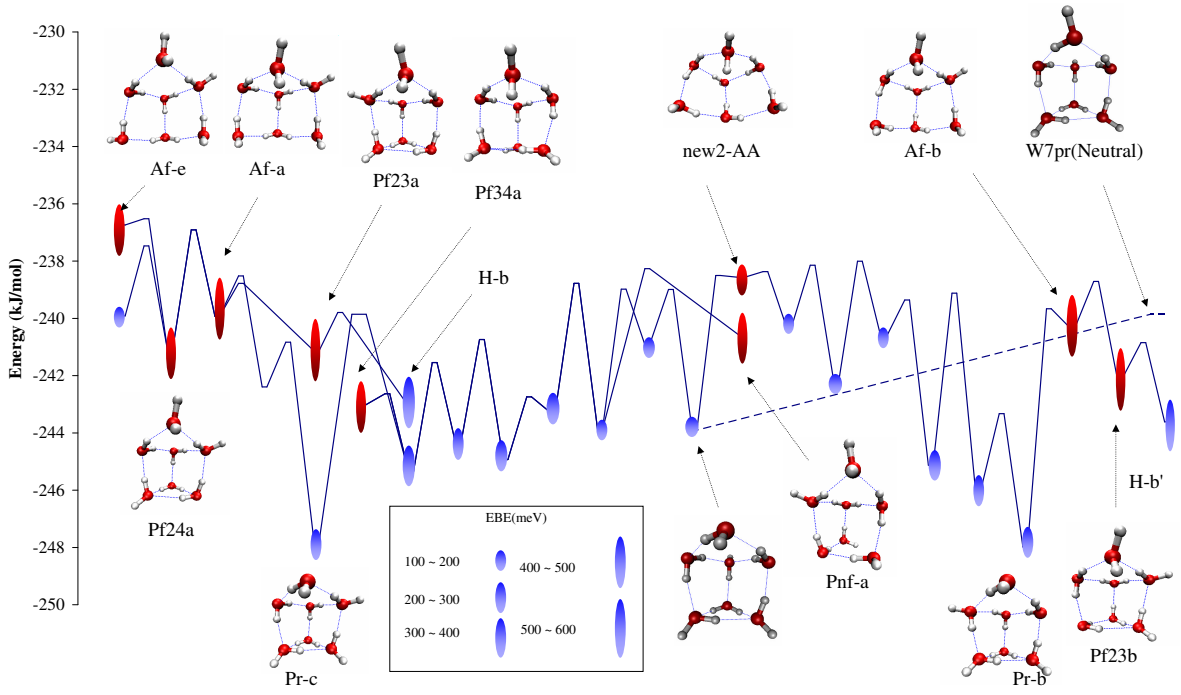

Figure 9: Low-energy pathways for rearrangements between low-energy AA and non-AA forms of $(H_2O)_7^-$. The magnitudes of the electron binding energies of the local minima are indicated schematically by ovals (red for AA and blue for non-AA). The energy of the lowest energy isomer of the neutral water cluster (W7pr) is alos indicated.

isomers are accessible with an overall activation energy of about 4.5 kJ/mol. On the other hand, an excess energy of at least 8 kJ/mol is needed to go from the low energy non-AA Pr-b and Pr-c isomers to any AA isomer of $(H_2O)_7^-$. Moreover several of the AA isomers, e.g., Pf23a, Afe, and Pf34a have very small ($\leq$ 1.5 kJ/mol) barriers to rearrangment, which suggests that they are unlikely to be observed experimentally. The Pf24a, Pnf-a, and new1-AA, AA-type isomers are trapped by barriers of over 2.3 kJ/mol, making them more likely to be observed experimentally. The lowest-energy barriers for escape from each of the twelve AA minima are summarized in Table 3.

In Ref. 15 it was proposed that Pnf-a and Pf24a are likely structures for the type I AA isomer of $(H_2O)_7^-$ observed experimentally and that Af-a is a likely candidate for the observed type I′ AA isomer. Our calculations of the activation energies for interconversion of these species are consistent with the assignment of the type I isomers. However, the calculated barrier for escaping from Af-a is only 1.1 kJ/mol, leading us to suggest that the new1-AA isomer, which has a similar EBE but a calculated activation energy for isomerization of 2.7 kJ/mol may actually be the observed I′ species.

4.3.2 $(H_2O)_8^-$

Fig. 10 reports the low-energy portion of the disconnectivity graph of $(H_2O)_8^-$. A total 168 minima are included. Interestingly, the potential energy surface of $(H_2O)_8^-$ has a branch with ten low energy non-AA cubic species which are significantly more stable than any of the other $(H_2O)_8^-$ isomers. The two lowest energy structures bind the excess electron by about 550 meV and are predicted to be about 6 kJ/mol more stable than the most stable forms of the neutral cluster, which are also depicted in the figure.

Fig. 11 reports the structures and relative energies of the ten low-energy isomers of $(H_2O)_8^-$. The three lowest energy minima are identified as Cd″, Cd, and Cdh, using the labeling scheme of Kim *et al.* [124] For the Cd″ and Cd isomers, the four dangling OH groups and four of the H-bonded OH groups all point in the same direction which results in large dipole moments and high ($\sim$ 550 meV) EBEs. The Cd isomer can be derived from the

Table 3: Energies and EBEs of the low-energy AA isomers of $(H_2O)_7^-$ and activation energies for escaping from the minima.

AA structures	Energy (kJ/mol)	Barrier (kJ/mol)	EBE (meV)
Pf24a	-241.2	3.7	422
new1-AA	-240.0	2.7	610
Pnf-a	-240.6	2.3	440
Pf23a	-241.1	1.5	563
Pf23b	-242.1	1.3	564
new3-AA	-238.4	1.2	436
Af-a	-239.9	1.1	598
Af-b	-240.3	0.7	590
Pf34a	-243.0	0.4	440
new4-AA	-237.1	0.4	459
Af-e	-236.7	0.2	465
new2-AA	-238.6	0.0	288

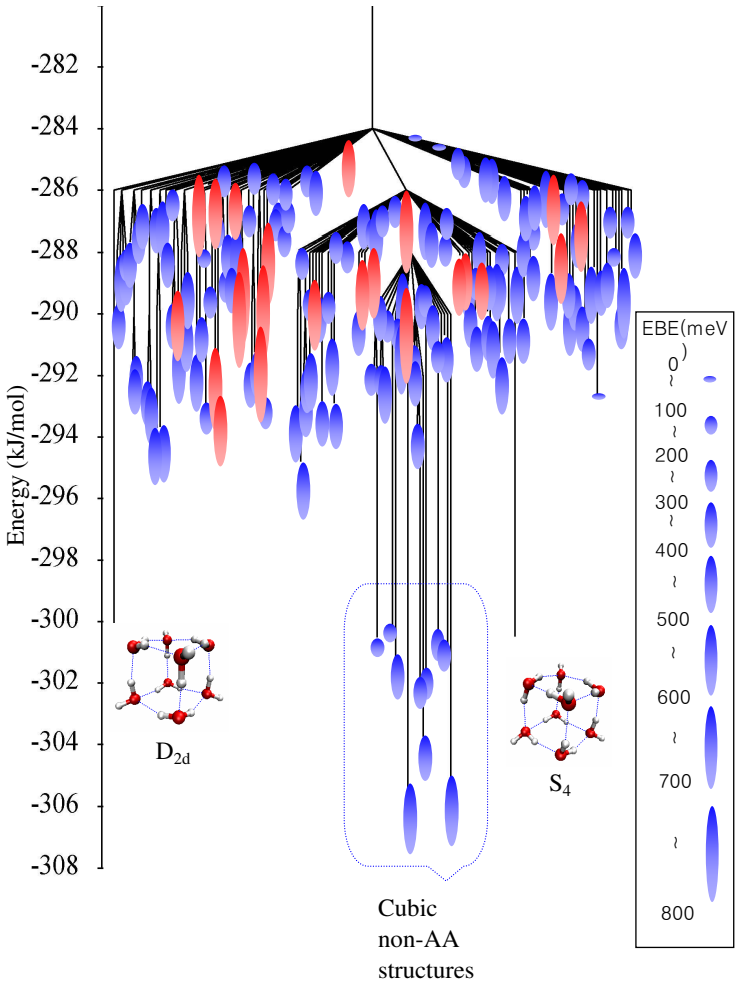

Figure 10: Low energy portion of the disconnectivity graph of $(H_2O)_8^-$. The ovals schematically indicate the magnitudes of the electron binding energies, and the blue and red colors denote the non-AA minima and AA minima, respectively. The two lowest energy isomers of the neutral cluster, which have D_{2d} and S_4 symmetry are also indicated.

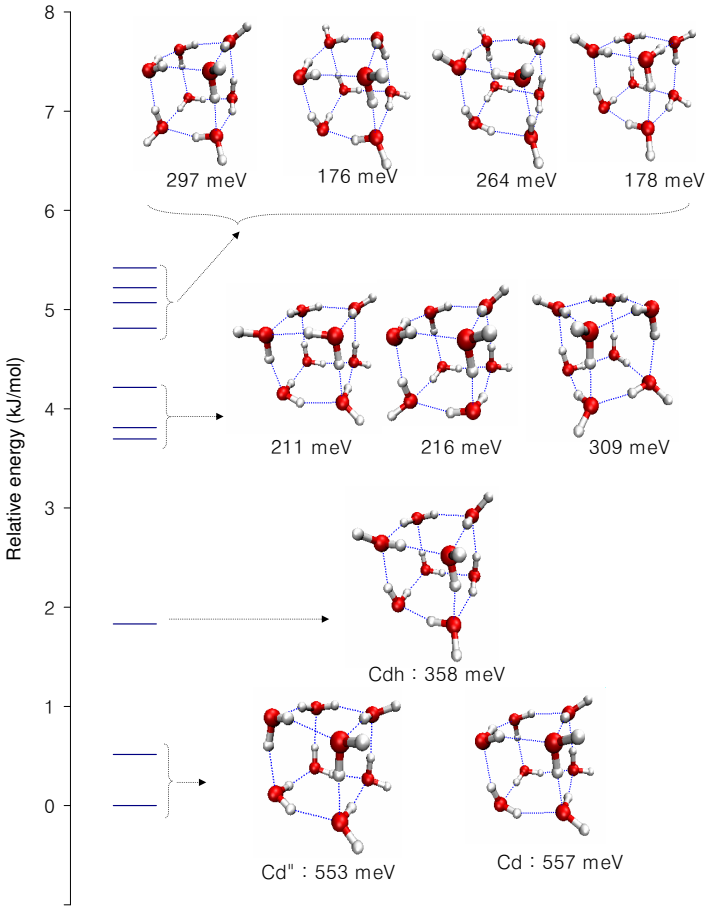

Figure 11: Structures and energies of the ten lowest energy non-AA isomers of $(H_2O)_8^-$. The EBE of each isomer is given below its structure.

S_4 neutral cluster by two donor-acceptor exchanges, while the Cd″ isomer can be derived from the D_{2d} neutral isomer by two donor-acceptor exchanges. The Cdh anion species also differs from D_{2d} neutral cluster by two donor-acceptor exchanges. (However, as discussed below, the observed $(H_2O)_8^-$ anions almost certainly result from water condensation onto $(H_2O)_7^-$ clusters.) At the MP2/aug-cc-pVDZ+diff(2sp/s) level of theory [124], the Cdh isomer is calculated to be slightly more stable than the Cd and Cd″ isomers. The MP2 calculations of Kim *et al.* predict the D_{2d} and S_4 forms of the neutral cluster to be about 12 kJ/mol below the most stable anion, while the OEPM model predicts the Cd and Cd″ anions to be about 5 kJ/mol more stable than the low-energy isomers of the neutral cluster. These differences between the OEPM and MP2 results are largely due to the neglect of high order correlation effects in the latter. High order correlation effects typically increase EBEs by 10-20%. [33] Indeed the electron binding energies (EBEs) of Cd″, Cd, and Cdh calculated using OEPM method are $0.14 \sim 0.23$ eV greater than those calculated at the MP2 level of theory.

With the OEPM, the lowest energy AA isomers of $(H_2O)_8^-$ are calculated to lie energetically about 13 kJ/mol above the Cd and Cd″ isomers. Fig. 12 depicts for $(H_2O)_8^-$ the 12 low-lying energy AA isomers which have energy barriers of at least 2 kJ/mol to rearrangement to other isomers. The EBEs of three most stable AA structures, which are labeled as OAA1, OAA2, OAA3, are about 600 meV. The second group of AA structures includes seven structures with EBEs of about 750 meV. The two highest energy AA structures energetically lie about 22 and 25 kJ/mol above the lowest energy minimum and have EBEs of about 800 meV.

Mass spectral studies reveal that $(H_2O)_8^-$ does not result from electron attachment to preexisting $(H_2O)_8$ clusters. [102,110] The reason for this is that the under the experimental conditions employed the $(H_2O)_8$ isomer distribution should be dominated by D_{2d} and S_4 isomers which have zero dipole moments and do not bind an excess electron. Indeed, it is expected that the observed AA $(H_2O)_8^-$ species result from a condensation of a water molecule onto AA isomers of $(H_2O)_7^-$. [14] In Fig. 13, we illustrate the possible pathways for forming the three lowest energy AA isomers of $(H_2O)_8^-$ by condensation of a water molecule onto

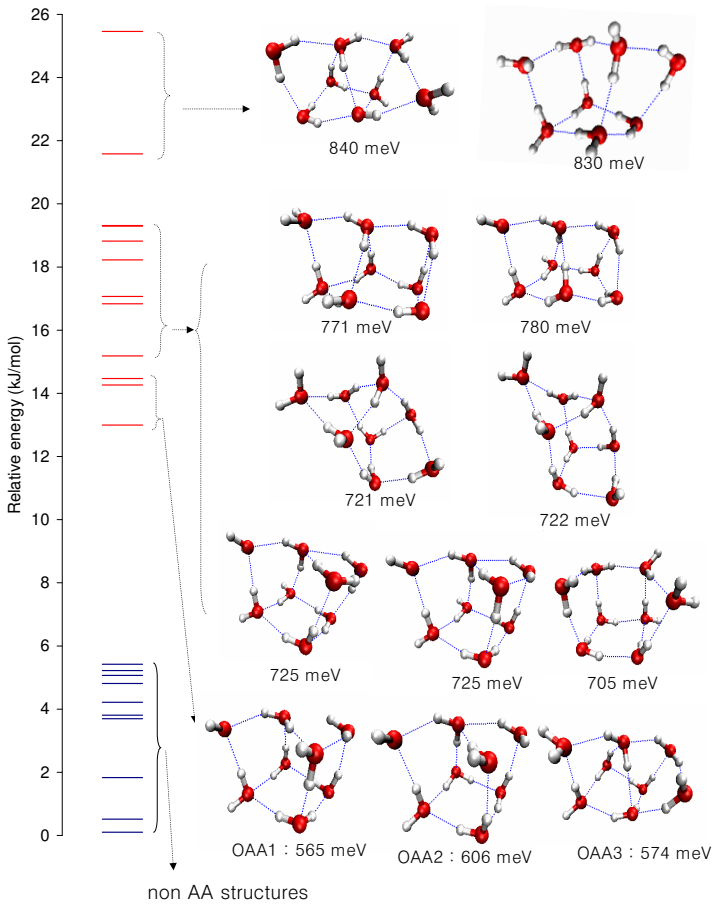

Figure 12: Structures of low energy AA isomers of $(H_2O)_8^-$ with activation energies to rearrangement greater than 2 kJ/mol. The EBE of each isomer is given below its structure.

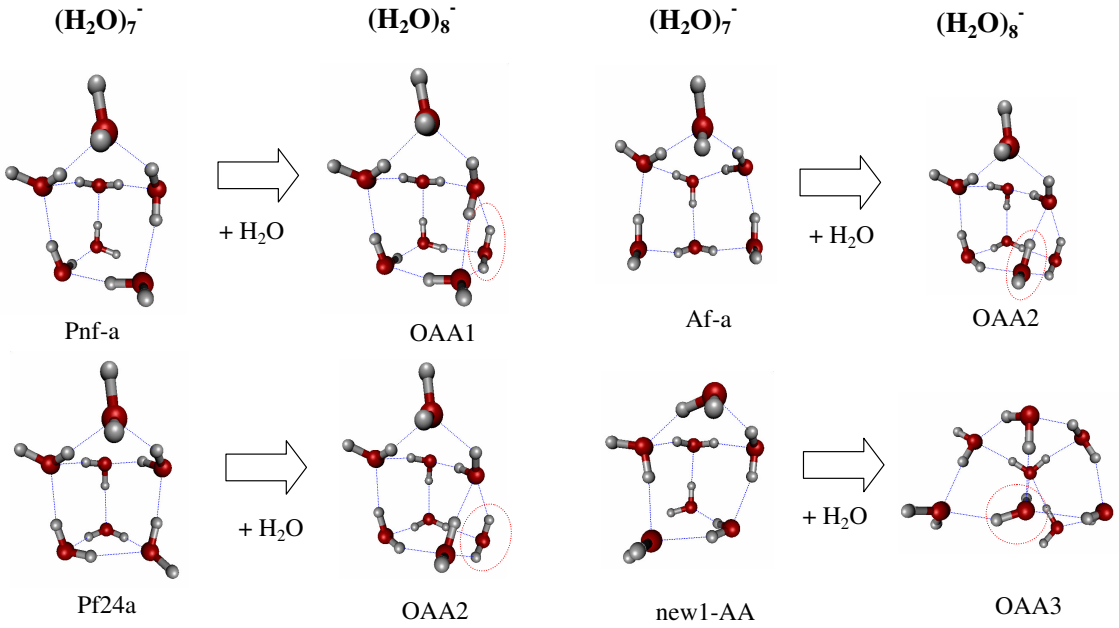

Figure 13: Pathways for forming the three lowest energy AA isomers of $(H_2O)_8^-$ by condensation of a water molecule onto the Pnf-a, Pf24a, Af-a, and new1-AA isomers of $(H_2O)_7^-$. The inserted water molecules are indicated by ellipses.

four of the $(H_2O)_7^-$ AA isomers believed to be important in the $(H_2O)_7^-$ cluster distribution.

Experimental studies of $(H_2O)_8^-$ reveal comparable populations of isomers binding the excess electron by $\sim$ 590 and 300 meV, with the former being assigned to AA and the later to non-AA species. Thus it is relevant to examine low-energy pathway connecting low energy AA and non-AA isomers of $(H_2O)_8^-$. This is done in Fig. 14 from which it is seen that the overall barriers from the OAA1 and OAA2 isomers to the Cdh and other non-AA isomers are 7-8 kJ/mol, which are far less than the energy of condenstion of a water molecule onto the low energy AA isomers of $(H_2O)_7^-$. Thus the proposed condensation processes can indeed also account for the presence of both AA and non-AA isomers in the experimental studies of Ref. 16. Specifically, the OAA1, OAA2, and OAA3 isomers of $(H_2O)_8^-$ can be formed by simple addition of a water molecule to the Pnf-a, Pf24a (or Af-a), and new1-AA isomers of $(H_2O)_7^-$, respectively. The excess energy resulting from the condensation process could drive the rearrangement to the Cdh and other non-AA isomers. Interestingly the Cdh isomer has a calculated EBE of 358 meV in good agreement with that of the weak EBE isomers observed experimentally.

4.4 CONCLUSIONS

The potential energy landscapes of the $(H_2O)_7^-$ and $(H_2O)_8^-$ clusters have been explored using the OEPM model. The low-lying potential energy minima and the transition states for isomerization have been determined. It is found that the $(H_2O)_7^-$ and $(H_2O)_8^-$ clusters, like the previously studied $(H_2O)_6^-$ cluster, have multiple non-AA isomers energetically below the most stable AA isomers. For the $(H_2O)_6^-$ and $(H_2O)_7^-$ clusters most of the non-AA isomers bind the excess electron much more weakly than do the AA isomers. However, for $(H_2O)_8^-$ the calculations predict that the lowest energy AA and non-AA have isomers comparable ($\sim$ 550 meV) electron binding energies. The high EBEs of the low-lying non-AA isomers of $(H_2O)_8^-$ are due to the the large ($\sim$ 12 D) dipole moments of the associated neutral clusters

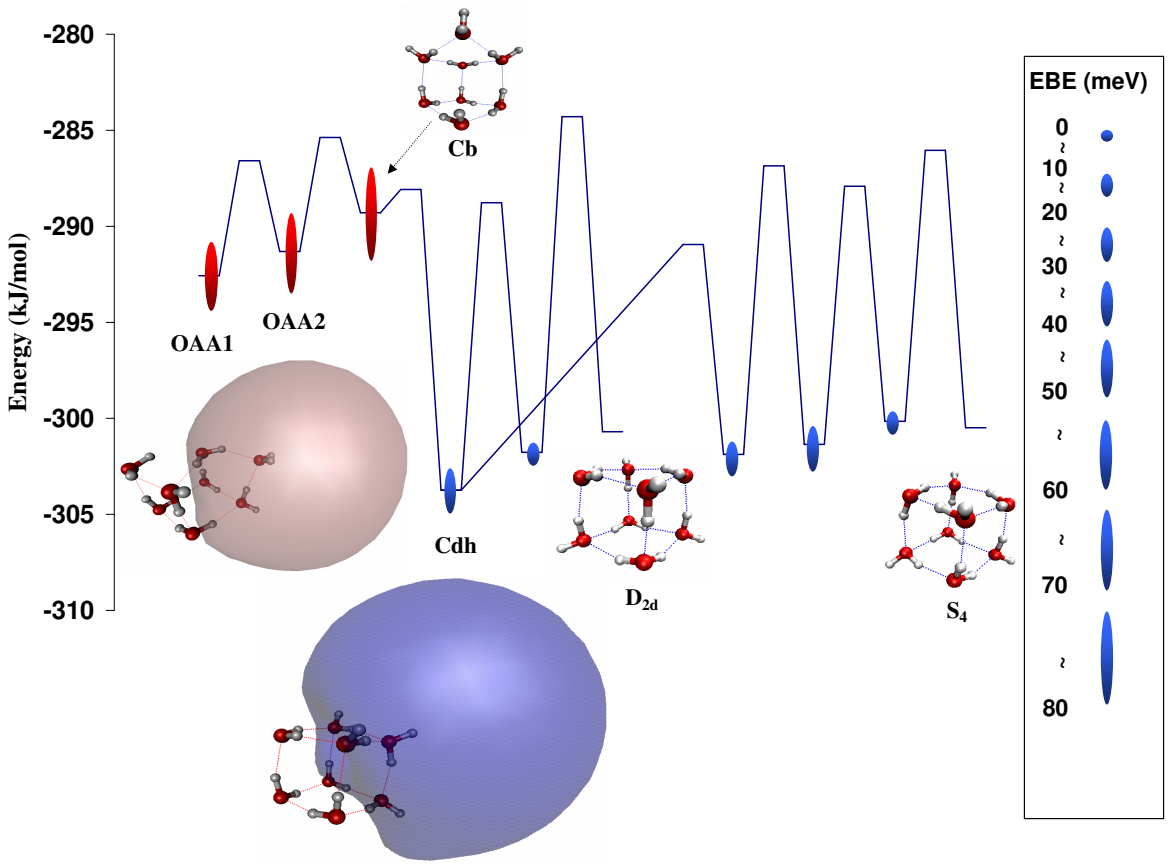

Figure 14: The lowest energy pathway from the Cdh non-AA isomer to the lowest energy AA isomers of $(H_2O)_8^-$. Pathways involving the S_4 and D_{2d} isomers of the neutral cluster are also shown even though these isomers do not bind the excess electron near their potential energy minima.

resulting from eight OH groups pointing in the same direction. These high EBE isomers appear not to have been observed experimentally.

5.0 DISCRETE VARIABLE REPRESENTATION (DVR) IMPLEMENTATION OF THE ONE ELECTRON POLARIZATION MODEL (OEPM)

Manuscript in preparation, Tae Hoon Choi, Thomas Sommerfeld, S. Levent Yilmaz, and Kenneth D. Jordan.

5.1 INTRODUCTION

The interaction of excess electrons with water clusters has been the subject of numerous experimental and theoretical studies. [1, 2, 3, 4, 5, 6, 7, 8, 9, 10, 11, 12, 13, 14, 102, 110, 15, 16, 17, 18, 19, 20, 21, 22, 23, 26, 125, 126, 104, 127, 24, 25, 27, 28, 29, 30, 31, 32, 33, 128] A key to much of the computational work in this area has been the development of the electron-water potentials for use in one-electron model Hamiltonians. [125, 126, 104, 127, 24, 25, 27, 28, 29, 30, 31, 32, 33, 128] Our group has introduced both a quantum Drude oscillator approach [27, 28] and a computationally simpler one-electron polarizable model (OEPM) [33] for describing $(H_2O)_n^-$ clusters. The GTO implementation of the OEPM model, including the evaluation of analytical gradients, has been described in earlier publications. [33, 101]

When using Gaussian type orbital (GTO) basis sets, the construction of the matrix elements $\mathbf{H}_{kl} = \int \varphi_k^*(x)\mathbf{H}\varphi_l(x)dx$ is the major time consuming part of the calculation of the energy and of the analytical gradients. We consider here an alternative approach involving the discrete variable representation (DVR) method. [76, 77, 78, 79, 80, 81, 82, 83, 84, 85, 86, 87,

88, 89, 90] Although the use of the DVR basis sets results in much larger Hamiltonian matrices, the matrix elements are rapid to evaluate, and the sparsity of the matrices allows for rapid diagonalization. In the following section, we describe the DVR implementation of the OEPM algorithm and compare its performance with the GTO implementation for $(H_2O)_n^-$ clusters with n as large as 90. We note that X and Herbert have also used a DVR approach for calculating the electron binding energies of their one-electron polarization model. [128] However, there are several differences between the two approaches, making a detailed examination of a DVR approach to our one-electron model instructive. Parallelization of the OEPM-DVR code using shared memory and OpenMP [129] is also escribed.

5.2 COMPUTATIONAL METHODS

5.2.1 DVR with the OEPM Hamiltonian

The OEPM method is built on top of the DPP water model developed in our group. [66] In this model each water monomer carries three point charges, $+q$ at each H atom and -2q at a so-called M site located 0.25 Å from the O atom on the rotational axis, and displaced toward the H atoms. In the DPP model each atom is polarizable, with Thole-type [130] damping of the charge-induced dipole and induced dipole-induced dipole interactions. Finally, there are exponential repulsive interactions between atoms of different monomers and attractive van der Waals interactions between the O atoms. In OEPM method, the model Hamiltonian (in atomic units) for an excess electron interacting with a water cluster is

$$\mathbf{H} = -\frac{1}{2}\nabla^2 - \sum_i \frac{Q_i}{r_i} f_{pc}(r_j) + \sum_j \sum_k GTF_{jk} + \sum_j \frac{\boldsymbol{\mu}_j \cdot \boldsymbol{r}_j}{r_j^3} f_{ind}(r_j) - \sum_j \frac{\alpha}{2r_j^4} f_{pol}(r_j), \quad (5.1)$$

where the first sum is over the charge sites in the DPP model, and the third term represents a short-ranged repulsive potential (V_{rep}), expanded in terms of six s GTOs on each monomer. The sums in the fourth and fifth terms which correspond respectively, to the interaction of the excess electron with the induced dipoles (from the water-water interactions)

and the induced dipoles from the electron-water interaction, are over the M sites. (Although each water molecule employs three polarizable sites for the water-water interaction, only a single polarizable site is used for the electron-water interaction. This reduces the compuational effort while having little impact of the accuracy of model.) It should be noted that for computational efficiency we have collapsed that induced dipoles on the atoms of each monomer to the associated M site. The f_{pc}, f_{ind}, and f_{pol} damping functions are represented as $f_{pc}(r_i) = 1-\exp(-b_1 r_i^2)$, $f_{ind}(r_j) = (1-\exp(-b_2 r_j^2))^2$, and $f_{pol}(r_j) = (1-\exp(-b_3 r_j^2))^2$, respectively. The f_{pc} damping term is employed in the DVR but not in the GTO version of the code.

The DVR method is well documented in the literature, [76, 77, 78, 79, 80, 81, 82, 83, 84] and only a brief summary is given here. We adopt the sine DVR approach which uses particle-in-a-box eigenfunctions as a basis. For simplicity we describe the DVR method for one dimensional case; extension to three dimensions is straightforward. The basis functions for the sine DVR method are

$$\varphi_j(x) = \begin{cases} \sqrt{\frac{2}{L}} \sin\left(\frac{j\pi(x-x_0)}{L}\right), & \text{for } x_0 \le x \le x_{n+1}, \\ 0 & \text{otherwise} \end{cases} \tag{5.2}$$

where x_0 and x_{n+1} refer to the box edges and L = x_{n+1} - x_0. The DVR kinetic energy matrix elements can be evaluated analytically:

$$\mathbf{T}_{kl}^{DVR} = -\left(\frac{\pi(n+1)}{L}\right) \begin{cases} -\frac{1}{3} + \frac{1}{6(n+1)^2} - \frac{1}{2(n+1)^2 \sin^2\left(\frac{k\pi}{n+1}\right)}, & \text{if } k = l, \\ \frac{2(-1)^{k-l}}{(n+1)^2} \frac{\sin\left(\frac{k\pi}{n+1}\right)\sin\left(\frac{l\pi}{n+1}\right)}{\left(\cos\left(\frac{k\pi}{n+1}\right) - \cos\left(\frac{l\pi}{n+1}\right)\right)^2}, & \text{if } k \ne l. \end{cases} \tag{5.3}$$

where $\mathbf{T}_{kl}^{DVR} = \langle \varphi_k^*(x) | \mathbf{T} | \varphi_l(x) \rangle$. With a δ function basis set the potential energy matrix would also be diagonal. In the finite basis sets used in actual applications, one can diagonalize the

position operator and obtaining a new set of functions that approximate delta functions. Thus, for sufficiently large DVR basis sets, to a good approximation one can treat V as diagonal. For sine DVR basis sets the diagonal elements of V are defined at the n uniformly spaced grid points $\{x_i\}$, where n is the number of sine functions in the basis set. The total Hamiltonian matrix for the 3-dimension case has the form

$$\tilde{\mathbf{H}} = \begin{pmatrix} & & & & & \\ & 3N^{4/3} & & & & \\ & \text{nonzero elements} & & & & \\ & & & & & \end{pmatrix} + \begin{pmatrix} V(q_1) & 0 & 0 & 0 & \cdots & 0 \\ 0 & V(q_2) & 0 & 0 & \cdots & 0 \\ 0 & 0 & V(q_3) & 0 & \cdots & 0 \\ 0 & 0 & 0 & V(q_4) & \cdots & 0 \\ \vdots & \vdots & \vdots & \vdots & \ddots & \vdots \\ 0 & 0 & 0 & 0 & \cdots & V(q_N) \end{pmatrix} \tag{5.4}$$

where N is the total number of DVR grid points ($N = n \times n \times n$), and q_i denotes a point on the three dimensional grid. The kinetic energy matrix has $3N^{4/3}$ nonzero elements. The resulting $N \times N$ Hamiltonian matrix is very sparse, and the eigenvalue equation, $\mathbf{H}C = \varepsilon C$, is solved using iterative Lanczos diagonalization. [131]

5.2.2 Analytical gradients in the DVR method

In the DVR approach the gradient of the energy assumes a particularly simple form since there are no Pulay terms [106, 107], and the kinetic energy terms do not contribute. The

gradient is thus given by

$$\begin{aligned}
\frac{\partial E}{\partial R} &= \begin{pmatrix} C_1 & C_2 & C_3 & \cdots & C_N \end{pmatrix} \begin{pmatrix} \frac{\partial V(q_1)}{\partial R} & 0 & 0 & \cdots & 0 \\ 0 & \frac{\partial V(q_2)}{\partial R} & 0 & \cdots & 0 \\ 0 & 0 & \frac{\partial V(q_3)}{\partial R} & \cdots & 0 \\ \vdots & \vdots & \vdots & \ddots & \vdots \\ 0 & 0 & 0 & \cdots & \frac{\partial V(q_N)}{\partial R} \end{pmatrix} \begin{pmatrix} C_1 \\ C_2 \\ C_3 \\ \vdots \\ C_N \end{pmatrix} \\
&= \sum_{i=1}^{N} \frac{\partial V(q_i)}{\partial R} C_i^2
\end{aligned} \tag{5.5}$$

where the C_i are the coefficients of the converged wavefunction.

5.2.3 Box size and grid points

In the applications of the OEPM-DVR method to $(H_2O)_n^-$ clusters, it is important to choose appropriate box sizes and grid point spacing. This can be especially challenging for excess electron system as the spatial extent of the excess electron can vary appreciable, depending on the arrangement of the water monomers. To illustrate the issues at play we consider the two $(H_2O)_6^-$ clusters and the two $(H_2O)_{45}^-$ clusters shown in Fig. 15. One $(H_2O)_6^-$ structure (A) binds the excess electron by about 0.6 eV and the other (B) binds it by only $\sim$ 0.1 eV. Both $(H_2O)_{45}^-$ structures strongly bind the excess electron, but one has it bound on the surface and the other in the interior. The geometries of the clusters were taken from Ref. 39.

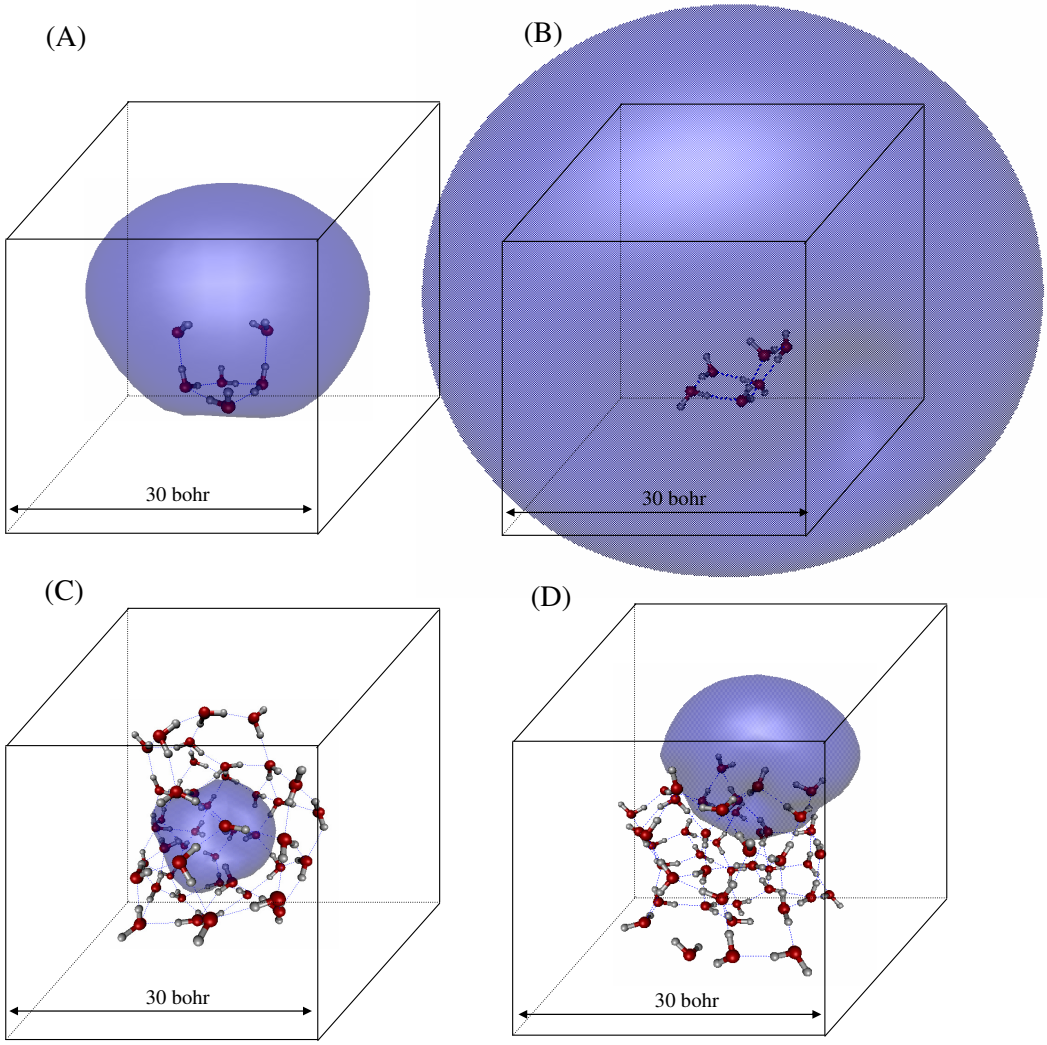

Figure 15: Isosurface containing 90% of the excess electron density calculated by the OEPM-GTO method are plotted for two $(H_2O)_6^-$ and two $(H_2O)_{45}^-$ clusters.

5.3 RESULTS

5.3.1 A convergence with box size and density of grid points

The first set of exploratory calculations employed a cubic box of 30 bohr size and 1 bohr spacing of the grid points. In these and all other calculations carried out in this study, the center of the cubic grid of DVR points was located at the center of mass of the cluster. For each of the four test systems the surface enclosing 90% of the density of the excess electron was calculated. The results are shown in Fig. 15 from which it is immediately clear that the 30 bohr box is too small for the weak electron binding $(H_2O)_6^-$ species, (B) but that it should be appropriate for the two $(H_2O)_{45}^-$ for which the excess electron is much more localized. One cannot tell from this figure alone as to whether this box size is suitable for the $(H_2O)_6^-$ (A) species.

In Fig. 16 the electron binding energies of the four test systems are plotted as a function of the number of grid point (n) along one dimension of the cubic box for box lengths of 30, 60, and 90 bohr. For the 30 bohr box the binding energies are relatively constant as n varies from 30 to 110, but for the larger boxes, the binding energies show appreciable oscillations for grids with spacings between the points greater than about 1.5 bohr. Clearly for convergence of the energies one needs to employ grids with spacings less than this. We also checked the convergence of the forces and find that in most cases, there are well converged for DVR basis sets that correspond to a grid spacings of ≤ 1 bohr.

From Fig. 16, it is also seen that the excess electron is not even bound for $(H_2O)_6^-$ (B) when the 30 bohr box is used and that the use of this small box size leads to a sizable error in the EBE of the more strongly bound $(H_2O)_6^-$ species as well. The 30 bohr box, however, is suitable for the two $(H_2O)_{45}^-$ isomers, and the 60 bohr box is suitable for obtaining well converged EBE's for all four of the test systems.

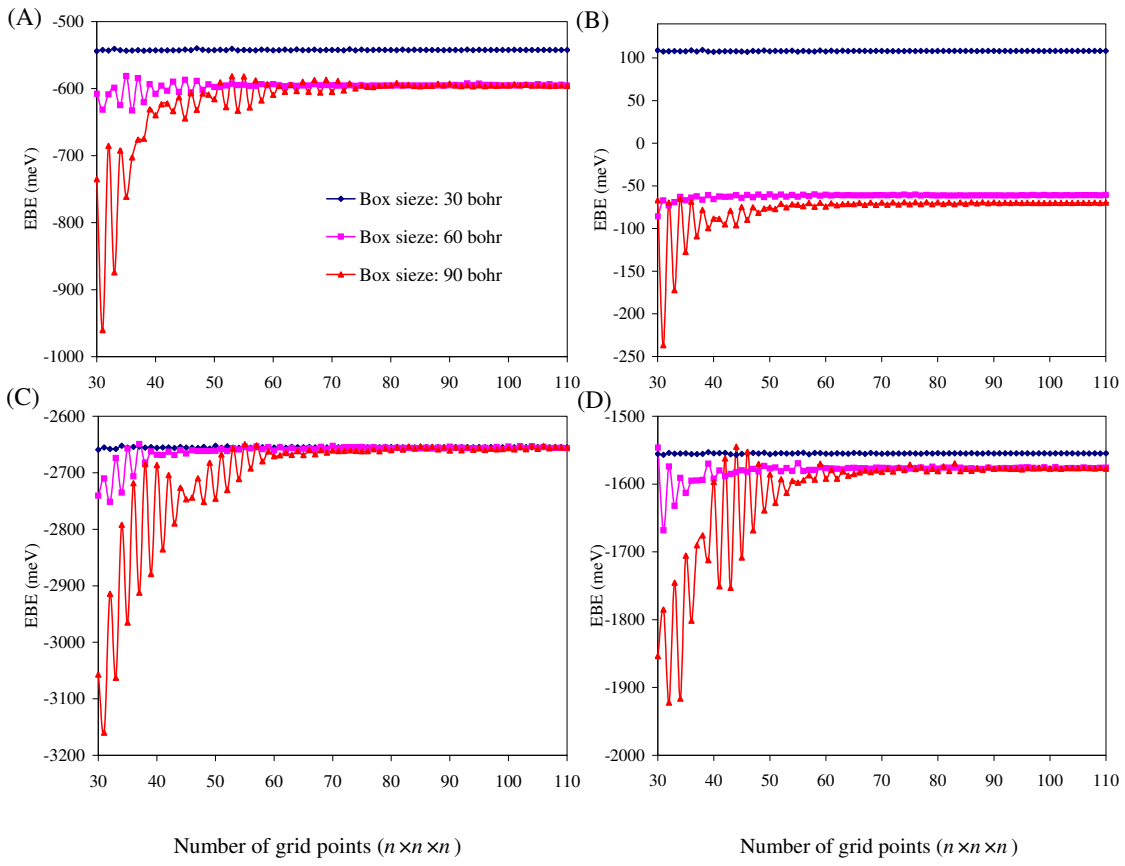

Figure 16: Electron binding energies of the four $(H_2O)_n^-$ clusters shown in Fig. 15. Results are reported for 30×30×30, 60×60×60, and 90×90×90 bohr box sizes. The number of grid points in the each direction, is varied from 30 to 110 .

5.4 PERFORMANCE OF THE DVR METHOD

In evaluating the performance of the DVR method for describing $(H_2O)_n^-$ ions, comparison is made with the timings for calculations using a Gaussian-type basis set which has been optimized for use with the OEPM method. [33] This basis set employs three s and one p function on each water monomer and a $5s4p$ set of GTOs at the center of mass of the cluster. Fig. 17 reports the CPU time for the evaluation of the energy and gradient of clusters containing two to 90 water molecules with the DVR and the GTO basis sets. DVR results are reported for 30×30×30, 60×60×60, and 90×90×90 grids. The energy and gradient evaluations with the GTO basis set both display $O(M^{2.9})$ scaling, where M is the number of monomers, whereas the corresponding DVR calculations essentially display $O(M^{1.0})$ and $O(M^{1.4})$ scaling, respectively. The weaker scaling in the DVR case is a consequence of the fact that the number of DVR grid points was not increased with increasing number of molecules. Of course for very large clusters, if one did not know in advance where the electron is localized, it would be necessary to adopt larger DVR grids. For the 60×60×60 grid, the energy plus gradient calculations with the DVR basis set are faster than calculations with the GTO basis set for $M \geq 17$.

With the DVR basis set, the most time consuming part of the energy calculation is the diagonalization of the Hamiltonian matrix. Thus, the CPU time for the energy calculation in the DVR basis set depends mainly on the number of grid points, and only weakly (linearly) on the number of water molecules (see Figs. 17 and 18). For the gradient evaluations with the DVR method, there is a slightly stronger $\sim O(M^{1.4})$ scaling with the number of monomers. Fig. 19 reports the computational time associated with the various parts of the gradient evaluation as a function of the number of water monomers. For the $n < 6$ clusters, the most time consuming part of the gradient evaluation involves the derivatives of the repulsive potential, but for larger clusters, the derivatives of the induced dipole moment

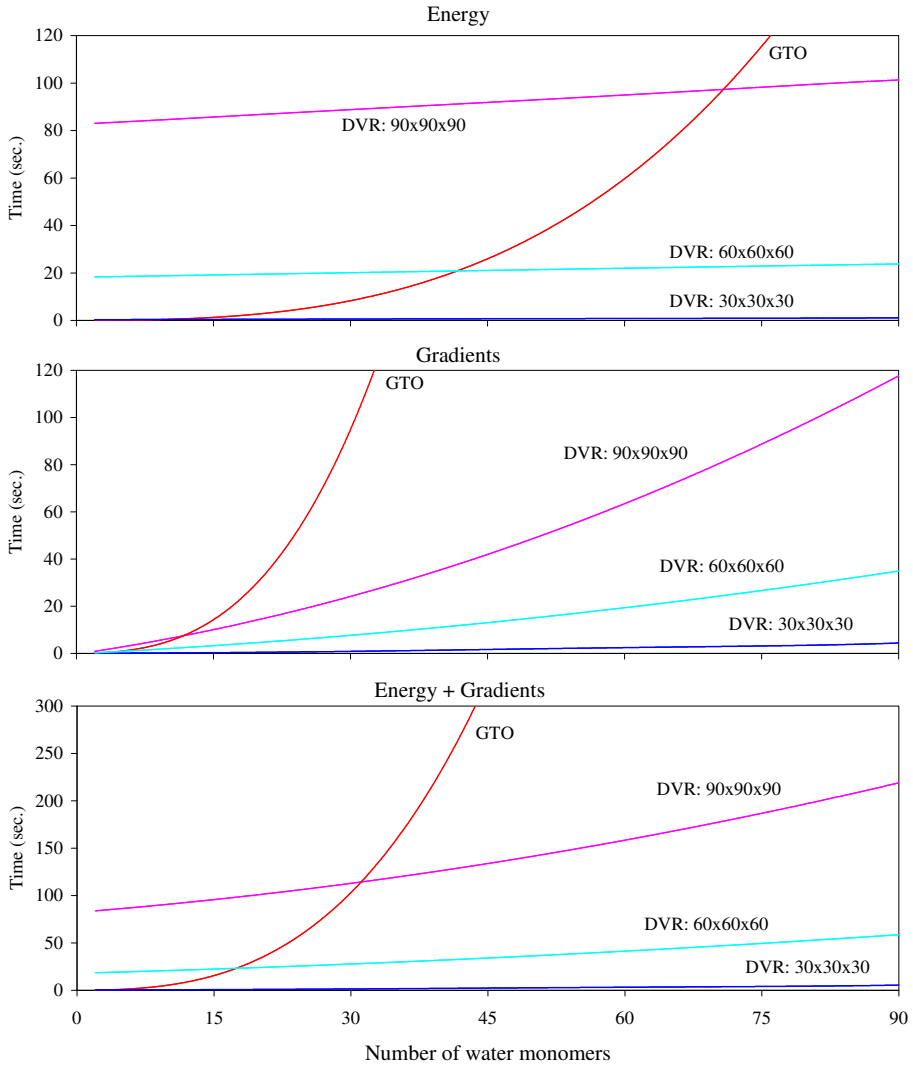

Figure 17: CPU time required to calculate the energy and gradient using GTO basis sets and three different DVR grids, 30×30×30, 60×60×60, and 90×90×90. The last graph shows the time of the energy and gradient together.

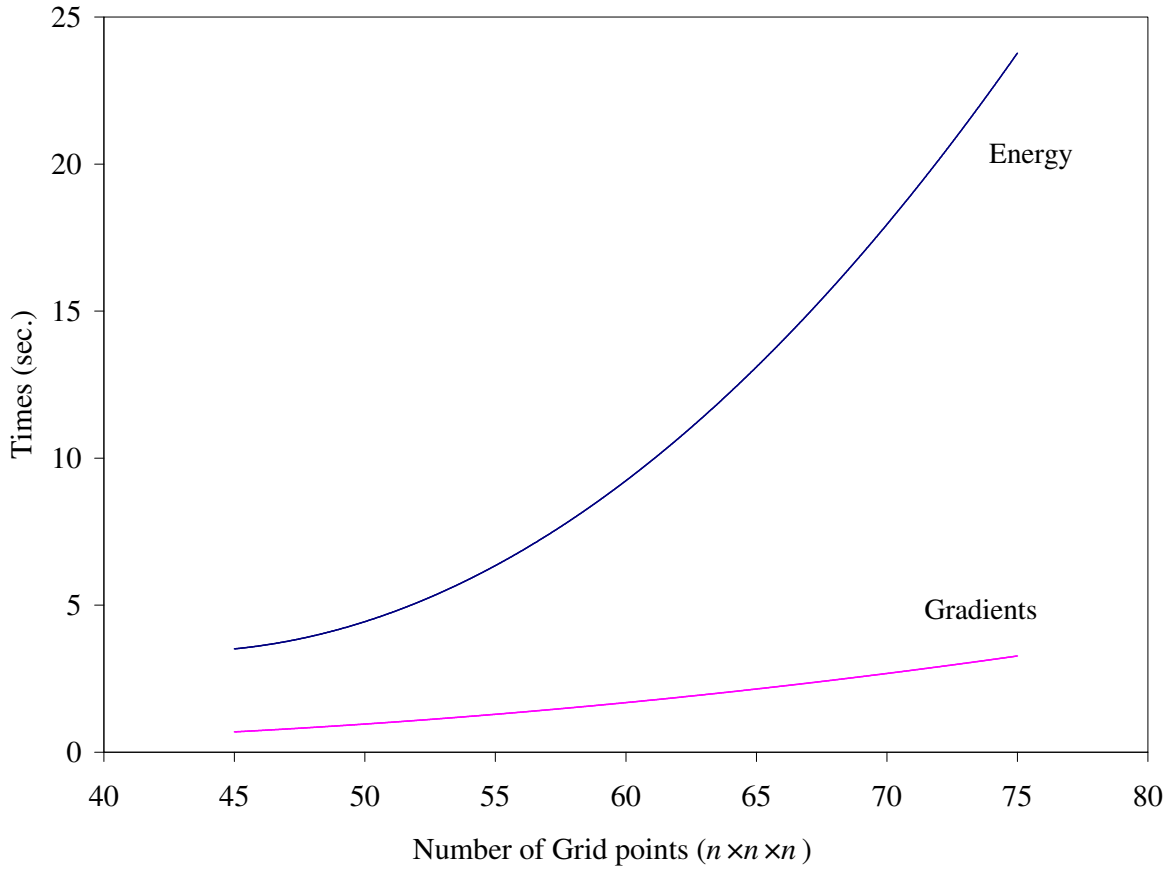

Figure 18: CPU time required to calculate the energy and gradients of a $(H_2O)_6^-$ cluster using 60×60×60 bohr box size. The number of gird points in the each direction is varied from 45 to 75.

term dominate the gradient evaluation. The latter derivatives can be expressed as

$$\frac{\partial V_{ind}}{\partial R_k} = \frac{\partial}{\partial R_k} \sum_j \frac{\boldsymbol{\mu}_j \cdot \boldsymbol{r}_j}{r_j^3} = \sum_j \boldsymbol{\mu}_j \cdot \frac{\partial}{\partial R_k} \left(\frac{\boldsymbol{r}_j}{r_j^3} \right) + \sum_j \frac{\boldsymbol{r}_j}{r_j^3} \cdot \frac{\partial \boldsymbol{\mu}_j}{\partial R_k}, \tag{5.6}$$

where the subscript k denotes the atomic coordinates and μ_j is the induced dipole moment located at the M site of the jth molecule. The first term on the right hand side of Eq. 5.6 can be expanded as

$$\begin{aligned} \sum_j \boldsymbol{\mu}_j \cdot \frac{\partial}{\partial R_k} \left(\frac{\boldsymbol{r}_j}{r_j^3} \right) &= \sum_j \mu_{xj} \frac{\partial}{\partial R_k} \left(\frac{r_{xj}}{r_j^3} \right) + \mu_{yj} \frac{\partial}{\partial R_k} \left(\frac{r_{yj}}{r_j^3} \right) + \mu_{zj} \frac{\partial}{\partial R_k} \left(\frac{r_{zj}}{r_j^3} \right) \\ &= \mu_{xk} \frac{\partial}{\partial R_k} \left(\frac{r_{xk}}{r_k^3} \right) + \mu_{yk} \frac{\partial}{\partial R_k} \left(\frac{r_{yk}}{r_k^3} \right) + \mu_{zk} \frac{\partial}{\partial R_k} \left(\frac{r_{zk}}{r_k^3} \right) \end{aligned} \tag{5.7}$$

Only the term with k=j is nonzero, making the evaluation of this contribution to the gradient computationally fast. However, the second term on the right-hand side of Eq. 5.6, which can be expanded as

$$\sum_j \frac{\boldsymbol{r}_j}{r_j^3} \cdot \frac{\partial \boldsymbol{\mu}_j}{\partial R_k} = \sum_j \left[\left(\frac{r_{xj}}{r_j^3} \right) \frac{\partial \mu_{xj}}{\partial R_k} + \left(\frac{r_{yj}}{r_j^3} \right) \frac{\partial \mu_{yj}}{\partial R_k} + \left(\frac{r_{zj}}{r_j^3} \right) \frac{\partial \mu_{zj}}{\partial R_k} \right], \tag{5.8}$$

does not undergo such a simplification. In the gradient evaluation, only the induced dipole moment term involves a sum over molecules. Of the clusters considered here the computational effort associated with the terms in Eqs. 5.7 and 5.8 are O($M^{1.0}$) and O($M^{1.8}$), respectively. Hence for sufficiently large clusters, the gradient evaluation in the DVR approach will display a computational scaling approach O($M^{1.8}$). (Again this assumes the number of grid points does not grow with system size, which in most applications can be assured by use of a prescreening step.) In general, in the absence of prescreening, the number of grid points would grow linearly water system size giving in overall scaling of O($M^{2.8}$), the same as with the GTO basis set.

The OEPM-DVR code has been parallelized using structured loop-level parallelism implemented via OpenMP. [129] The energy gradient and potential energy computations contain computationally intensive data-parallel loops, parallelization of which is straightforward.

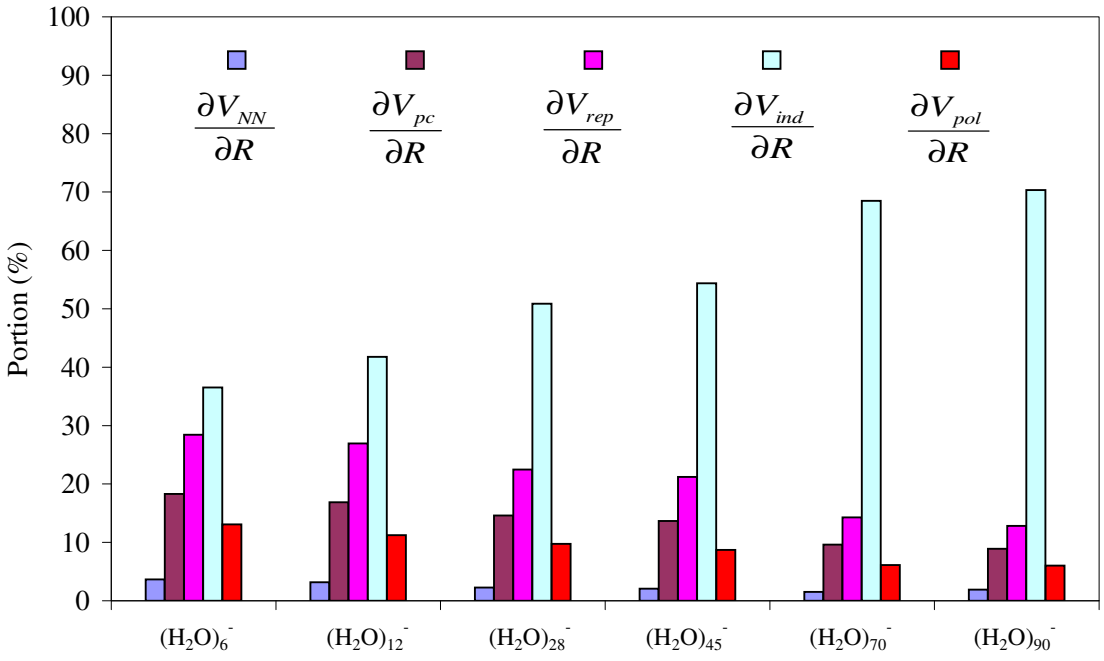

Figure 19: Relative CPU times for the various contributions to the gradient calculation.

The iterative Lanczos algorithm used to calculate the energy, on the other hand, is implemented via a sequential solver library, [132,133] and the OpenMP parallelization was limited to only the eigenvector update stages during reverse communication with the solver.

Fig. 20 reports the results of the parallel speed-up analysis. The runs are made on a SGI Altix 4700 shared-memory system. For the speedup analysis the energy and gradient for the $(H_2O)_{45}^-$ cluster are calculated using a 60×60×60 DVR grid. Fig. 20 shows the normalized wall-time for various sections of the code as well as the overall run. Near-perfect speed-up is obtained for the potential energy and the gradient computations, while the diagonalization step does not perform well beyond 12 cores. For $(H_2O)_{45}^-$, the computer time to evaluate the enery exceeds that for the gradient, causing the efficiency of the parallelization of the energy plus gradient to perform poorly on over 12 CPUs as well. However, the computational effort to evaluate the gradient grows more rapidly with increasing cluster size than the time to evaluate the energy (see Fig. 17), and for $(H_2O)_{90}^-$ the scaling of the parallelization is quite good up to about 32 cores. As a result nanosecond MD simulations are now possible on large $(H_2O)_n^-$ clusters using the OEPM approach even with the inclusions of interaction with the induced dipoles.

5.5 CONCLUSIONS

In this work a sine-type DVR basis implementation of the one-electron polarization model for $(H_2O)_n^-$ clusters developed in our group has been described. Even with a grid as large as 60×60×60 [equivalent to 216,000 sine basis functions], the gradient calculations with the DVR approach are computationally faster than those using the GTO basis sets for clusters, containing more than 12 monomers.

The sine-type particle-in-the-box basis set, generates a uniform set of grid points. Significant computational savings could be achieved by using non-uniform grids, in particular using a sparser density of points in regions of space where the electron density of relatively low.

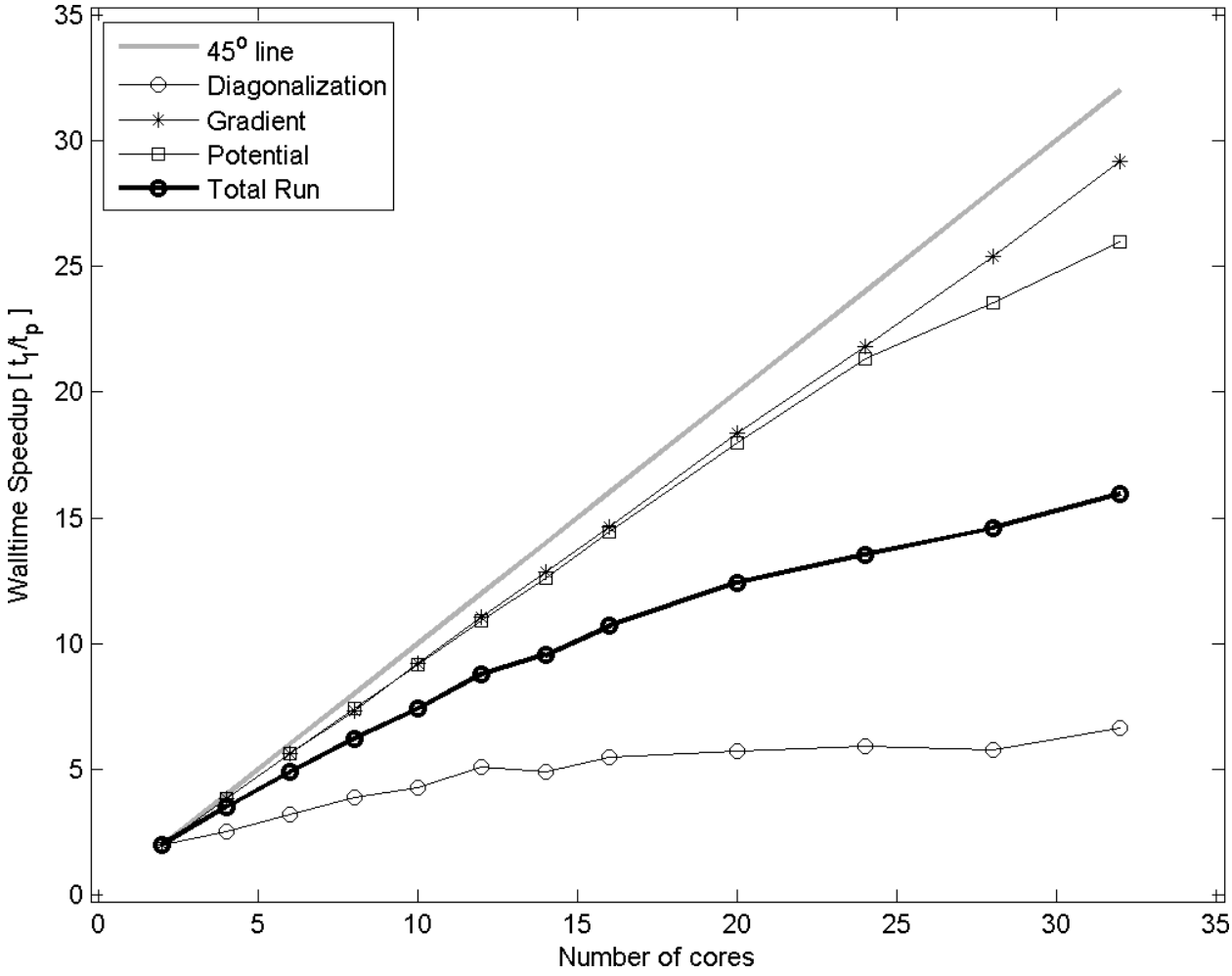

Figure 20: The parallel speed-up analysis of $(H_2O)_{45}^-$ cluster using a 60×60×60 DVR grid.

Exploratory calculations with harmonic oscillator DVR grids, in which distance between grid points grows with increasing distance from the center of the box, shows that with such grids it is possible to achieve about an order of magnitude in reduction in the CPU time required to evaluate the energy and gradients in the DVR approach with no loss of accuracy.

6.0 SIMULATION OF THE $(H_2O)_8$ CLUSTER WITH THE SCC-DFTB ELECTRONIC STRUCTURE METHOD

Manuscript in preparation, Tae Hoon Choi and Kenneth D. Jordan.

6.1 INTRODUCTION

Water clusters have been the subject of numerous theoretical studies, employing the model potentials as well as electronic structure methods. [34, 35, 36, 37, 38, 39, 40, 41, 42, 43, 44, 45, 46, 47, 48, 49] Although the MP2 and density functional methods, in particular, have proven valuable for characterizing water clusters, their computational cost precludes their use for exhaustive exploration of the potential energy surfaces or for carrying out finite temperature (or energy) simulations, for clusters containing more than eight monomers. As a result, most theoretical studies exhaustively exploring the stationary points of the potential energy surfaces or carring out Monte Carlo or molecular dynamics simulations of $(H_2O)_n$, n $\geq$ 6 clusters, have been carried out using model potentials. Over the last few years significant progress has been made in developing accurate force fields for water [35, 36, 37, 38, 39, 40]. However even the most sophisticated of these models are unable to properly describe water over the entire range of condition of interest and, in many cases, comparable quality force fields do not exist for solute-water interactions. An alternative approach would be to employ a semiempirical electronic structure method such as AM1 or PM3. However, these methods generally perform significantly poorer than force field methods for describing water clusters.

The recently introduced self-consistent-charge density-functional tight-binding (SCC-DFTB) [91,92,93,94,95,96,98,99] method is comparable in computational speed to traditional semiempirical methods, but, in general, provides a more accurate description of geometries and relative energies of chemical species. Thus, it is of considerable interest to determine whether the SCC-DFTB method is riable method for characterizing water clusters.

In this work we apply three various of the SCC-DFTB+D method to the $(H_2O)_8$ cluster in order to see how accurately these methods can catch the potential energy surfaces. $(H_2O)_8$ has been studied well by our previous works, so this study is the basic step to apply these methods to water clusters. In the present study we have carried out global optimizations using the basin hopping Monte Carlo method. [67, 34, 68, 134, 135, 136, 114, 137, 138, 139, 140] and have also used PTMC (Parallel Tempering Monte Carlo) simulations [47, 48, 49, 141, 142, 143] for calculating the thermodynamic properties of the clusters in conjunction with the SCC-DFTB method.

6.2 THEORETICAL METHOD

6.2.1 Electronic structure method

The SCC-DFTB method is derived from density functional theory (DFT), by making use of second-order expansion of the Kohn Sham total energy with respect to the charge density fluctuations, and evaluating the Hamiltonian matrix elements in a minimal basis of pseudoatomic orbitals and a two-center approximation [91, 92, 93, 94, 95, 96, 98, 99]. The total energy including a correction term to account [92] for dispersion is given by Equation (7.1).

$$E_{tot} = \sum_{i\mu v} c_\mu^i c_v^i H_{\mu v}^0 + \frac{1}{2}\sum_{\alpha\beta}\gamma_{\alpha\beta}\Delta q_\alpha \Delta q_\beta + E_{rep} + E_{dis} \tag{6.1}$$

where the $H_{\mu v}^0$ are the Hamiltonian matrix elements, Δq_α and Δq_β are charge fluctuation

term on atoms α and β, respectively, and E_{rep} accounts for short-range repulsion.

In order to more correctly describe hydrogen-bonding interactions, Elstner [99] has introduced a damping factor into the $\gamma_{\alpha\beta}$ function for atomic pairs involving hydrogen

$$\gamma_{\alpha H} = \frac{1}{R_{\alpha H}} - S_{\alpha H} * f(R_{\alpha H}) = S_{\alpha H} * \exp\left[-\left(\frac{U_\alpha + U_H}{2}\right)^\zeta R_{\alpha H}^2\right], \tag{6.2}$$

where $S_{\alpha H}$ is an exponentially decaying short-range function and U_α is the atomic Hubbard parameter that is related to the chemical hardness. [144] The parameter, ζ, in the damping function was adjusted based on high-level *ab initio* results for hydrogen-bonded clusters. In this work we refer to this method as SCC-DFTB+D(HB).

In another recent modification of the SCC-DFTB method third order correction terms have been incorporated to give the expression. [98, 99]

$$E_{tot} = \sum_{i\mu v} c_\mu^i c_v^i H_{\mu v}^0 + \frac{1}{2}\sum_{\alpha\beta} \gamma_{\alpha\beta}\Delta q_\alpha \Delta q_\beta + E_{rep} + E_{dis} + \frac{1}{6}\sum_\alpha \eta_{\alpha\alpha\alpha}(\Delta q_\alpha)^3, \tag{6.3}$$

where $\eta_{\alpha\alpha\alpha}$ is related to the charge derivative of the atomic Hubbard parameter, U_α. A more detail description of both modifications can be found in Ref. 23. In this work the SCC-DFTB method with both H-bond and Third-order corrections is refered to as SCC-DFTB+D(HB+3rd).

Before presenting the results for the octamer, it is instructive to apply the various SCC-DFTB models to the water dimer. Figure 21 reports the energy of the water dimer as a function of the OO distance calculated with each of the three SCC-DFTB methods as well as with the MP2/aug-cc-pV5Z methods. In generating the potential curves, the geometry of the monomer was first optimized using the MP2/aug-cc-pVTZ method. The resulting bond lengths and angles were then employed in the dimer calculations. The equilibrium geometry of the dimer was then optimized using the MP2/aug-cc-pVTZ method, assuming rigid monomers. The resulting flap angles giving the relative orientation of the two monomers

were then fixed in mapping out the potential energy curves of the dimer. In the original SCC-DFTB+D method, the binding energy of the dimer is only about half as large in magnitude as that obtained with the MP2/aug-cc-pV5Z method.

The H-bonding correction of Ref. 23 increase the binding energy of the dimer by about 1.3 kcal/mol while the 3rd-order correction proves to be relatively unimportant, increasing the binding energy by only 0.14 kcal/mol. The SCC-DFTB+D (HB+3rd) method underbinds the dimer by about 0.35 kcal/mol and gives minimum at too short an OO seperation. In addition the SCC-DFTB+D methods all have the wrong shape to the potential for R between about 3 and 5 Å. The too short an OO seperation for the potential energy minima, reflect an inadequacy in the E_{rep} term in the SCC-DFTB method, whereas the attractive portion of the potential is a consequence of the underestimation of induction and despersion. Although the H-bond correction can ,in part, compensate for the underestimation of polarization in the SCC-DFTB method, it does not "build in" the correct R dependence. We note also that the dispersion correction in the SCC-DFTB+D method damps out the dispersion so strongly that the dispersion contribution near $R_{oo} = 2.9$ Åis only 0.05 kcal/mol as compared with the value of 1.3 kcal/mol found in SAPT calculation.

6.2.2 Basin hopping Monte Carlo method

The basin hopping Monte Carlo method uses Monte Carlo walks combined with gradient-based local optimization to locate local minima of the potential energy surface. [67,34,68,134, 135,136,114,137,138,139,140] Sampling in the Monte Carlo walks is based on the energies of the minima and, as a result, barriers are effectively removed making this an efficient approach for searching for low-energy minima. In this work a modified version of the limited-memory quasi-Newton routine(LBFGS) by Nocedal has been employed for the minimization. [116]

In the basin hopping optimizations, the Monte Carlo moves consisted of rigid-body translations and rotations of the H_2O species. Monte Carlo moves that generated OO distance less than 3 Bohr were rejected, and step sizes were adjusted so that the acceptance ratio was

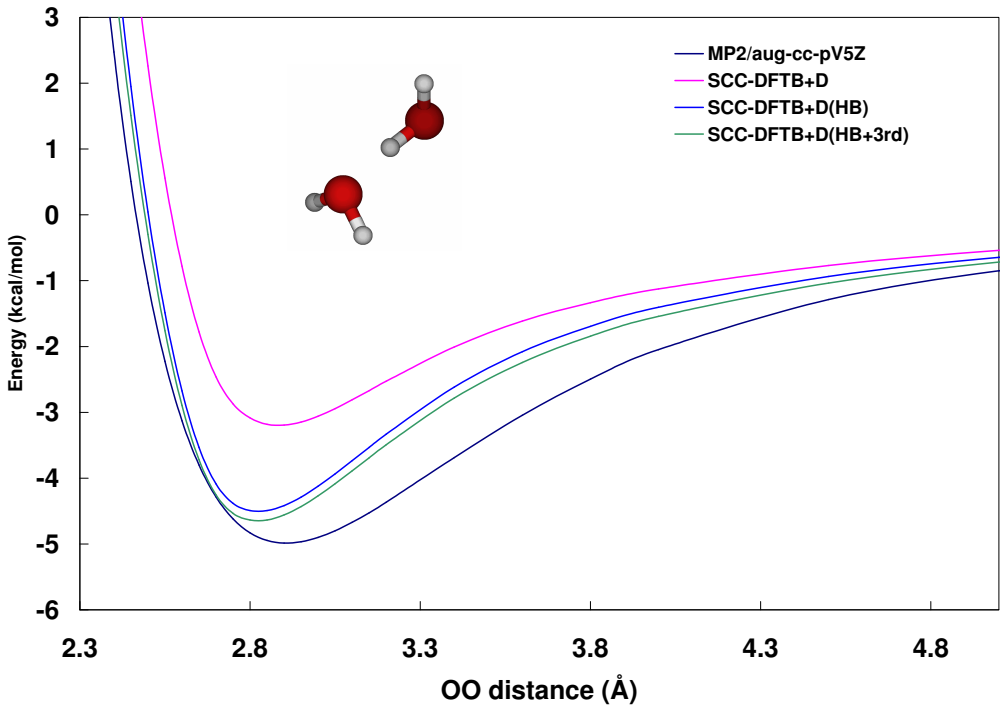

Figure 21: Interaction energy of the water dimer as a function of the OO separation with the flap angles fixed at the values for the MP2/aug-cc-pVTZ optimized minimum energy structure. Results are reported for the SCC-DFTB+D, SCC-DFTB+D(HB), SCC-DFTB+D(HB+3rd) and MP2/aug-cc-pV5Z methods.

adout 0.4. In each MC step, the number of molecules and which molecules to move were chosen at random. With this setup, we carried out basin hopping runs for 10000 steps at a reduced temperature of 2.0 kJ/mol.

6.2.3 PTMC(Parallel-Tempering Monte Carlo) simulations

PTMC simulations were carried out for $(H_2O)_8$ with 20 temperatures for the original SCC-DFTB and 24 temperatures for modified SCC-DFTB methods. Every 800^{th} move an exchange of configurations from replicas at adjacent temperatures(T_i and T_{i+1}) was attempted. A constraining sphere of 4.25 $\mathring{A}$ was used to suppress evaporation. Based on a series of trial runs, the simulation temperature range for SCC-DFTB potential was chosen to be 50 to 190 K, with 10K temperature intervals for T $\leq$ 100, 5K intervals for T=100 - 160K and 10K intervals for T=160K - 190K. For the modified SCC-DFTB potentials, a temperature range, from 110 to 290K, was chosen, with 10K temperature intervals for T=110 - 190K, 5K intervals for T=190 - 240K, and 10K intervals for T=240 - 290K.

Each Monte Carlo cycle consisted of an attempted rotation and translation of each H_2O as the rigid molecule moves. The step sizes were adjusted to give acceptance ratios of 50%. The simulations of $(H_2O)_8$ for all of SCC-DFTB methods employed 10^6 cycles for equilibration, followed by 10^7 production cycles for averaging. The dimensionless configurational constant volume heat capacity curves were calculated from the potential energy fluctuations using

$$\frac{C_v}{K_B} = \frac{1}{(K_B T)^2}(\langle E^2 \rangle - \langle E \rangle^2) \tag{6.4}$$

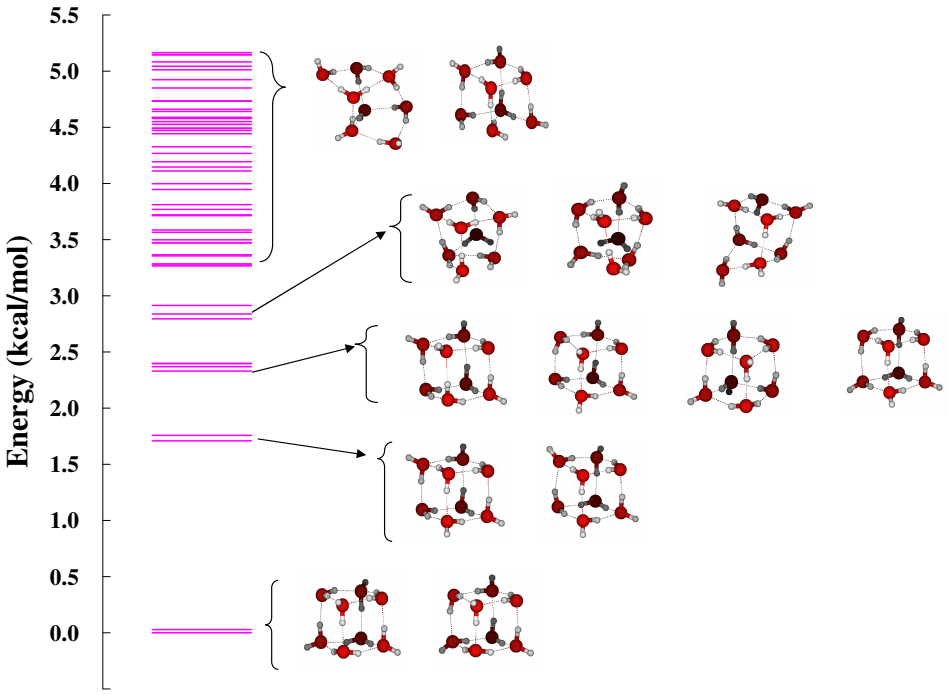

Figure 22: Relative energies of low-lying minima of $(H_2O)_8$ determined using the basin hopping Monte Carlo optimizations with the SCC-DFTB method

6.3 RESULTS

6.3.1 Energy diagram of $(H_2O)_8$

Figure 22 reports the structures and relative energies of the low lying potential energy minima of $(H_2O)_8$ as described using the SCC-DFTB+D method together with the basin hopping Monte Carlo procedure. As found previously using model potentials and the MP2 electronic structure methods, $(H_2O)_8$ has two low-energy cubic structures (of S_4 and D_{2d} symmetry) followed by a sizable ($\sim$ 1.7 kcal/mol) energy gap, then six more cubic like structures, followed by a large number of non-cubic structures at still higher energy. Several of the low-lying non-cubic structures are found to be 1-2 kcal/mol lower in energy with the SCC-DFTB+D procedure than with MP2 calculations. [41]

Figure 23 depicts the relative energies of the low-lying local minima of $(H_2O)_8$ obtained using the three SCC-DFTB methods. The inclusion of the H-bonding corrections tend to destabilize both the higher lying cubic structure and the non-cubic structures relative to the S_4 and D_{2d} cubic isomers.

6.3.2 Thermodynamic properties of $(H_2O)_8$

Heat capacity curves for $(H_2O)_8$ calculated using parallel-tempering Monte Carlo simulations with the three SCC-DFTB+D approaches are shown in Figure 24. The heat capacity curve of the SCC-DFTB+D method has a pronounced peak near T=134K indicative of melting of the clusters. This peak moves up to about 200K in the simulations using the modified SCC-DFTB+D methods. Figure 25 reports histograms of the potential energies for themperatures near the maxima of the various heat capacity curves. For example, with the TIP4P water model, the peak in the heat capacity curve occurs near T=212K. The different melting temperatures for the original SCC-DFTB and modified methods can be understood in term of qualitative differences in the distribution of local minima (Fig. 23).

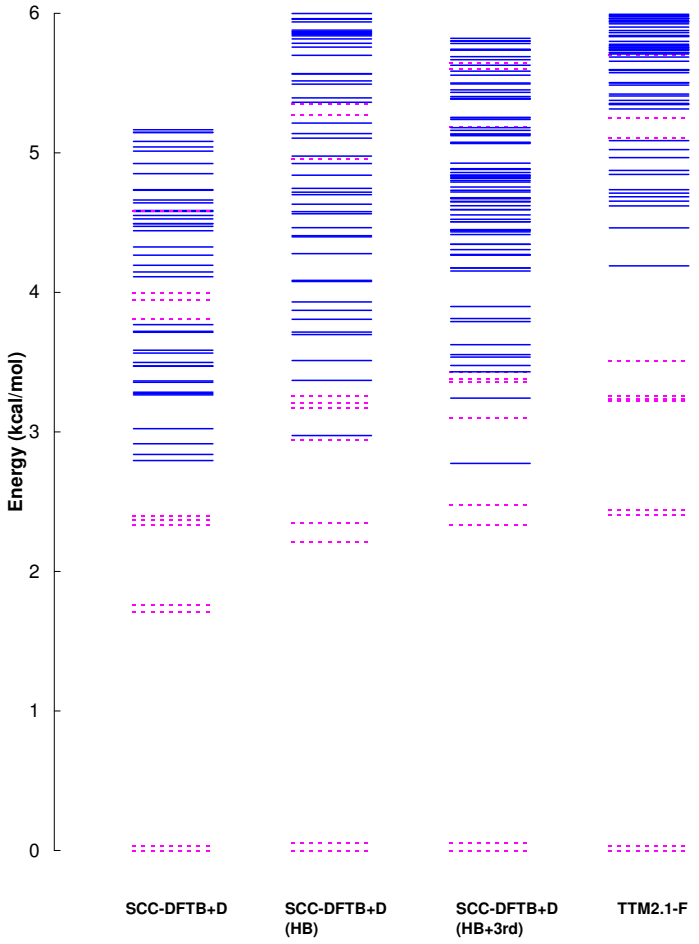

Figure 23: Energy level diagram of $(H_2O)_8$ determined using the basin hopping Monte Carlo optimization with the original and modified SCC-DFTB methods, and TTM2.1-F results from Ref. [40]. The energies of cubic and non-cubic structures are designated as dashed lines and solid lines, respectively.

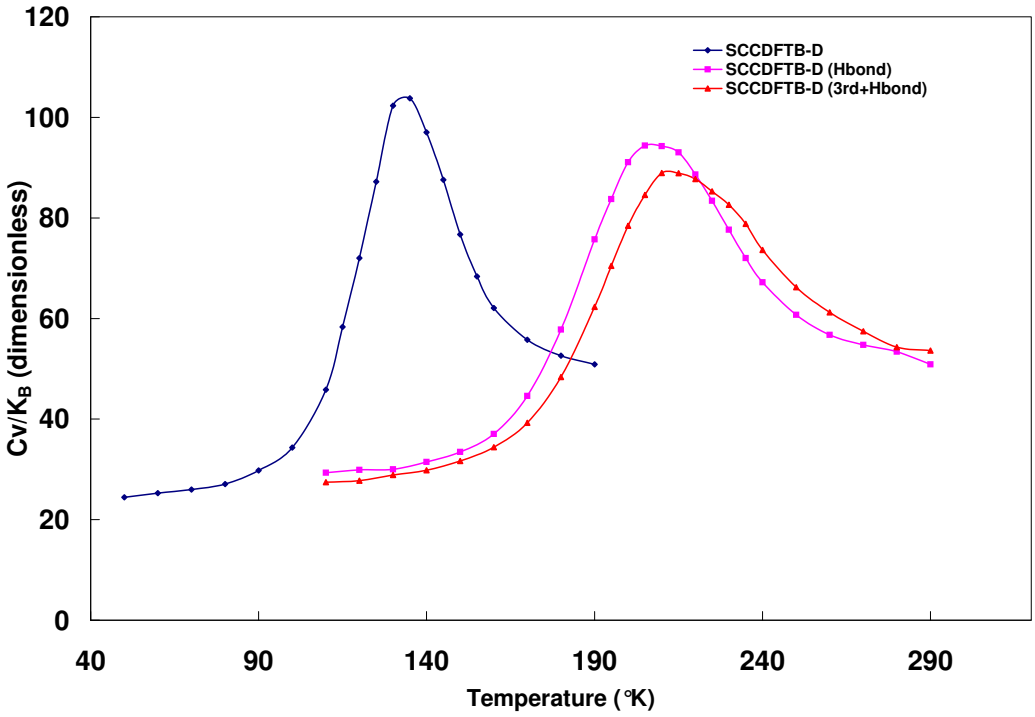

Figure 24: Heat capacity curve of $(H_2O)_8$ calculated using the parallel tempering Monte Carlo method together with three variants of the SCC-DFTB

It is known from previous studies that the pronounced peak in the heat capacity curve of $(H_2O)_8$ is due to a transition from the two low-energy cubic structures to the higher-energy non-cubic structuresa [47, 48].

6.4 CONCLUSIONS

We have applied the SCC-DFTB+D electronic structure method to the $(H_2O)_8$ cluster together with the basin hopping Monte Carlo method and PTMC simulation. PTMC simulatiions with the SCC-DFTB+D method give a melting transition of 135K, appreciably below that reported previously in simulations using the TIP4P, NCC, and DC water models. [47,48] The PTMC simulations with the SCC-DFTB+D method with H-bonding correction places the melting transition near 195 K, close to that found with the above-mentioned model potentials. The basin hopping Monte Carlo simulations reveals that in the absence of the H-bonding correction, the SCC-DFTB+D method places many more non-cubic structures below 4kcal/mol than found in the calculations with the H-bonding correction. This is responsible for the lower melting transition in the SCC-DFTB+D method. Comparison of the relative energies of selected isomers calculated with the three SCC-DFTB methods with those from MP2 calculations, shows that the overall, the inclusion of the H-bond corrections improves the agreement with the MP2 results, but that even with the H-bonding and 3rd-order correction, the relative energies from the SCC-DFTB calculations differ by up to 2 kcal/mol from the MP2 predictions.

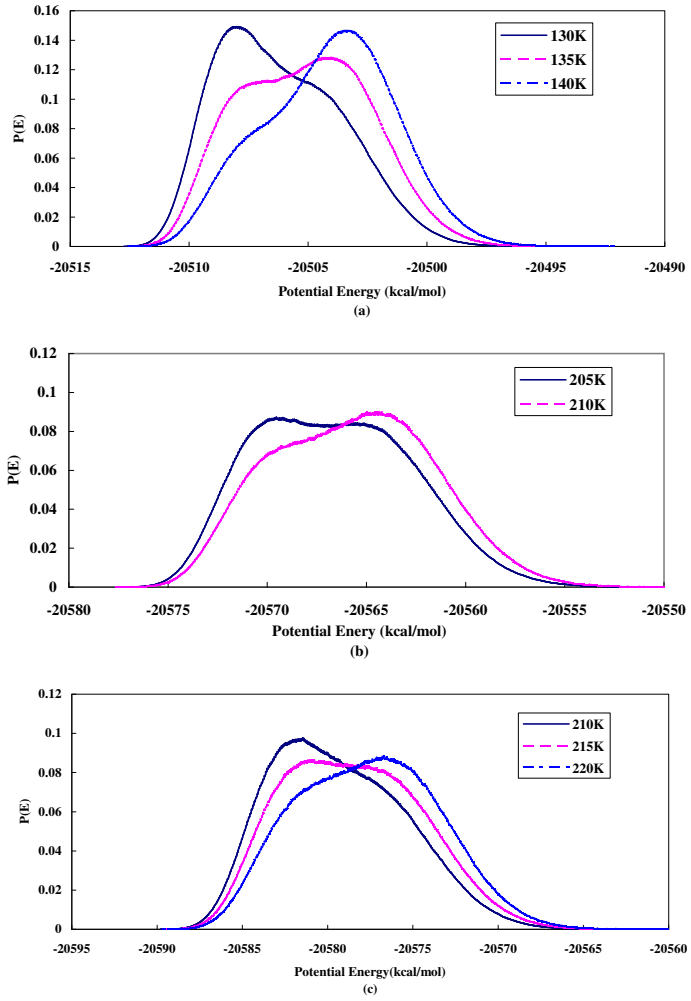

Figure 25: Histograms of potential energies of $(H_2O)_8$ from PTMC simulations at T=130,135, and 140K in the original SCC-DFTB method (a), at T=205 and 210K in the H-bonding correction (b) , and at T=210,215, and 220K in the H-bonding and 3rd-order corrections.

7.0 APPLICATION OF THE SCC-DFTB METHOD TO $H^+(H_2O)_{21}$ AND $H^+(H_2O)_{22}$

This work has been submitted for publication to the Jouranl of Physical Chemistry.

7.1 INTRODUCTION

Excess protons in water play an important role in many chemical and biological processes. [50,51,52,53,54,55,56,57,58,59,60,61,62,63,64] Yet the nature of excess protons in liquid water has been hard to pin down experimentally. Computer simulations [50,51,52] reveal that there is a rapid interconversion between Eigen [$H_9O_4^+$] [145,146] and Zundel [$H_5O_2{}^+$] type species. [147,148] Recent experimental work on protonated water clusters has allowed one to isolate the Zundel and Eigen species and to obtain their vibrational signatures. [54] The $H^+(H_2O)_{21}$ magic number cluster, in particular, has been the subject of numerious experimental and theoretical studies. [52,53,54,55,56,57] Theoretical studies on protonated water clusters of this size are challenging due to the large number of local minima on their potential energy surfaces. [149,150,151,152,153,154,155,156,157,158,159,160,161,162] Although *ab initio* MP2 calculations do accurately describe protonated water clusters, they are too computationally demanding to use in exhaustive searches of the stationary points on the potential energy surfaces or for performing Monte Carlo or molecular dynamics simulations for clusters the size of $H^+(H_2O)_{21}$. Traditional density functional methods are computationally faster, but are known to incorrectly order the isomers of water clusters. [163,164,165] Model

potentials [154,155,156,157] and effective valence bond (EVB) methods [158,159,160,161,162] have been developed to describe excess protons in water. The effective valence bond methods in particular, hold considerable promise, but they are not yet at the point that they accurately reproduce the relative energies of isomers obtained from MP2 calculations.

This leads naturally to interest in whether alternative approaches such as the self-consistent-charge density-functional tight-binding (SCC-DFTB) method [91, 92, 93, 94, 95, 96, 97, 98, 99] can provide a semiquantitatively accurate description of the potential energy landscapes of protonated water clusters. In the present study, two versions of the SCC-DFTB method are applied to the $H^+(H_2O)_{21}$ and $H^+(H_2O)_{22}$ clusters, in conjunction with the basin-hopping Monte Carlo method [67,34,68,134,135,136,114,137,138,139,140,161] to locate the local minima. The results are compared with those of density functional Becke3LYP [100] calculations. (Although DFT methods without corrections for long-range dispersion interactions can display a bias toward open rather than more compact clusters, they are adequate for addressing issues such as the relative stability of Eigen and Zundel structures.)

7.2 METHODOLOGY

7.2.1 Electronic structure calculations

The SCC-DFTB method is based on a second-order expansion of the Kohn-Sham total energy in terms of the charge density fluctuations, with the Hamiltonian matrix elements being evaulated using a minimal basis set of pseudoatomic orbitals, along with a two-center approximation. [91,92,93,94,95,96,97,98,99] In addition in the SCC-DFTB+D approaches considered here, the total energy also includes damped atom-atom C_6/R^6 terms to account for dispersion interactions. [92] The energy is expressed as

$$E^{SCC-DFTB+D} = \sum_{i\mu v} c_\mu^i c_v^i H_{\mu v}^0 + \frac{1}{2}\sum_{\alpha\beta}\gamma_{\alpha\beta}\Delta q_\alpha \Delta q_\beta + E_{rep} + E_{dis}, \tag{7.1}$$

where the $H^0_{\mu v}$ are a Hamiltonian matrix elements evaluated in terms of atom-centered basis functions ϕ_μ, and the coefficients c^i_μ give the atomic contributions of the i^{th} Kohn-Sham orbital. Δq_α and Δq_β are charge fluctuations associated with atoms α and β, respectively, and E_{rep} accounts for short-range repulsion. In the original versions of SCC-DFTB theory the $\gamma_{\alpha\beta}$ function was approximated as

$$\gamma_{\alpha\beta} = \frac{1}{R_{\alpha\beta}} - S_{\alpha\beta}, \tag{7.2}$$

where $S_{\alpha\beta}$ is an exponentially decaying short-range function. In order to more correctly describe hydrogen-bonding interactions, Elstner [99] added a damping factor to the $S_{\alpha\beta}$ term in the $\gamma_{\alpha\beta}$ function for atomic pairs involving hydrogen atoms

$$\gamma_{\alpha H} = \frac{1}{R_{\alpha H}} - S_{\alpha H} \times \exp\left[-\left(\frac{U_\alpha + U_H}{2}\right)^\zeta R^2_{\alpha H}\right], \tag{7.3}$$

where U_α is the atomic Hubbard parameter that is related to the chemical hardness of atom α. [144] The parameter, ζ, in the damping function was adjusted by fitting G3B3 [166] energies for small hydrogen-bonded clusters and MP2/G3large [167] energies for large complexes. The SCC-DFTB+D[HB+3rd] method includes this hydrogen bonding modification as well as third-order corrections of the form

$$E^{3rd} = \frac{1}{6}\sum_\alpha \eta_{\alpha\alpha\alpha}(\Delta q_\alpha)^3, \tag{7.4}$$

where $\eta_{\alpha\alpha\alpha}$ is related to the charge derivative of the atomic Hubbard parameter, U_α. A more detailed description can be found in Refs. 37 and 44.

Whether a protonated water cluster is Zundel-like or Eigen-like depends on the solvation environment of the excess proton in the cluster. [50, 51] Thus it is instructive to evaluate the performance of the SCC-DFTB methods at describing the potential energy of an excess proton located between two water monomers. To accomplish this, the geometry of $H_5O_2^+$ was first optimized at the MP2/aug-cc-pVDZ level, [168] giving an OO distance of 2.432 Å. The OO distance was then fixed at this value and the shared proton was displaced along the line joining the two O atoms, keeping all other degrees of freedom fixed. At each geometry

the energy was calculated using both SCC-DFTB+D methods as well as at the MP2 level of theory. Analogous potentials were calculated for OO distances of 2.54 and 2.60 Å. The resulting potential energy curves are depicted in 26, from which it is seen that both SCC-DFTB+D approaches are biased toward Zundel structures especially for short OO distances, with the bias being less for the SCC-DFTB+D[HB+3rd] procedure.

7.2.2 Basin hopping Monte Carlo calculations

The basin hopping Monte Carlo method uses Monte Carlo walks combined with gradient-based optimizations to locate local potential energy minima. [67, 34, 68, 134, 135, 136, 114, 137, 138, 139, 140, 161] At each move, the structure is optimized to the local minimum in its "basin", and acceptance of moves is based on the energies of the minima. As a result, barriers are effectively removed, making this an efficient approach for searching for low-energy minima. In the present study a modified version of the limited-memory quasi-Newton routine (LBFGS) [116] by Nocedal is employed for the minimizations, and the Monte Carlo moves involve both translations and rotations of the H_2O and H_3O^+ species. It was found that alternating blocks of 100 pure translational and 500 pure rotational moves at a reduced temperature of 2.0 kJ/mol, with a target acceptance ratio of 0.4, worked reasonably well. A similar strategy was employed by James and Wales in their applications of the basin hopping algorithm. [161] At each Monte Carlo step, the number of molecules to be moved was chosen at random. Monte Carlo moves that generated OO distances less than 3 bohr (1.59 Å) were rejected, and moves involving Zundel-like species [$H_5O_2^+$] were not attempted. For the $H^+(H_2O)_{21}$ and $H^+(H_2O)_{22}$ clusters, ten basin hopping Monte Carlo runs of 15000 steps each were carried out. For the $H^+(H_2O)_{21}$ cluster, one run used as the initial geometry the lowest energy structure reported in Ref. 3, and the other nine runs were started from randomly generated structures. For $H^+(H_2O)_{22}$, the initial structures for all ten runs were chosen at random.

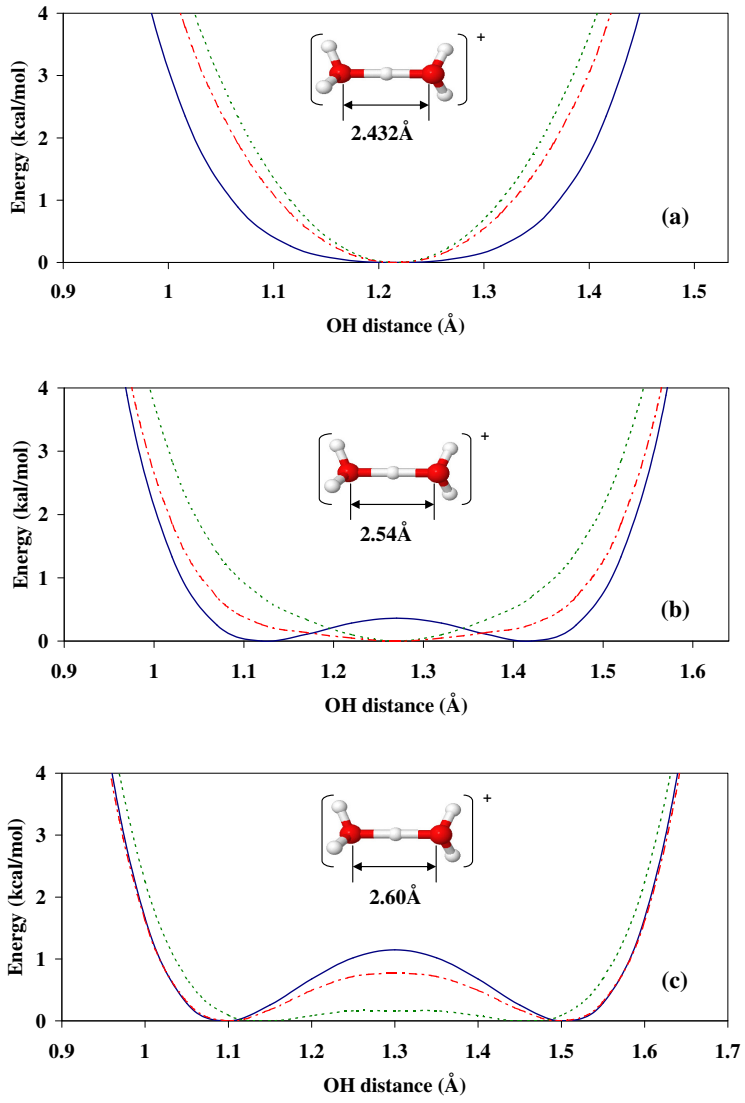

Figure 26: Interaction energies of the protonated water dimer as a function of the shared proton OH distance for fixed OO distances of (a) 2.432, (b) 2.540, and (c) 2.600 Å. Results obtained with the SCC-DFTB+D, SCC-DFTB+D[HB+3rd], and MP2/aug-cc-pVDZ methods are indicated by green dotted, red dash-dotted, and blue solid lines, respectively.

7.3 RESULTS

7.3.1 Low energy minima of $H^+(H_2O)_{21}$

27 reports the relative energies of the low-lying local minima of $H^+(H_2O)_{21}$ found using basin hopping Monte Carlo calculations with the SCC-DFTB+D method starting from the lowest energy structure reported in Ref. 3 as well as from a randomly generated structure. The differences in the distributions of local minima obtained using the two initial structures reflects the need to run longer basin-hopping simulations when dealing with such a complex potential energy surface. However, since the goal of this paper is to assess the performance of SCC-DFTB methods for describing such clusters, rather than to locate most of the low energy minima, these calculations will suffice for present purposes. 28 presents a blow up of the energy level diagram up to 0.7 kcal/mol (here we have merged the results from the ten simulations). The nine lowest energy local minima are Eigen-like with all rings on the surface being five-membered and with nine free OH (AAD) groups (A indicates acceptor and D, donor). This is the type of structure identified as the global minimum isomer in *ab initio* and DFT calculations. [52, 53, 54, 55, 56]

Starting at about 0.36 kcal/mol above the global minimum, there is high density of Zundel-like structures, some of which are derived from the water dodecahedron, with all rings on the surface being five-membered, and the others having one four-membered, one six-membered ring, and ten five-membered rings on the surface (see 28). A subset of structures optimized with SCC-DFTB+D method were reoptimized at the Becke3LYP/6-31+G(d) level [100] and found to collapse back to Eigen-like structures, consistent with the SCC-DFTB+D method having a bias toward Zundel-like species.

Additional insight into the occurrence of Zundel and Eigen structures in the SCC-DFTB+D calculations is provided by examination of 29, which reports the OO distances of the 1714 potential energy minima of $H^+(H_2O)_{21}$ located in the basin hopping Monte Carlo optimizations. 1657 of these minima have OO distances of 2.40 - 2.45 Å, which we characterize as Zundel-like, and 53 minima have OO distances ranging from 2.50 to about 2.58 Å,

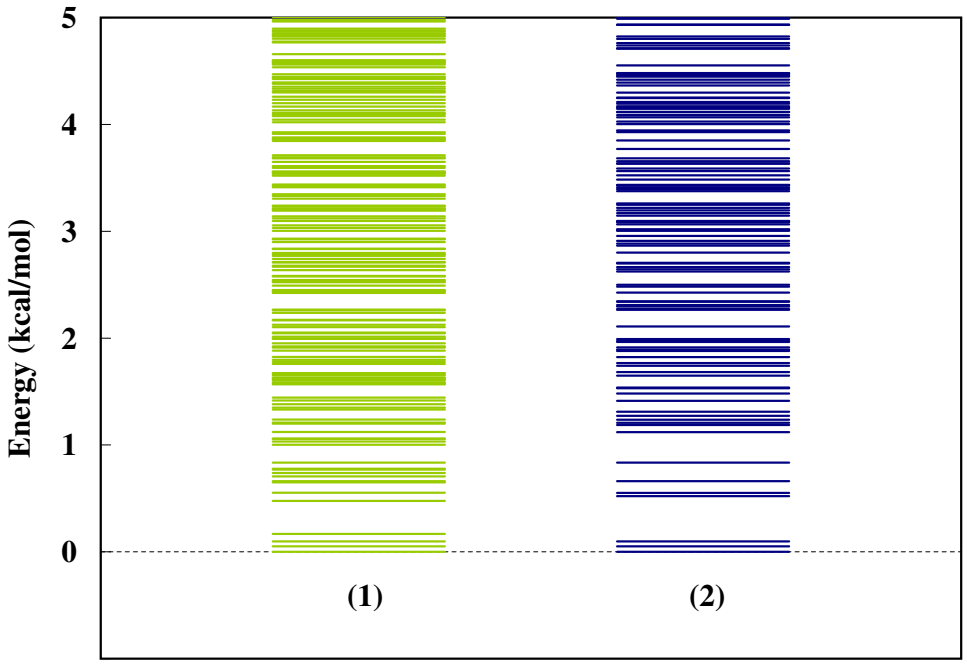

Figure 27: Distribution of potential energy minima of $H^+(H_2O)_{21}$ found using the basin hopping Monte Carlo procedure with the SCC-DFTB+D method starting from (1) the global minimum and (2) a randomly generated structure.

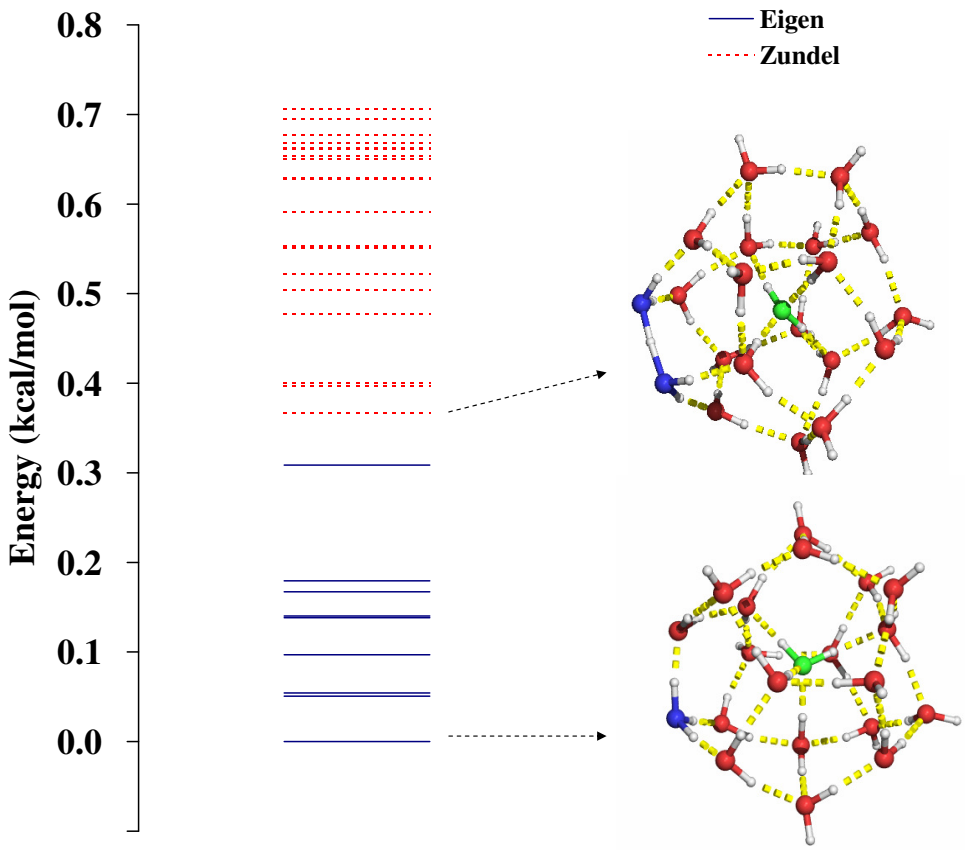

Figure 28: Low-lying potential energy minima of $H^+(H_2O)_{21}$ determined using basin hopping Monte Carlo optimization with the SCC-DFTB+D method.

which we attribute to Eigen-like structures. The four remaining minima have OO distances between 2.45 and 2.48 Å and can be viewed as intermediate between Zundel and Eigen.

The bias toward Zundel structures is even more pronounced in the SCC-DFTB+D [HB+3rd] approach as can be seen from 30, which reports the energies and structures of the low lying minima obtained with the original and modified SCC-DFTB+D methods. With the SCC-DFTB+D[HB+3rd] method, all low-lying local minima of $H^+(H_2O)_{21}$ are Zundel-like. Moreover, the low energy minima obtained with this method have structures very different from those found with SCC-DFTB+D[HB] or DFT optimizations.

7.3.2 Low energy minima of $H^+(H_2O)_{22}$

31 reports the energies of the low-lying potential energy minima of $H^+(H_2O)_{22}$ located with the basin hopping Monte Carlo optimizations using the SCC-DFTB+D energies. All low-energy structures are Zundel-like and can be separated into three classes. One class, which includes the lowest-energy structure, has ten dangling OH groups, nine of which are associated with AAD monomers and one of which is associated with a AD monomer (highlighted in green in 31). The second class of isomers, has nine free OH groups all of which are AAD. The third, higher energy, class of isomers all have a dangling acceptor H_2O molecule bound by a single H-bond to the remainder of the cluster. The four lowest energy structures have two six-membered rings and ten five-membered rings on the surface. When re-optimized using the Becke3LYP method, these four species convert to Eigen-like structures.

7.4 CONCLUSIONS

In this work we applied two versions of the SCC-DFTB+D method to investigate the $H^+(H_2O)_{21}$ and $H^+(H_2O)_{22}$ clusters. Both SCC-DFTB+D implementations show a bias toward Zundel structures. For $H_5O_2^+$ the bias is more severe for the original SCC-DFTB+D

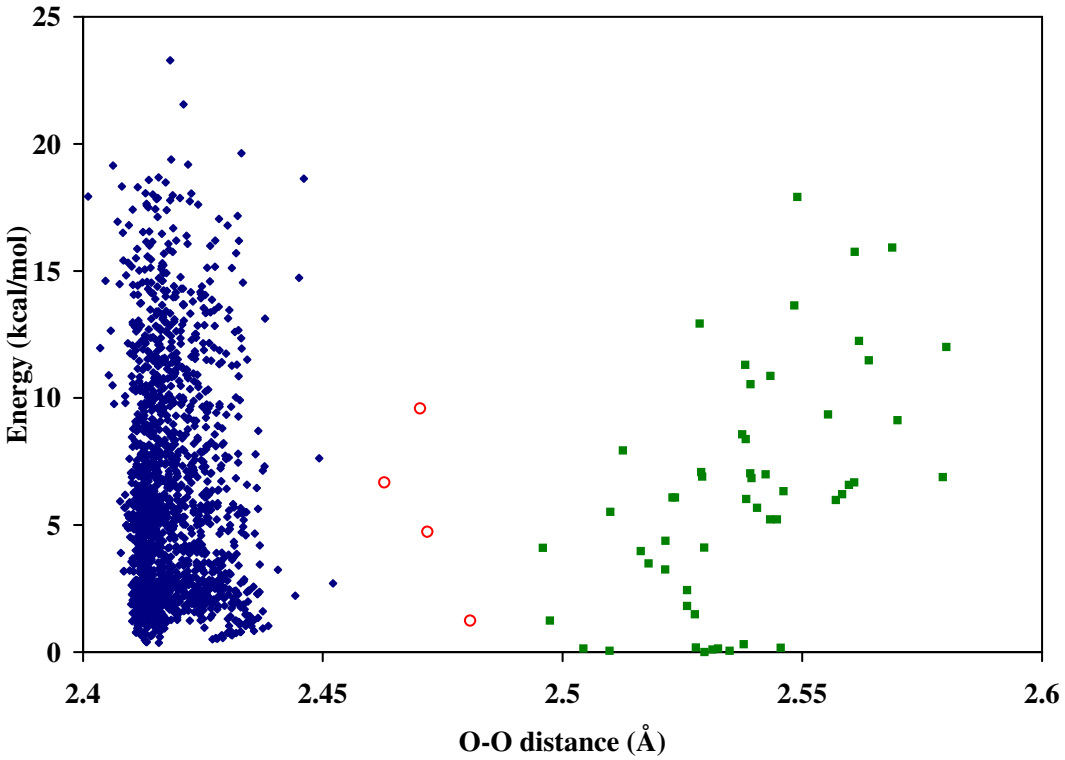

Figure 29: OO distances of 1714 potential energy minima of $H^+(H_2O)_{21}$ determined using basin hopping Monte Carlo optimization with the SCC-DFTB+D method. The Zundel-like structures (OO distance of 2.4 $\sim$ 2.45 Å) are denoted by dark-blue diamonds, and the Eigen-like structures (OO distance of 2.5 $\sim$ 2.58 Å) are indicated by green squares. The intermediate structures are indicated with open-red circles.

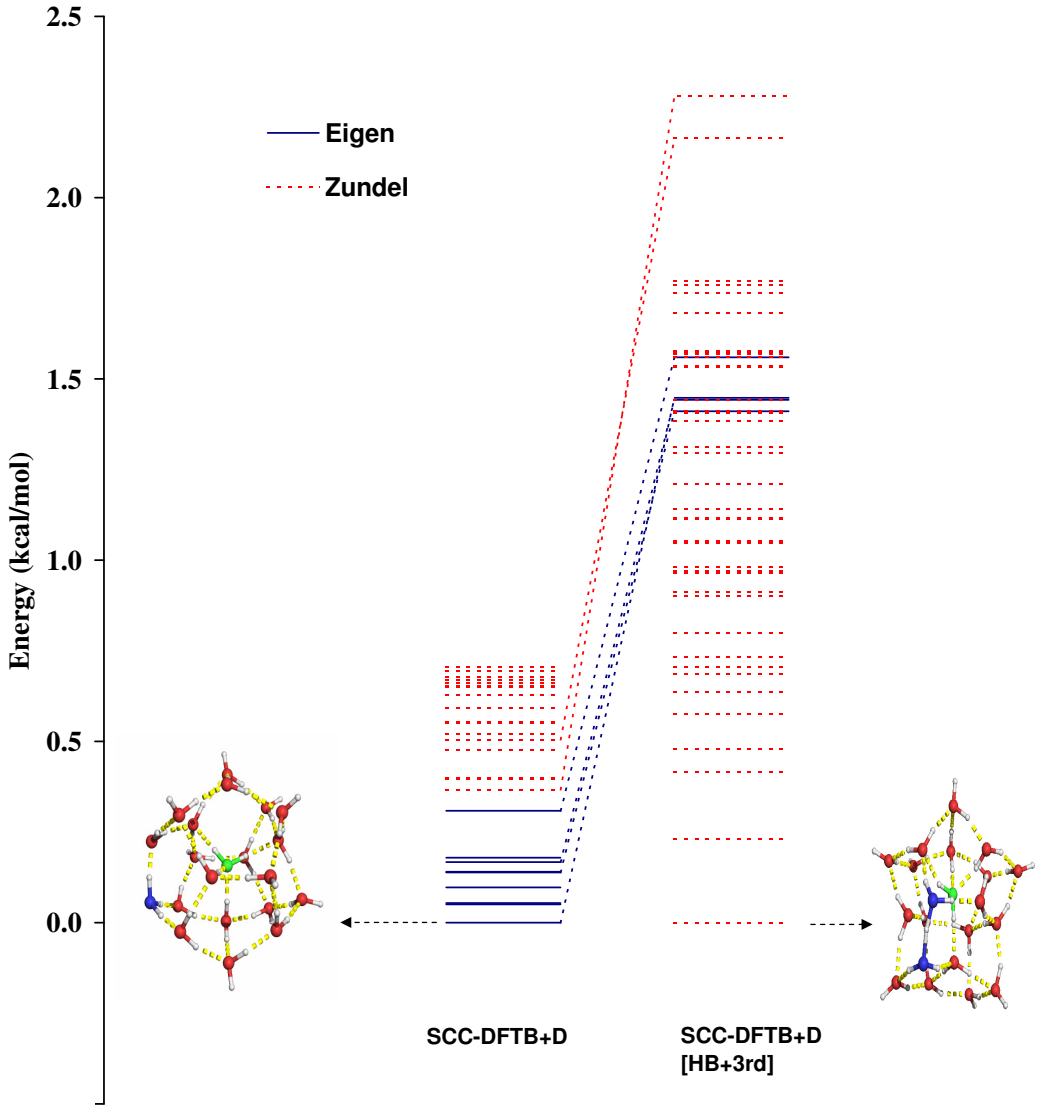

Figure 30: Low-energy local minima of $H^+(H_2O)_{21}$ determined using basin hopping Monte Carlo optimization with the SCC-DFTB+D and SCC-DFTB+D[HB+3rd] methods.

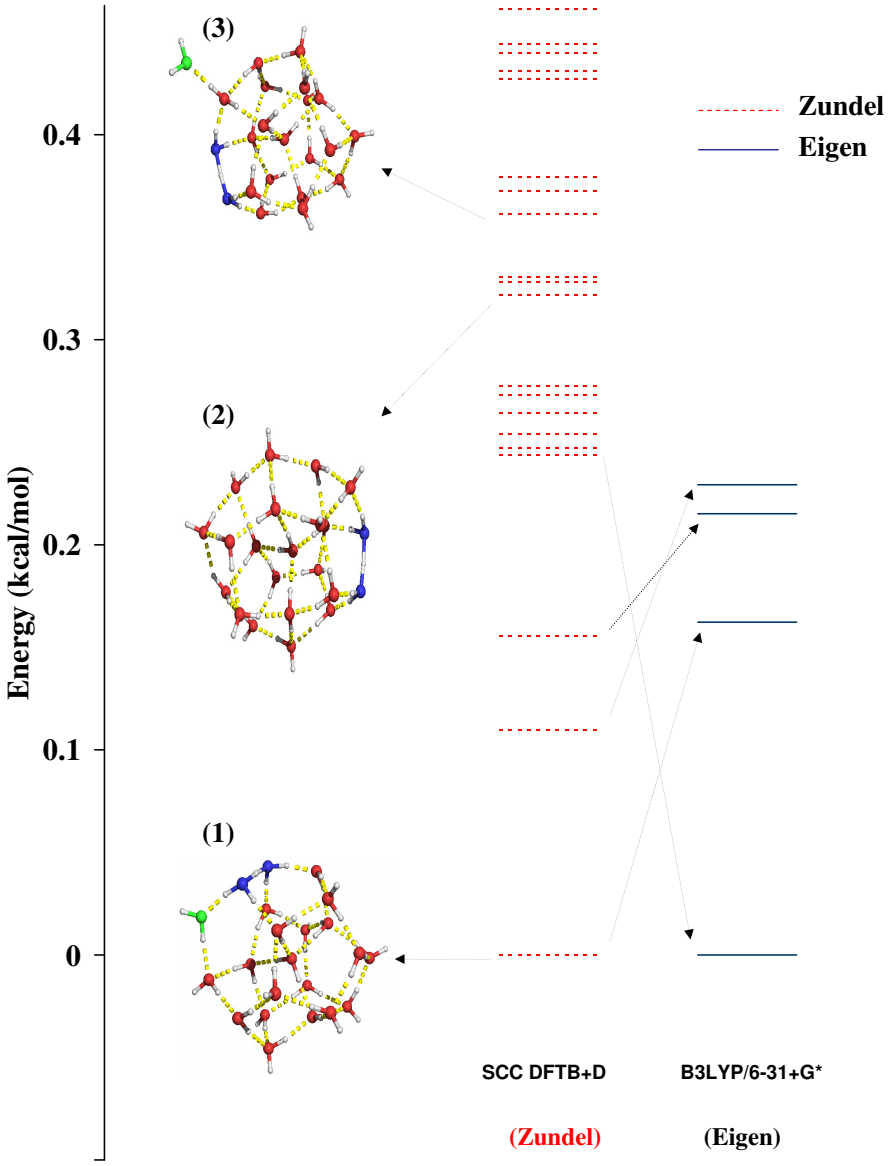

Figure 31: Low-lying potential energy minima of $H^+(H_2O)_{22}$ determined using basin hopping Monte Carlo optimization with the SCC-DFTB+D method. The four lowest energy Zundel structures found with the SCC-DFTB+D method were reoptimized with the B3LYP method and found to collapse to Eigen structrures.

method without H-bonding and 3^{rd} order corrections. However, for $H^+(H_2O)_{21}$ the bias toward Zundel structures is actually more severe in the SCC-DFTB+D[HB+3rd] approach. We have also applied the two SCC-DFTB+D methods to selected isomers of the neutral $(H_2O)_{21}$ cluster and find that these approaches have errors in the relative energies of different isomers as large as 6.2 kcal/mol, compared to large-basis set RIMP2 calculations. [169] Clearly, part of the problem in describing the $H^+(H_2O)_n$ clusters with the SCC-DFTB+D methods stems from the failure of these approaches to accurately describe the neutral water networks. This study reflects the need for a further extension of the SCC-DFTB method to enhance its usefulness at describing uncharged and protonated water clusters.

8.0 SUMMARY

The development of models for describing excess electrons interacting with water clusters has been an active research field in our group for the last ten years. The Drude model initially introduced Wang *et al.* [65, 27, 28] has been improved both in accuracy and computational speed. By employing the distributed point polarizable water model (DPP) developed by DeFusco *et al.* [66] instead of the Dang-Chang water model [36], the energetics has been considerably improved. [31] Also one-electron polarization models (OEPM) for $(H_2O)_n^-$ have been derived by applying an adiabatic approximation to the Drude/DPP approach. These greatly reduce the computational cost in the calculations of the electron binding energies (EBE) for $(H_2O)_n^-$ clusters. [33]

In this thesis, analytical gradients for the OEPM-GTO method have been implemented. This implementation has permitted a detailed characterization of the potential energy surfaces (PES) of the $(H_2O)_n^-$, n = 6, 7, and 8, clusters. The minimum energy pathways proceeding from the neutral isomers to the observed AA isomers for the $(H_2O)_6^-$ and $(H_2O)_7^-$ clusters have been identified. Also, mechanisms for forming the lowest energy AA isomers of the $(H_2O)_8^-$ cluster by condensation of H_2O on dominant $(H_2O)_7^-$ isomers have been analyzed.

In addition, a sine-type DVR basis implementation of the OEPM method has been developed. For a cluster the size of $(H_2O)_{45}^-$, the OEPM-DVR method achieves about an order of magnitude in reduction in the CPU time compared to calculations with GTO basis sets with no loss of accuracy.

Although the potential energy surfaces of the $(H_2O)_n^-$, n = 6, 7, and 8 clusters have

been characterized using the OEPM-GTO method, the mechanism for the formation of the AA anion observed experimentally is still unclear. This could be addressed by means of molecular dynamics simulations. The challenge here will be to run the simulations for the long times required to explore the rearrangements. This should be feasible with the parallel version of the OEPM-DVR code. It would also be useful to couple the OEPM method with the newly developed DPP2 water model [170], which gives more accurate energetics for the neutral clusters. Furthermore, the OEPM-DVR method should be extended to address the properties of the excess electron in bulk water.

The SCC-DFTB method is an alternative to the use of force fields for describing the neutral and protonated water clusters together. In this thesis, the thermodynamic properties of the $(H_2O)_8$ cluster have been calculated using PTMC simulations with the SCC-DFTB method. Inclusion of the H-bond plus 3rd order corrections in the SCC-DFTB approach improves the agreement with the predictions of *ab initio* calculations. However, for the protonated water clusters, $H^+(H_2O)_{21}$ and $H^+(H_2O)_{22}$, the bias toward Zundel structure is actually more severe in the SCC-DFTB+D[HB+3rd] approach.

A major limitation of the SCC-DFTB method for describing neutral and protonated water clusters appears to be the underestimation of the polarization energy. Multiple strategies are possible for addressing this shortcoming, including the extension of SCC-DFTB method to include the effect of polarization functions.

APPENDIX A

CONFORMATIONAL ANALYSIS OF A FLEXIBLE BICHROMOPHORE: 3-(4-HYDROXYPHENYL)-N-BENZYL-PROPIONAMIDE (HNBPA)

This work has been published as Ref. [171]

A.1 INTRODUCTION

Bichromophoric systems are especially useful for examining the effects of electronic coupling. 3-(4-hydroxyphenyl)-N-benzyl-propionamide (HNBPA) is a biologically relevant single chain bichromophore molecule that contains two spectroscopically distinguishable ultraviolet chromophores. The phenyl and phenol chromophores are connected by a chain six bonds long containing an amide group (Figure 32). In Professor Zwier's group, the spectra of several conformers of HNBPA have been obtained by using one-color resonant two-photon ionization(R2PI) [172], UV-UV hole-burning [172], and dispersed fluorescence.

A major challenge in interpreting the spectra is the identification of the isomers responsible for the observed transitions. Here electronic structure calculations can be valuable. I have optimized the geometries of eight conformers of HNBPA and have calculated the vibrational frequencies of these conformers using several electronic structure methods.

A.2 CONFORMATIONAL ANALYSIS WITH ELECTRONIC STRUCTURE METHODS

Fig. 33 depicts the geometries of the conformers of HNBPA optimized using the RIMP2 electronic structure method with the aug-cc-pVDZ [169] basis set. In this figure, 'fol' and 'ext' denote the folded and extended structures respectively, 'fac' and 'per' indicate whether the planes of the rings face each other or are perpendicular to one another, and 'TNH' or 'CNH' refer to the position of the N-H group in the chain with respect to the O-H group in the phenol chromophore, either cis or trans. The optimizations were carried out in three steps: first at the B3LYP/6-31+G(d) level, then at the MP2/6-31+G(d) level, and finally at the RIMP2/aug-cc-pVDZ level. The B3LYP and MP2 calculations were carried out using Gaussian 03, and the RIMP2 calculations were carried out using the TURBOMOLE program [173].

In Figure 34, the relative energies of the conformers calculated with various electronic structure methods are shown. Single-point energies were calculated using the RIMP2/aug-cc-pVTZ method with RIMP2/aug-cc-pVDZ optimized geometries. We also checked the reliability of SCC-DFTB+D(HB+3rd) semiempirical electronic structure method [91,92,93, 94,95,96,98,99] for characterizing HNBPA.

Whereas the calculations with the HF method favor the extended structures, the opposite behavior is found with the MP2 method. The Becke3LYP method gives results intermediate between the HF and MP2 results. Interestingly, the SCC-DFTB+D(HB+3rd) method qualitatively reproduces the trend found in the MP2 calculations, whereas the SCC-DFTB(HB+3rd) method without the dispersion correction gives results similar to the Becke3LYP method. Clearly, dispersion interactions play a major role in determining the relative stability of the folded and extended structures.

Vibrational frequencies of the eight conformers of HNBPA shown above were calculated with each of the SCC-DFTB+D(HB+3rd), MP2/6-31+G(d), and RIMP2/aug-cc-pVDZ methods. Table 4 and 5 summarizes the lowest 10 vibrational frequencies of the four ex-

tended structures, and Table 6 and 7 reports the corresponding results for the four folded structures. With the SCC-DFTB+D(HB+3rd) and RIMP2 methods, the second derivatives were generated by numerical differentiation of the analytical first derivatives.

A.3 CONFORMATIONAL SPECIFIC SPECTROSCOPY

Professor Zwier's group has studied HNBPA using one-color resonance two-photon ionization (R2PI), UV-UV hole-burning(HB), and resonant ion dip infrared (RIDIR) spectroscopies. [172] R2PI and UV-UV HB permit conformation-specific excitation and detection, taking advantage of the unique infrared and ultraviolet signatures of the individual conformations when cooled in a supersonic expansion. Figure 35 shows the spectra of two conformers of HNBPA using R2PI along with UV-UV HB results. The S_1 origins, which arise from the phenol chromophore, are spread over 200 cm^{-1}, with the dominant conformers exhibiting extensive low-frequency vibronic structure.

Figure 36 shows the tentative assignment of the HB spectra of conformers A and B of HNBPA. The structure in the spectrum of A derives from combinations of modes with frequencies of 25 and 45 cm^{-1}, and that in the spectrum of B derives from combination bands envolving modes with frequencies of 16 and 18 cm^{-1}.

The Zwier group also obtained emission spectra by using a monochromator to disperse the fluorescence. The dispersed fluorescence spectra of conformers A and B are shown in Figure 37. The spectrum of conformer B does not show as many peaks as that of conformer A, leading us to conclude that the geometry distortion upon electronic excitation is much greater in A than B.

We also assign the vibrational frequencies of conformers A and B of HNBPA in the ground state using the observed dispersed fluorescence spectra (see Figure 37). The spectrum of conformer A is characterized by four progressions (α_n^0, β_n^0, $\alpha_1^0\beta_n^0$, $\alpha_2^0\beta_n^0$) with vibrational intervals of 19 (α_1^0) and 27 cm^{-1} (β_1^0). For the conformer B, four fundamentals, 26 (β_1^0),

48 (γ_1^0), 462 (δ_1^0), and 822 cm^{-1} (ϵ_1^0), were observed together with progressions of β and γ. After analyzing the vibrational motions of the four folded structures, we conclude that the second lowest vibrational mode, 27 cm^{-1} (β_1^0) of conformer A is corresponds to the first lowest vibrational mode, 26 cm^{-1} (β_1^0) of conformer B.

A.4 CONCLUSION

In this study, double resonance spectroscopy has been used to record the infrared and ultraviolet spectra of single conformation of the model flexible bichromophore, HNBPA. Relative energies of eight low-energy conformers of HNBPA have been calculated by using several different electronic structure methods. More detail analysis with amide NH and OH stretch frequencies is explained in Ref. [171]

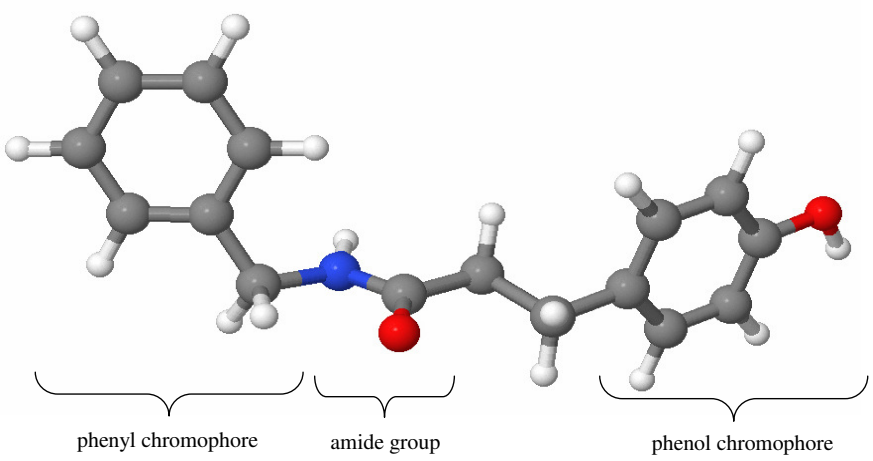

Figure 32: 3-(4-hydroxyphenyl)-N-benzyl-propionamide(HNBPA)

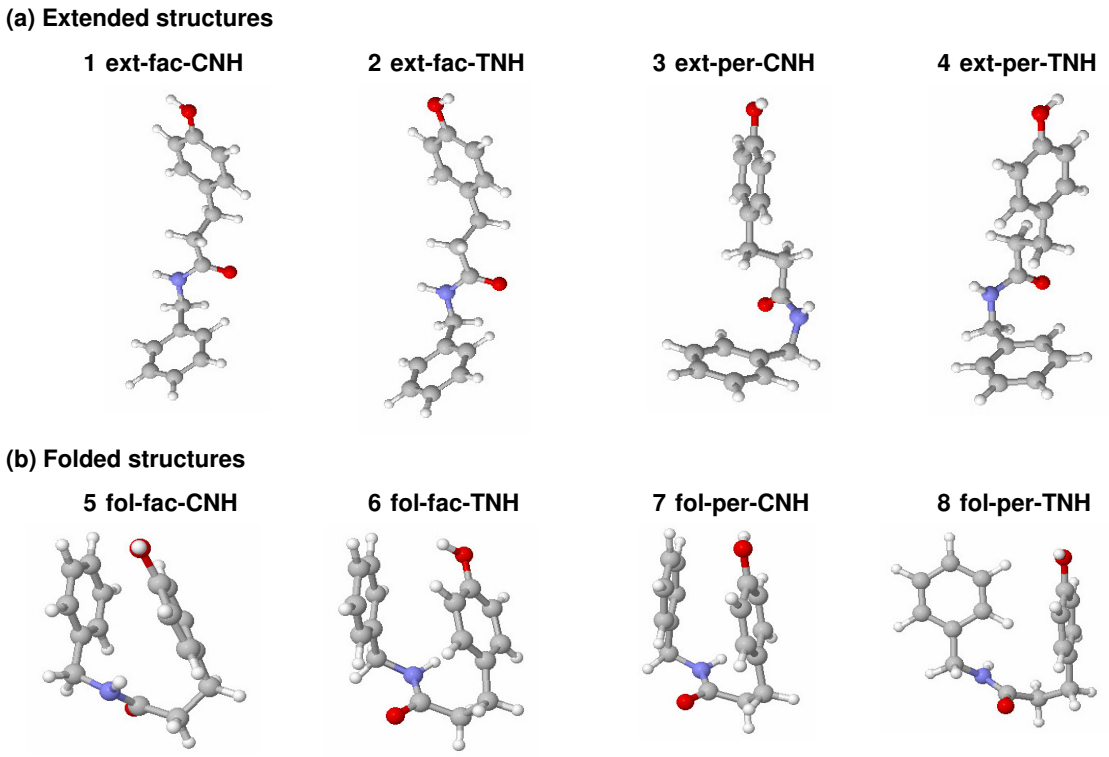

Figure 33: RIMP2/aug-cc-pVDZ optimized geometries of the eight isomers of HNBPA

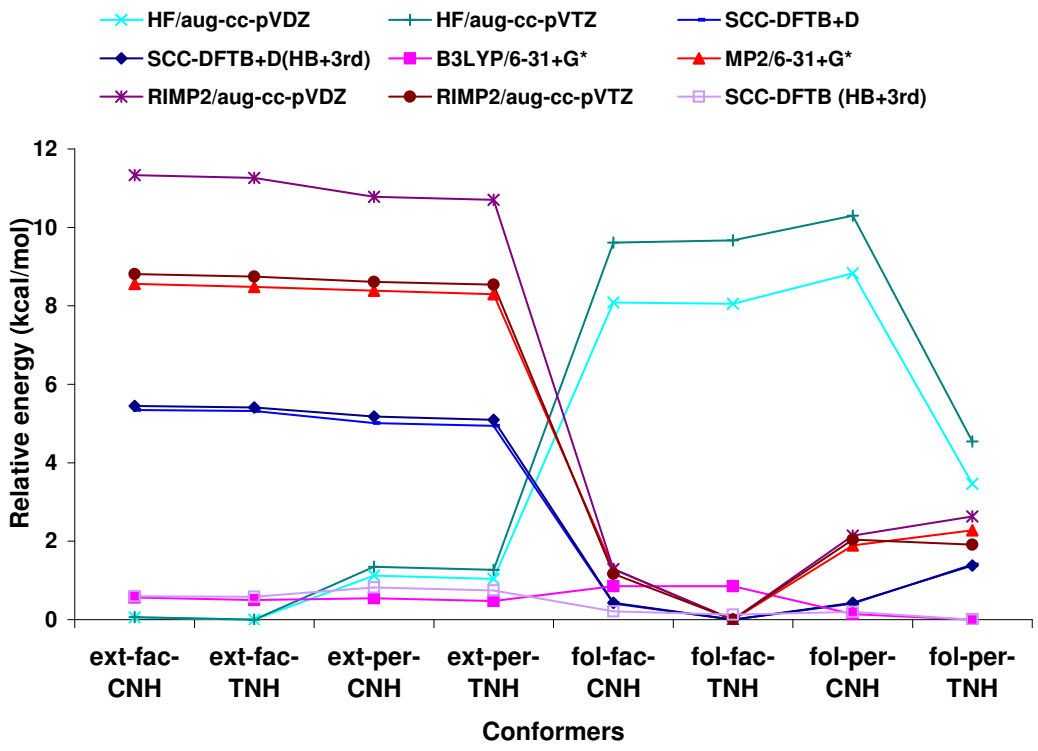

Figure 34: Relative energies of the eight conformers of HNBPA, calculated with several electronic structure methods.

Table 4: Relative energies (kcal/mol) an the 10 lowest vibrational frequencies (cm^{-1}) of the ext-fac-CNH and ext-fac-TNH structures of HNBPA, calculated with the MP2/6-31+G*, RIMP2/aug-cc-pVDZ(aDZ), and SCC-DFTB+D(HB+3rd) electronic structure methods.

	ext-fac-CNH			ext-fac-TNH		
	MP2/ 6-31+G*	RIMP2/ aDZ	SCC-DFTB+D (HB+3rd)	MP2/ 6-31+G*	RIMP2/ aDZ	SCC-DFTB+D (HB+3rd)
E_{rel}	8.56	11.33	5.45	8.48	11.26	5.41
Freq.	11.97	6.92	6.34	12.37	7.48	11.16
	19.62	20.02	12.62	19.64	20.09	13.76
	24.71	20.61	17.74	24.76	20.46	19.08
	38.62	35.68	26.32	30.03	36.20	29.25
	48.94	49.73	35.18	46.72	48.90	41.30
	69.68	69.98	63.33	69.27	69.78	60.96
	71.50	73.48	66.87	70.72	72.72	73.34
	145.64	145.48	133.76	146.29	145.99	136.72
	173.54	173.39	175.56	173.37	173.27	175.36
	189.47	192.50	182.80	190.27	193.32	184.89

Table 5: Relative energies (kcal/mol) an the 10 lowest vibrational frequencies (cm^{-1}) of the ext-per-CNH and ext-per-TNH structures of HNBPA, calculated with the MP2/6-31+G*, RIMP2/aug-cc-pVDZ(aDZ), and SCC-DFTB+D(HB+3rd) electronic structure methods.

	ext-per-CNH			ext-per-TNH		
	MP2/ 6-31+G*	RIMP2/ aDZ	SCC-DFTB+D (HB+3rd)	MP2/ 6-31+G*	RIMP2/ aDZ	SCC-DFTB+D (HB+3rd)
E_{rel}	8.39	10.78	5.18	8.30	10.70	5.10
Freq.	9.61	11.32	10.70	9.70	9.16	8.87
	17.01	14.91	15.07	16.61	15.91	13.15
	21.22	20.84	20.06	20.95	22.05	19.98
	36.01	35.36	23.05	35.29	35.12	21.70
	57.08	59.28	41.33	55.15	58.63	41.34
	62.41	65.94	55.84	62.40	66.31	56.21
	79.44	82.79	68.47	79.20	82.48	68.07
	137.45	137.57	143.77	137.42	137.51	143.47
	181.62	186.00	184.35	181.95	186.21	184.58
	211.67	210.49	197.47	211.84	210.67	197.76

Table 6: Relative energies (kcal/mol) and the 10 lowest vibrational frequencies (cm^{-1}) of the fol-fac-CNH and fol-fac-TNH structures of HNBPA, calculated with the MP2/6-31+G*, RIMP2/aug-cc-pVDZ(aDZ), and SCC-DFTB+D(HB+3rd) electronic structure methods.

	fol-fac-CNH			fol-fac-TNH		
	MP2/ 6-31+G*	RIMP2/ aDZ	SCC-DFTB+D (HB+3rd)	MP2/ 6-31+G*	RIMP2/ aDZ	SCC-DFTB+D (HB+3rd)
E_{rel}	1.29	1.29	0.43	0.00	0.00	0.00
Freq.	24.37	28.56	9.57	29.26	33.35	9.65
	36.94	37.12	27.69	47.01	43.69	29.48
	45.17	57.12	37.21	53.43	63.86	36.23
	58.67	69.84	44.86	70.60	76.98	44.19
	75.86	88.65	58.67	80.73	91.02	59.40
	96.21	122.33	74.85	102.75	112.77	76.63
	112.63	126.52	116.81	116.39	127.36	116.18
	139.81	140.95	134.19	142.61	145.17	131.97
	177.62	184.92	175.31	179.66	185.58	174.64
	225.29	218.25	219.03	226.45	218.51	219.25

Table 7: Relative energies (kcal/mol) and the 10 lowest vibrational frequencies (cm^{-1}) of the fol-per-CNH and fol-per-TNH structures of HNBPA, calculated with the MP2/6-31+G*, RIMP2/aug-cc-pVDZ(aDZ), and SCC-DFTB+D(HB+3rd) electronic structure methods.

	fol-per-CNH			fol-per-TNH		
	MP2/ 6-31+G*	RIMP2/ aDZ	SCC-DFTB+D (HB+3rd)	MP2/ 6-31+G*	RIMP2/ aDZ	SCC-DFTB+D (HB+3rd)
E_{rel}	1.89	2.14	0.43	2.27	2.63	1.38
Freq.	30.02	30.23	7.51	23.92	20.68	9.88
	44.12	51.32	27.97	29.44	29.11	25.48
	50.03	54.23	37.02	46.87	53.19	36.37
	60.83	69.20	44.74	59.96	73.29	41.09
	61.78	79.95	58.36	69.02	79.12	59.19
	100.26	113.04	74.65	79.66	98.42	67.89
	129.04	140.33	116.94	114.99	116.12	97.09
	145.67	145.95	134.22	151.43	154.53	137.51
	175.87	180.62	175.45	184.42	192.48	186.46
	234.35	229.20	218.39	221.92	217.54	206.14

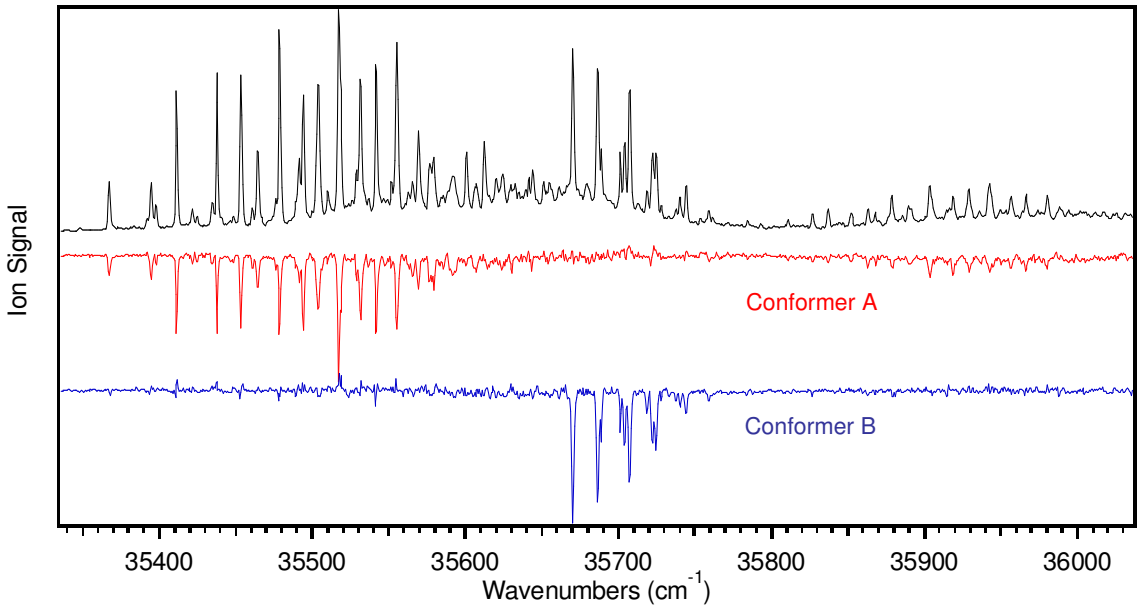

Figure 35: R2PI and HB spectra of conformers A and B of HNBPA (from Prof. T. Zwier)

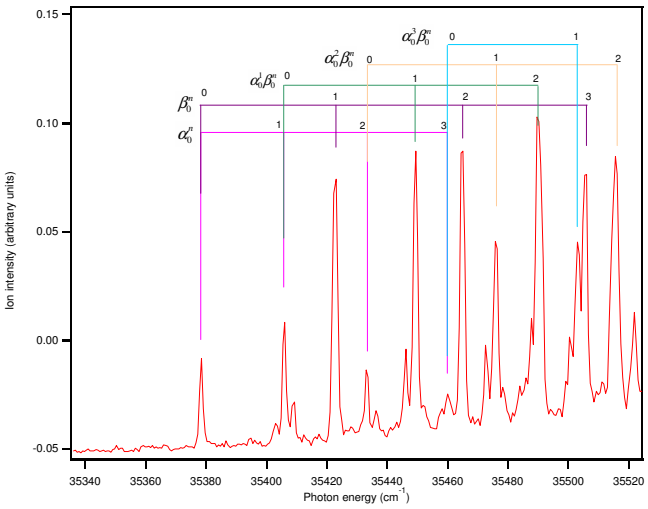

(a) Assignment of HB spectrum of conformer A of HNBPA

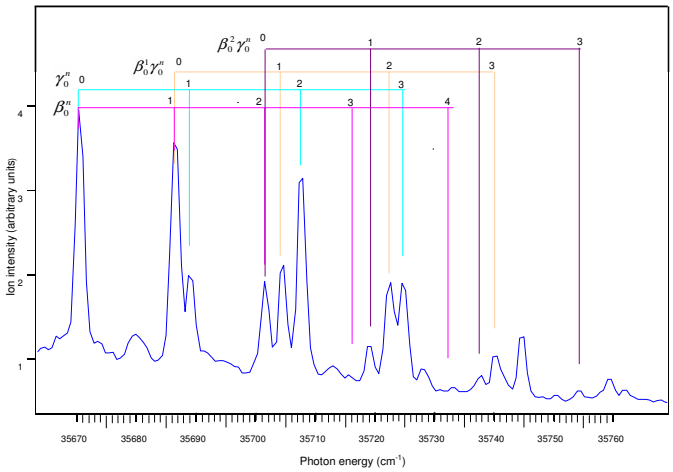

(b) Assignment of HB spectrum of conformer B of HNBPA

Figure 36: HB spectra of conformers A and B of HNBPA and the progressions of 28 (α_0^1) and 45 cm^{-1} (β_0^1) for the conformer A (a), and those of 16 (β_0^1) and 18 cm^{-1}(γ_0^1) for the conformer B (b).

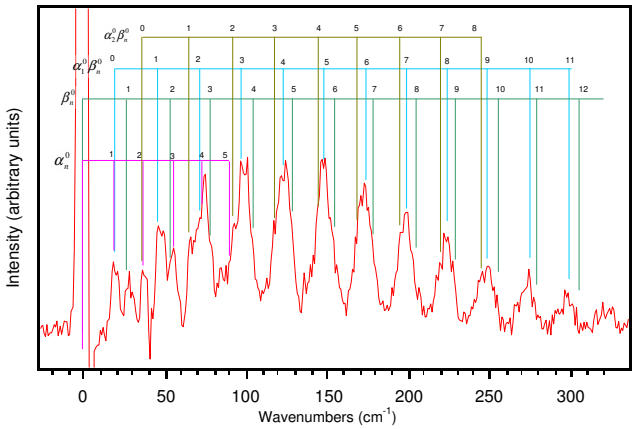

(a) Dispersed fluorescence of conformer A of HNBPA, together with the assignment of the vibrational structure.

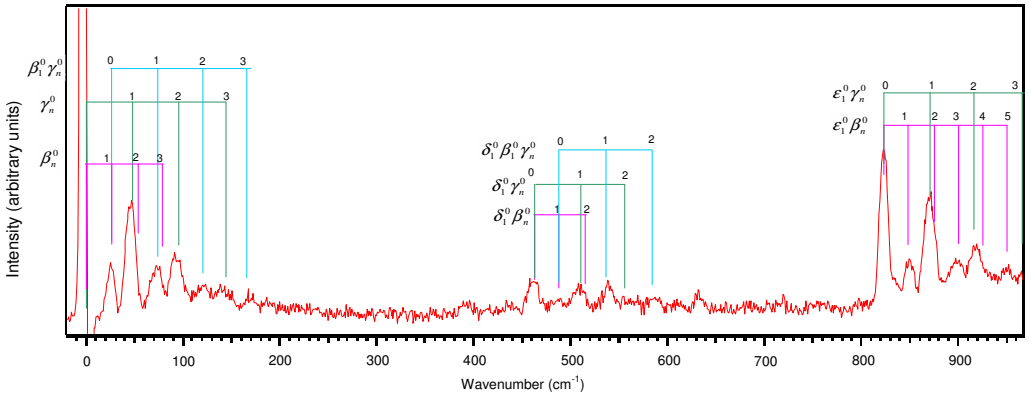

(b) Dispersed fluorescence of conformer B of HNBPA, together with the assignment of the vibrational structure.

Figure 37: Dispersed fluorescence spectra of conformer A and B of HNBPA (from Prof. T. Zwier) and the progressions of 19 (α_1^0) and 27 cm^{-1} (β_1^0) for the conformer A (a), and those of 26 (β_1^0) and 48 cm^{-1} (γ_1^0) for the conformer B (b).

APPENDIX B

MODELING CHARGE PENETRATION EFFECTS IN WATER-WATER INTERACTIONS

B.1 INTRODUCTION

Over the last few years, a large number of new water model potentials have been introduced. [174, 36, 37, 35, 66] A correct treatment of the electrostatic interactions has emerged as a central point in the development of these potentials. Although several popular water models such as TIP4P [174], DC [36], TTM$_n$-R [37], and AMOEBA [35] have described successfully the relative energies of water clusters, none of them consider charge penetration effects [175] that are important for short-range electrostatic interactions. Most of these models use a classical point-charge representation of electrostatics. The AMOEBA model also includes the multipolar expansions to improve the electrostatic description. Unfortunately, the inclusion of higher order moments does not describe the charge penetration effects observed when continuous charge distributions interact.

To illustrate the idea of charge penetration, Figure 38 shows the overlap of charge densities that occurs when two water molecules are in close proximity. The electrostatic interaction between these two species is no longer well represented by methods such as Stone's distributed multipolar analysis (DMA) [175] as the nuclei on one molecule are no longer shielded by its own electron density, thus experience a greater attraction for the electron density associated

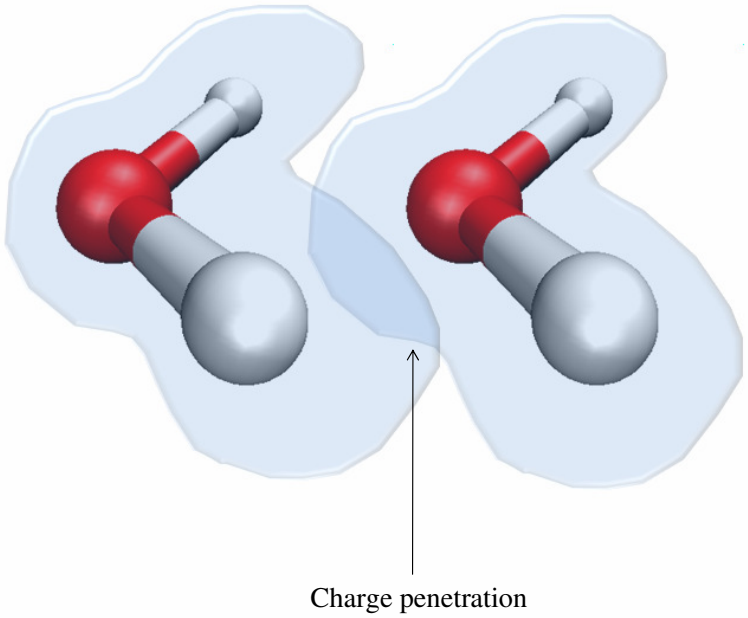

Figure 38: Schematic description of charge penetration for two water molecules.

with the other species. The energy resulting from this increased attraction is referred to as charge penetration.

One way of dealing with charge penetration is to introduce a screening function as a pre-factor to the Coulomb potential. [176,177,178,179] However, this method is limited due to the absence of nuclear-electron interactions. An alternative method is to fit *ab initio* properties to Gaussian auxiliary basis sets (ABSs) centered on specific molecular sites. [180, 181, 182, 183] This method can accurately generate the Coulomb interaction energies and explicitly considers nuclear charge and electron densities. The *ab initio* calculated electron density can be fit with a number of basis function of differing angular momentum, but ABSs are usually restricted to *s*-type Gaussian functions due to the computational demand.

In the present study, three Gaussian electrostatic models have been tested: Model1 has one *s*- Gaussian type function (GTF) located at each of five sites, Model2 has one *s*-GTF at each of three sites, and Model3 has two *s*-GTFs at each of three sites. The coefficients and exponents of the Gaussian functions of the auxiliary basis sets are fitted to the MP2/aug-cc-pVTZ electrostatic potential. The validity of the three models has been examined by calculating the intermolecular Coulomb interactions for several stationary points on the water dimer potential energy surface.

B.2 METHODOLOGY

B.2.1 Models

Figure 39 compares the DPP water model and the three different GEMs considered in this work. Model1 employs five sites one on each atom and D sites, located above and below the HOH plane. The geometry of Model1 is taken from the SAPT-5S model [184] which is a rigid model based on the vibrational averaged geometry. The positions of the D sites were optimized to get a better fit to the electrostatic energy. Nuclear point charges of Mode1 are

located on Oxygen and each Hydrogen with +6 and +1, respectively. Model2 locates three s-GTFs at the Hydrogens as well as at the M site, which is displaced along the HOH bisector. Darden *et al.* have already tested a similar three-site model, where the GTFs were located at the Oxygen and two Hydrogen sites [183]. This resulted in a water monomer dipole moment of about 1.9∼2.0 Debye, much higher than the experimental result (1.855 Debye). Model3 places two s-GTFs at each of the three sites of Model2. Nuclear point charges of both of Model2 and Model3 are placed on M and each Hydrogen with +6 and +1, respectively. The locations of D and M sites of GEMs are determined as part of the fit to the electrostatic potential.

The electrostatic interaction energy for the DPP water model (classical point-charge representation) is given by

$$E_{DPP}^{elec} = \sum_i \sum_j \frac{Q_{A_i} Q_{B_j}}{r_{A_i B_j}}, \tag{B.1}$$

where Q_{A_i} and Q_{B_j} represent the point charges at i and j sites of two different monomers A and B, respectively. For the GEMs a more detail description of the intermolecular Coulomb energy is required and nucleus-nucleus (N-N), nucleus-electron (N-e), and electron-electron (e-e) contributions must be considered.

$$E_{intermol} = E_{N-N} + E_{N-e} + E_{e-e}. \tag{B.2}$$

The following expression gives the intermolecular Coulomb interactions in the GEM model.

$$\begin{aligned} E_{GEM}^{elec} &= \sum_i \sum_j \frac{Z_{A_i} Z_{B_j}}{r_{A_i B_j}} + \sum_i \int \frac{Z_{A_i} \rho^B(r_2)}{r_{A_i 2}} dr_2 \\ &+ \sum_j \int \frac{Z_{B_j} \rho^A(r_1)}{r_{B_i 1}} dr_1 + \int \int \frac{\rho^A(r_1) \rho^B(r_2)}{r_{12}} dr_1 dr_2 \end{aligned} \tag{B.3}$$

The first term represents the nucleus-nucleus interaction, the second and third terms are the nucleus-electron contributions, and the last term is the electron-electron interaction. Z_{A_i} and Z_{B_j} represent the nuclear charges of atoms i and j on molecule A and B, respectively. Only valence nucleus charges are considered, +6 and +1 for the Oxygen and Hydrogen,

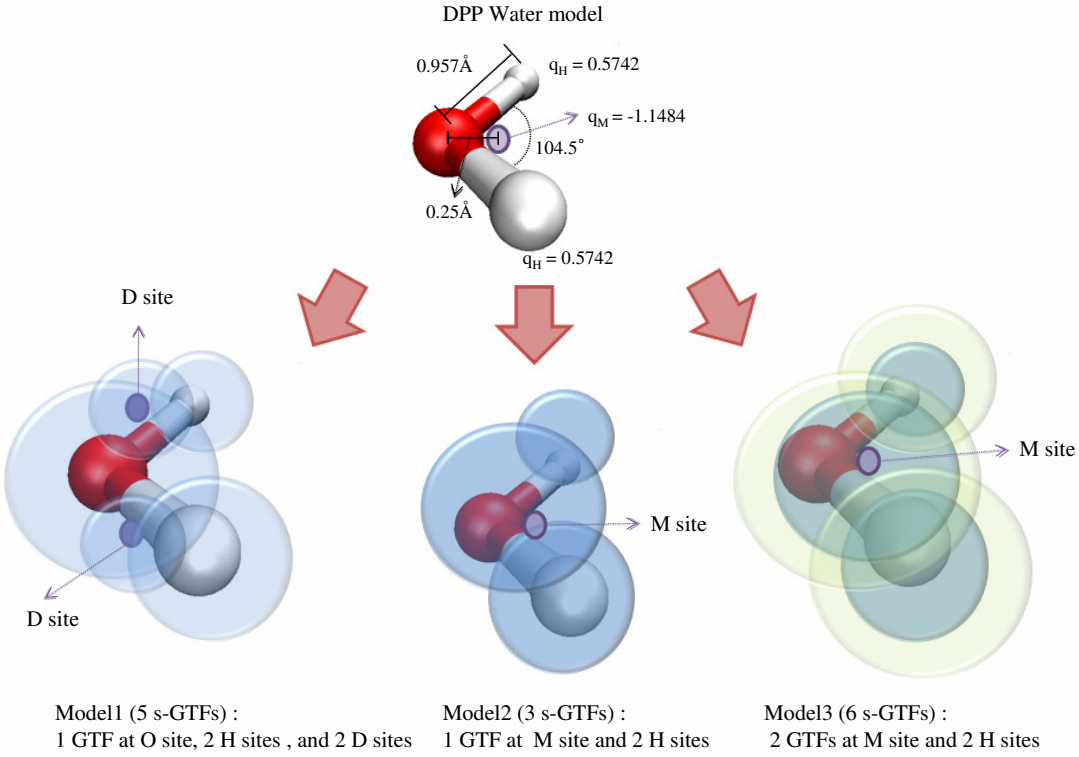

Figure 39: Gaussian electrostatic models: Model1, Model2, and Model3 have 5, 3, and 6 s-type Gaussian functions, respectively.

respectively. ρ^A and ρ^B represent the Gaussian electron densities of molecule A and B, respectively.

B.2.2 Fitting procedure

I followed the fitting procedure of Darden *et al* [183]. In that work, Gaussian electron densities were found through fits to several molecular properties: density, ESP (Electrostatic potential), and electric field. The least-square method is used to get the optimized coefficients and exponents of the Gaussian functions by minimizing the following fitting function.

$$\chi^2 = \sum_{\alpha} w_\alpha \sum_i W(r_i)(y_\alpha(r_i) - y_\alpha(r_i, c_k))^2 \tag{B.4}$$

where $y_\alpha(r_i)$ corresponds to the *ab initio* molecular property of interest at point i, $y_\alpha(r_i, c_k)$ is the same property evaluated with the kth ABS element at the same point on the grid, and α denotes the molecular properties of interest. w_α is the relative weight for property α, and W(r) is the weighting function for the point on the grid, as suggested by Bayly *et al.* [185] and defined as :

$$W(r) = \exp[-\sigma(\log \rho(r) - \log \rho_{ref})^2] \tag{B.5}$$

in which $\rho(r)$ is the predefined electron densities, and ρ_{ref} is a reference electron density whose values are chosen in combination with σ to ensure the weighting function behaves as expected. Equation B.4 is minimized by using LBFGS optimization methods using analytical gradients with respect to the coefficients and exponents of the Gaussian functions.

B.3 RESULTS

In this work, the Gaussian coefficients and exponents were fit to the MP2/aug-cc-pVTZ ESP. Figure 40 shows the points at which the ESP was fitted. Due to the symmetry of the

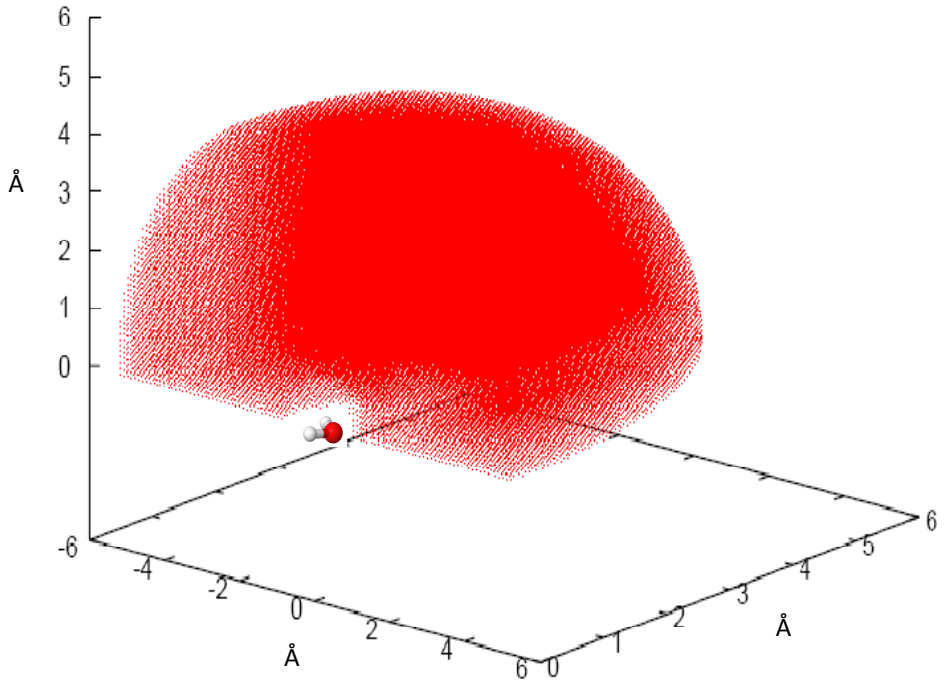

Figure 40: The data points (157412 points) used for fitting the MP2 ESP of the water monomer.

water monomer, the points span 1/4 of the space. As suggested by Darden [183], minimum cutoff values of 1.5 and 1.7 bohr were used for Hydrogen and Oxygen, respectively, and maximum cutoff values of 10 bohr with the grid point 0.1 Å were used. This brings the total number of data points to 157412.

The D sites of Model1, which are located out of the HOH plane, are optimized along with fitting the auxiliary basis set (ABS), so that the positions of D sites are different from original locations of the SAPT-5S model. Figure 41 shows the geometry of the SAPT-5S model and the positions of the D sites for Model1 as well as the M sites for Model2 and Model3. The M sites of Model2 and Model3 were placed to 0.1 Å from Oxygen, along the HOH bisector after a trial and error method.

The optimized coefficients and exponents of the Gaussian type functions (GTFs) as well as the dipole moments of Model1, Model2, and Model3 are shown in Table 8. The dipole moment of Model1 is very close to the experimental value, 1.855 Debye, [186] while those of Model2 and Model3 are under-estimated and over-estimated, respectively.

B.3.1 Electrostatic potential

In order to assess the fitting performance of the three different models for representing the electrostatic potential of each water monomer, I report the difference between the electrostatic potential associated with each model and that calculated at the MP2/aug-cc-pVTZ level of theory as a function of distance. Figure 42 shows the difference contours at the ± 0.5 kcal/mol level at points in the plane of the water monomer. The ± 0.5 kcal/mol contours were chosen for display because they represent a sizable (10%) portion of the net binding energy of the water dimer.

A 0.5 kcal/mol difference in ESP occurs at around ± 3.5 Å distance from the center of mass when using the DPP model. While 0.5 kcal/mol contour lines of the ESP differences in Model1 are located near ± 3.0 Å, those in Model2 and Model3 are presented near ± 4.5 Å. Compared to the DPP water model, only Model1 shows better performance. Model2

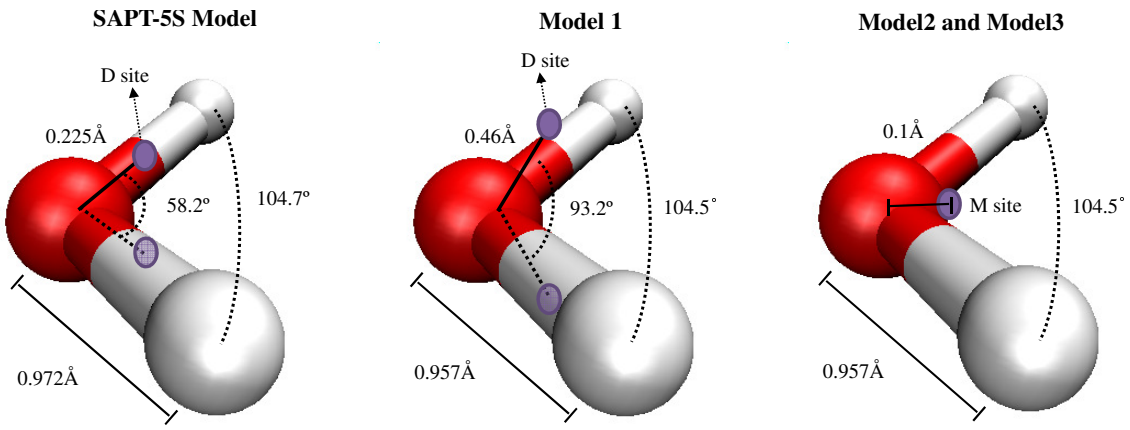

Figure 41: Original SAPT-5S model and optimal geometry of the Model1, and the geometries of Model2 and Model3.

and Model3 perform worse than the DPP water model in the analysis of the electrostatic potential difference of the water monomer.

B.3.2 Water dimer

Figure 43 displays the electrostatic interaction energy of the water dimer as a function of the Oxygen-Oxygen separation between these two water monomers (R_{OO}) for each model considered. In generating this plot, the monomers were kept rigid with OH bond lengths and HOH angles fixed at the values found experimentally for the gas-phase monomer. The flap angles that determine the orientation of these two monomers with respect to the O-O axis were frozen at the values they have for the MP2/aug-cc-pVTZ optimized structure.

I compare the electrostatic interaction energy of the water dimer with the values obtained from symmetry adapted perturbation theory (SAPT) [187, 188, 189] with the aug-cc-pVTZ basis set as a reference. The energy of the DPP water model is under-estimated at short O-O distances. Most classical water models such as TTM2-R, DC, and AMOEBA give nearly the same electrostatic interaction energies as the DPP water model. [66] While this is a limitation of the classical model for expressing the electrostatic energies at short distances since these models do not account for charge penetration effects, the Gaussian electrostatic models are able to account for these effects.

The electrostatic energy of Model2 is over-estimated in the region, $R_{OO} \leq 2.8$ Å, but under-estimated in the region, $R_{OO} > 2.8$ Å. Mode1 and Model3 show a better electrostatic energy of the dimer than Model2 because these models used five and six Gaussian type functions to describe the electron density, respectively. In the region, $R_{OO} > 2.7$ Å, the electrostatic energies of Model1 are almost the same as those of the SAPT calculation. On the other hand, the electrostatic energy of Model3 is in good agreement with that from the SAPT calculation at short OO distances.

B.3.3 The ten Smith water dimers

As a more general test for the water dimer, ten stationary points of the water dimer potential energy surface (PES) were considered. Figure 44 shows the geometries of the ten stationary points found originally by Smith *et al.* [190] In this work, they have been characterized by employing second-order Moller-Pleset perturbation theory (MP2), and I changed the OH bond lengths and HOH angles to conform to the rigid geometries of Model1-3.

The electrostatic energies of the ten stationary points of dimer are determined to constrained space orbital variations (CSOV) [191, 192] decomposition results. Figure 45 shows the errors in intermolecular Coulomb energy for the ten water dimers using the three different models and the DPP water model. The DPP water model has smaller electrostatics energies than the CSOV models because of the lack of charge penetration. The electrostatic energies of Model1-3 of dimers 1-3 are almost the same as the CSOV results. However, for the stationary points of dimers 4 through 10, the electrostatic energies are not in good agreement with the CSOV results. Model3 over-estimates the electrostatic energy and gives values that are worse than those obtained with the DPP water model. Model2 shows better results than DPP water model, but the errors of the stationary point 7 and 9 are more than 1 kcal/mol. Model3 reproduces the electrostatic energies for the ten stationary points quite well. With this model, the errors for all ten stationary points are less than 1 kcal/mol.

B.4 CONCLUSION

I designed three different GEM models and implemented a fitting procedure to reproduce ESP using ABSs located at different sites. I limited the ABS sites to three, five, and six sites with s-type Gaussian functions. Also, I did preliminary calculations with the ten Smith dimers to see how well these models reproduce charge penetration.

Model1 shows the best electrostatic potential among the three models about the contour

diagram of the water monomer (Figure 42), but in the analysis with ten Smith water dimers, the electrostatic energies are over-estimated for seven out of the ten dimers. In contrast with Model2, Model3 does poorer at describing electrostatic potential of the water monomer than does the DPP water in the contour diagram of the water monomer (Figure 42). However, the electrostatic energies of the ten dimers calculated with Model3 are in very good agreement with the CSOV results.

For further research, I can focus on two directions. One is applying Model1 or Model3 to the DPP water model by adjusting the repulsive potential, and checking the relative energies of several water clusters. The second direction is designing other models to get better performance for the electrostatic potential of the water monomer and electrostatic energies of the ten Smith water dimers. By employing seven or eight sites or using p-type Gaussian functions instead of s-type Gaussian functions, I can generate more accurate fits to the high level *ab initio* results.

Table 8: Optimized coefficients (a.u.) and exponents of GTFs for the electron density and the dipole moments (debye) of Model1, Model2, and Model3, respectively.

		Coefficient			Exponent			Dipole
Model 1		O site	2H sites	2D sites	O site	2H sites	2D sites	
	GTF1	6.300	0.463	0.387	0.787	4.695	0.193	1.849
Model 2		M site	2H sites		M site	2H sites		
	GTF1	6.776	0.612		0.604	0.472		1.810
Model 3		M site	2H sites		M site	2H sites		
	GTF1	4.229	0.167		6.209	1.993		
	GTF2	2.583	0.427		0.397	0.435		1.895

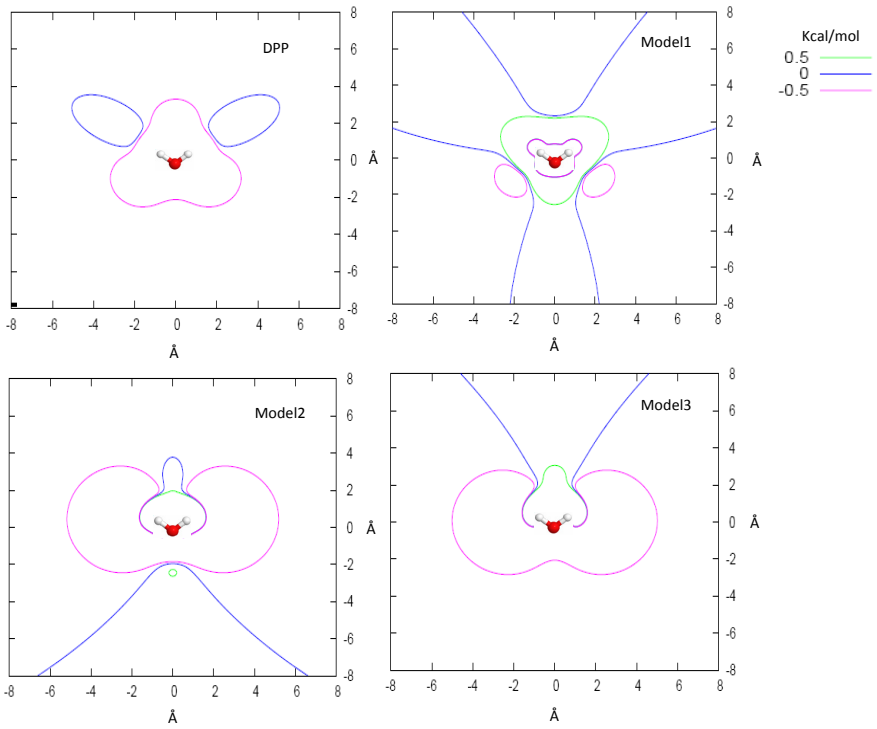

Figure 42: Electrostatic potential difference plots for the water dimer. In each case the plot gives the difference of the electrostatic potentials calculated using the model and the MP2/aug-cc-pVTZ method.

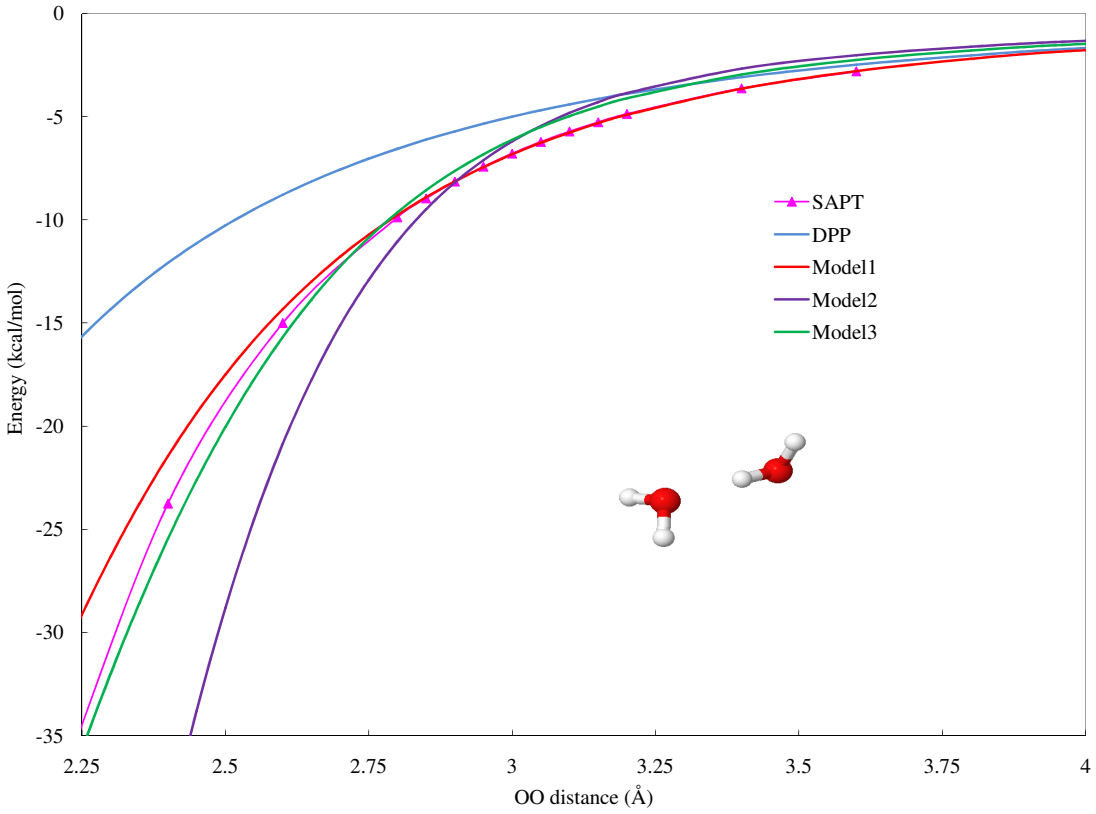

Figure 43: Electrostatic interaction energy for the water dimer, as a function of O-O distance, assuming rigid monomers and fixed flap angles.

(1) Non-plannar Open C_s

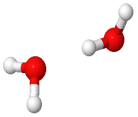

(2) Open C_1

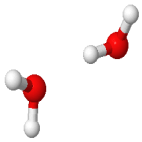

(3) Plannar Open C_s

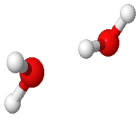

(4) Cyclic C_i

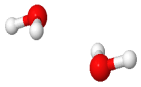

(5) Cyclic C_2

(6) Cyclic C_{2h}

(7) Triply Hydrogen Bonded C_s

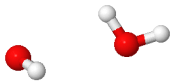

(8) Doubly Bifurcated C_{2h}

(9) Non-plannar Bifurcated C_{2h}

(10) Plannar Bifurcated C_{2v}

Figure 44: Ten different smith's water dimers.

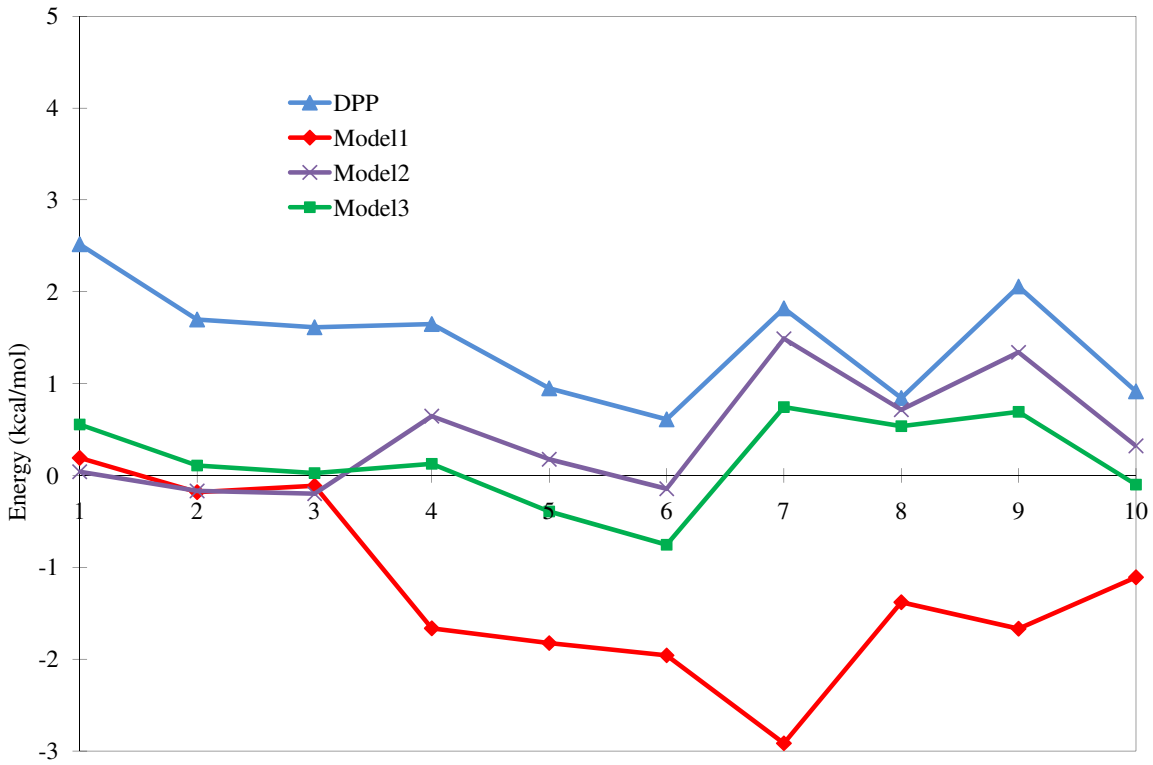

Figure 45: Errors in the electrostatic interaction energies for ten different Smith water dimers.

BIBLIOGRAPHY

[1] Kim, K. S.; Park, I.; Lee, S.; Cho, K.; Lee, J. Y.; Kim, J.; Joannopoulos, J. D. *Phy. Rev. Lett.* **1995,** *76,* 956.

[2] Paik, D. H.; Lee, I. R.; Yang, D. S.; Baskin, J. S.; Zewail, A. H. *Science* **2004,** *306,* 672.

[3] Hammer, N. I.; Shin, J. W.; Headrick, J. M.; Kiden, E. G.; Roscioli, J. R.; Weddle, G. H.; Johnson, M. A. *Science* **2004,** *306,* 675.

[4] Jordan, K. D. *Science* **2004,** *306,* 618.

[5] Borgis, D.; Rossky, P. J.; Turi, L. *J. Chem. Phys.* **2006,** *125,* 064501.

[6] Coe, J. V.; Lee, G. H.; Eaton, J. G.; Arnold, S. T.; Sarkas, H. W.; Bowen, K. H.; Ludewigt, C.; Haberland, H.; Worsnop, D. R. *J. Chem. Phys.* **1990,** *92,* 3980.

[7] Verlet, J. R. R.; Bragg, A. E.; Kammrath, A.; Cheshnovsky, O.; Neumark, D. M. *Science* **2005,** *307,* 93.

[8] Bragg, A. E.; Verlet, J. R. R.; Kammrath, A.; Cheshnovsky, O.; Neumark, D. M. *Science* **2004,** *306,* 669.

[9] Hammer, N. I.; Roscioli, J. R.; Johnson, M. A.; Myshakin, E. M.; Jordan, K. D. *J. Phys. Chem. A* **2005,** *109,* 11526.

[10] Hammer, N. I.; Roscioli, J. R.; Johnson, M. A. *J. Phys. Chem. A* **2005,** *109,* 7896.

[11] Diken, E. G.; Robertson, W. H.; Johnson, M. A. *J. Phys. Chem. A* **2004,** *108,* 64.

[12] Hammer, N. I.; Roscioli, J. R.; Bopp, J. C.; Headrick, J. M.; Johnson, M. A. *J. Chem. Phys.* **2005,** *123,* 244311.

[13] Roscioli, J. R.; Hammer, N. I.; Johnson, M. A.; Diri, K.; Jordan, K. D. *J. Chem. Phys.* **2008,** *128,* 104314.

[14] Roscioli, J. R.; Johnson, M. A. *J. Chem. Phys.* **2007,** *126,* 024307.

[15] Lee, H. M.; Suh, S. B.; Tarakeshwar, P.; Kim, K. S. *J. Chem. Phys.* **2005,** *122,* 044309.

[16] Suh, S. B.; Lee, H. M.; Kim, J.; Lee, J. Y.; ; Kim, K. S. *J. Chem. Phys.* **2000,** *113,* 5273.

[17] Lee, H. M.; Suh, S. B.; Kim, K. S. *J. Chem. Phys.* **2003,** *119,* 7685.

[18] Lee, H. M.; Lee, S.; Kim, K. S. *J. Chem. Phys.* **2003,** *119,* 187.

[19] Khan, A. *J. Mol. Struct.: THEOCHEM* **2008,** *850,* 144.

[20] Gutowski, M.; Skurski, P. *Recent Res. Dev. Phys. Chem.* **1999,** *3,* 245.

[21] Herbert, M. J.; Head-Gordon, M. *J. Phys. Chem. A* **2005,** *109,* 5217.

[22] Herbert, M. J.; Head-Gordon, M. *Phys. Chem. Chem. Phys.* **2006,** *8,* 68.

[23] Barnett, R. N.; Landman, U.; Cleveland, C. L.; Jortner, J. *J. Chem. Phys.* **1988,** *88,* 4429.

[24] Turi, L.; Sheu, W. S.; Rossky, P. J. *Science* **2005,** *309,* 914.

[25] Turi, L.; Madarasz, A.; Rossky, P. J. *J. Chem. Phys.* **2006,** *125,* 014308.

[26] Frigato, T.; VandeVondele, J.; Schmidt, B.; Schutte, C.; Jungwirth, P. *J. Phys. Chem. A* **2008,** *10,* 1021.

[27] Wang, F.; Jordan, K. D. *J. Chem. Phys.* **2002,** *116,* 6973.

[28] Wang, F.; Jordan, K. D. *J. Chem. Phys.* **2003,** *119,* 11645.

[29] Sommerfeld, T.; Jordan, K. D. *J. Phys. Chem. A* **2005,** *109,* 11531.

[30] Sommerfeld, T.; Jordan, K. D. *J. Am. Chem. Soc.* **2006,** *128,* 5828.

[31] Sommerfeld, T.; Gardner, S. D.; DeFusco, A.; Jordan, K. D. *J. Chem. Phys.* **2006,** *125,* 174301.

[32] DeFusco, A.; Sommerfeld, T.; Jordan, K. D. *Chem. Phys. Lett.* **2008,** *455,* 135.

[33] Sommerfeld, T.; DeFusco, A.; Jordan, K. D. *J. Phys. Chem. A,* **2008,** *112,* 11021.

[34] Wales, D. J.; Hodges, M. P. *Chem. Phys. Letters* **1998,** *286,* 65.

[35] Ren, P.; Ponder, J. W. *J. Phys. Chem. B* **2003,** *107,* 5933.

[36] Dang, L. X.; Chang, T.-M. *J. Chem. Phys.* **1997,** *106,* 8149.

[37] Bumham, C. J.; Li, J. C.; Xantheas, S. S. *J. Chem. Phys.* **2002,** *116,* 1500.

[38] Hartke, B. *Phys. Chem. Chem. Phys* **2003,** *5,* 275.

[39] Xantheas, S. S.; Apra, E. *J. Chem. Phys* **2004,** *120,* 823.

[40] Fanourgakis, G. S.; Xantheas, S. S. *J. Phys. Chem. A* **2006,** *110,* 4100.

[41] Belair, S. D.; Francisco, J. S. *Phys. Rev. A 67* **2003,** *67,* 063206.

[42] Tsai, C. J.; Jordan, K. D. *J. Chem. Phys.* **1993,** *99,* 6957.

[43] Pedulla, J. M.; Jordan, K. D. *Chem. Phys. Lett.* **1998,** *291,* 78.

[44] Tsai, C. J.; Jordan, K. D. *J. Phys. Chem.* **1993,** *97,* 5208.

[45] Kim, J.; Majumdar, D.; Lee, H. M.; Kim, K. S. *J. Chem. Phys.* **1999,** *110,* 9128.

[46] Maheshwary, S.; Patel, N.; Sathyamurthy, N.; Kulkarni, A. D.; Gadre, S. R. *J. Phys. Chem. A* **2001,** *105,* 10525.

[47] Pedulla, J. M.; Jordan, K. D. *Chem. Phys.* **1998,** *239,* 593.

[48] Tharrington, A. N.; Jordan, K. D. *J. Phys. Chem. A* **2003,** *107,* 7380.

[49] Nigra, P.; Carignano, M. A.; Kais, S. *J. Chem. Phys.* **2001,** *115,* 2621.

[50] Schmitt, U. W.; Voth, G. A. *J. Chem. Phys.* **1999,** *111,* 9361.

[51] Mark, D.; mark E. Tuckerman,; Hutter, J.; Parrinello, M. *Nature* **1999,** *397,* 601.

[52] Shin, J.-W.; Hammer, N. I.; Diken, E. G.; Johnson, M. A.; Walters, R. S.; Jaeger, T. D.; Duncan, M. A.; Christie, R. A.; Jordan, K. D. *science* **2004,** *304,* 1137.

[53] Brudermann, J.; Buck, U.; Buch, V. *J. Phys. Chem. A* **2002,** *106,* 453.

[54] Miller, Y.; Fredj, E.; Harvey, J. N.; Gerber, R. B. *J. Phys. Chem. A* **2004,** *108,* 4405.

[55] Iyengar, S. S. *J. Chem. Phys.* **2007,** *126,* 216101.

[56] Iyengar, S. S.; Petersen, M. K.; Day, T.; Burnham, C. J.; Teige, V. E.; Voth, G. A. *J. Chem. Phys.* **2005,** *123,* 084309.

[57] Yu, H.; Cui, Q. *J. Chem. Phys.* **2007,** *127,* 234504.

[58] Jeffrey, G. A.; Saenger, W. *Hydrogen Bonding in Biological Structures;* Berlin: Springer-Verlag, 1991.

[59] Nagle, J. F.; Morowitz, H. J. *Proc. Natl. Acad. Sci* **1978,** *75,* 298.

[60] Drukker, K.; de Leeuw, S. W.; Hammes-Schiffer, S. *J. Chem. Phys.* **1998,** *108,* 6799.

[61] Lee, Y.; Krauss, M. *J. Mol. Struct.* **2004,** *700,* 243.

[62] Kreuer, K. D.; Paddison, S.; Spohr, E.; Schuster, M. *Chem. Rev.* **2004,** *104,* 4637.

[63] Swanson, J.; Maupin, C.; Chen, H.; Petersen, M.; Xu, J.; Wu, Y.; Voth, G. *J. Phys. Chem. B* **2007,** *111,* 4300.

[64] Wayne, R. P. *Chemistry of Atomospheres;* New York: Oxford University Press, 1991.

[65] Wang, F.; Jordan, K. D. *J. Chem. Phys.* **2001,** *114,* 10717.

[66] DeFusco, A.; Schofield, D.; Jordan, K. D. *Mol. Phys.* **2007,** *105,* 2681.

[67] Wales, D. J.; Scheraga, H. A. *Science* **1999,** *285,* 1368.

[68] Doye, J. P.; Wales, D. J. *Phys. Rev. Letters* **1998,** *80,* 1357.

[69] Henkelman, G.; Uberuaga, B. P.; Jónsson, H. *J. Chem. Phys.* **2000,** *113,* 9978.

[70] Trygubenko, S. A.; Wales, D. J. *J. Chem. Phys.* **2004,** *120,* 2082.

[71] Hilderbrandt, R. L. *Comput. Chem. (Oxford)* **1977,** *1,* 179.

[72] Cerjan, C. J.; Miller, W. H. *J. Chem. Phys.* **1981,** *75,* 2800.

[73] Becker, O. M.; Karplus, M. *J. Chem. Phys.* **1997,** *106,* 1495.

[74] Wales, D. J.; Miller, M. A.; Walsh, T. R. *Nature* **1998,** *394,* 758.

[75] Wales, D. J. *Energy Landscapes;* Cambridge University Press: Cambridge, 2003.

[76] Beck, M.; Jackle, A.; Worth, G.; Meyer, H.-D. *Physics Reports* **2000,** *324,* 1.

[77] Lill, J. V.; Parker, G. A.; Light, J. C. *Chem. Phys. Lett.* **1982,** *89,* 483.

[78] Light, J. C.; Hamilton, I. P.; Lill, J. V. *J. Chem. Phys.* **1985,** *82,* 1400.

[79] Baye, D.; Heenen, P.-H. *J. Phys. A* **1986,** *19,* 2041.

[80] Vincke, M.; Malegat, L.; Baye, D. *J. Phys. B* **1993,** *26,* 811.

[81] Szalay, V. *J. Chem. Phys.* **1993,** *99,* 1978.

[82] Szalay, V.; Nemes, L. *Chem. Phys. Lett.* **1994,** *231,* 225.

[83] Baye, D.; Hesse, M.; Vincke, M. *Phys. Rev. E* **2002,** *65,* 026701.

[84] Littlejohn, R. G.; Cargo, M.; Jr., T. C.; Mithell, K. A.; Poirier, B. *J. Chem. Phys.* **2002,** *116,* 8691.

[85] Littlejohn, R. G.; Cargo, M. *J. Chem. Phys.* **2002,** *116,* 7350.

[86] Schneider, B. I.; Nygaard, N. *Phys. Rev. E* **2004,** *70,* 056706.

[87] Buisseret, F.; Semay, C. *Phys. Rev. E* **2005,** *71,* 026705.

[88] Xiao, Y.; Poirier, B. *J. Theoret. Comput. Chem.* **2007,** *6,* 309.

[89] Rayson, M. J. *Phys. Rev. E* **2007,** *76,* 026704.

[90] Yan, D.; Peng, L.-Y.; Gong, Q. *Phys. Rev. E* **2009,** *79,* 036710.

[91] Elster, M.; Porezag, D.; Jungnickel, G.; Elsner, J.; M.Haugk,; Frauenheim, T.; Suhai, S.; Seifert, G. *Phys. Rev. B* **1998,** *58,* 7260.

[92] Elstner, M.; Hobza, P.; Frauenheim, T.; Suhai, S.; Kaxiras, E. *J. Chem. Phys.* **2001,** *114,* 5149.

[93] Elstner, M.; Cui, Q.; Munih, P.; Kaxiras, E.; Frauenheim, T.; Karplus, M. *J. Com. Chem.* **2002,** *24,* 565.

[94] Lin, C. S.; Zhang, R. Q.; Lee, S. T.; Elstner, M.; Frauenheim, T.; Wan, L. J. *J. Phys. Chem. B* **2005,** *109,* 14183.

[95] Kruger, T.; Elstner, M.; Schiffels, P.; Frauenheim, T. *J. Chem. Phys.* **2005,** *122,* 114110-1.

[96] Zhechkov, L.; Heine, T.; Patchkovskii, S.; Seifert, G.; Duarte, H. A. *J. Chem. Theory Comput.* **2005,** *1,* 841.

[97] Hu, H.; Lu, Z.; Elstner, M.; Hermans, J.; Yang, W. *J. Phys. Chem. A* **2007,** *111,* 5685.

[98] Riccardi, D.; Schaefer, P.; Yang, Y.; Yu, H.; Ghosh, N.; Prat-Resina, X.; Konig, P.; Li, G.; Xu, D.; Guo, H.; Elstner, M.; Cui, Q. *J. Phys. Chem. B* **2006,** *110,* 6458.

[99] Elstner, M. *Theor. Chem. Acc.* **2006,** *116,* 316.

[100] Becke, A. D. *J. Chem. Phys.* **1993,** *98,* 5648.

[101] Choi, T. H.; Jordan, K. D. *Chem. Phys. Lett.* **2008,** *464,* 139.

[102] Haberland, H.; Schindler, H. G.; Worsnop, D. R. *ber. Bunsen-Ges. Phys. Chem.* **1984,** *88,* 270.

[103] Lee, M. H.; Suh, B. S.; Kim, K. S. *J. Chem. Phys.* **2003,** *118,* 9981.

[104] Schnitker, J.; Rossky, P. J. *J. Chem. Phys.* **1987,** *86,* 3462.

[105] Szabo, A.; Ostlund, N. S. *MODERN QUANTUM CHEMISTRY;* McGraw-Hall Publishing Company: New York, 1989.

[106] Pulay, P. *Mol. Phys.* **1969,** *17,* 197.

[107] Meyer, W.; Pulay, P. *J. Chem. Phys.* **1972,** *56,* 2109.

[108] Goldstein, H. *Classical Mechanics;* Addison-Wesley: Massachusetts, 1980.

[109] Choi, T. H.; Jordan, K. D. *Chem. Phys. Lett.* **2009,** *475,* 293.

[110] Haberland, H.; Ludewigt, C.; Schindler, H. G.; Worsnop, D. R. *J. Chem. Phys.* **1984,** *81,* 3742.

[111] Noga, J.; Bartlett, R. J. *J. Chem. Phys.* **1987,** *86,* 7041.

[112] Raghavachari, K.; Trucks, G. W.; Pople, J. A.; Head-Gordon, M. *Chem. Phys. lett.* **1989,** *157,* 479.

[113] Møller, C.; Plesset, M. S. *Phys. Rev.* **1934,** *46,* 618.

[114] Doye, J. P.; Wales, D. J. *Phys. Rev. B* **1999,** *59,* 2292.

[115] James, T.; Wales, D. J. *J. Chem. Phys.* **2005,** *122,* 134306.

[116] Byrd, R. H.; Lu, P.; Nocedal, J. *SIAM J. Sci. Comput. (USA)* **1995,** *16,* 1190.

[117] Simons, J.; Jørgenson, P.; Taylor, H.; Ozment, J. *J. Chem. Phys.* **1983,** *87,* 2754.

[118] Munro, L. J.; Wales, D. J. *Phys. Rev. B* **1999,** *59,* 3969.

[119] Wales, D. J. "`OPTIM`: a program for optimising geometries and calculating pathways", `http://www-wales.ch.cam.ac.uk/software.html`.

[120] Born, M.; Oppenheimer, R. *Ann. Phys. (Leipzig)* **1927,** *84,* 457.

[121] Johnson, M. page in preparation.

[122] Lee, H. M.; Lee, S.; Kim, K. S. *J. Chem. Phys.* **2003,** *118,* 9981.

[123] Carignano, M. A.; Mohammad, A.; Kais, S. *J. Phys. Chem. A* **2009,** *113,* 10886.

[124] Lee, H. M.; Kim, K. S. *J. Chem. Phys.* **2002,** *117,* 706.

[125] Wallqvist, A.; Thirumalai, D.; Berne, B. J. *J. Chem. Phys.* **1986,** *85,* 1583.

[126] Wallqvist, A.; Thirumalai, D.; Berne, B. J. *J. Chem. Phys.* **1987,** *86,* 6404.

[127] Turi, L.; Borgis, D. *J. Chem. Phys.* **2002,** *117,* 6186.

[128] Jacobson, L. D.; Williams, C. F.; Herbert, J. M. *J. Chem. Phys.* **2009,** *130,* 124115.

[129] http://www.openmp.org,.

[130] Thole, B. T. *Chem. Phys.* **1981,** *59,* 341.

[131] Lanczos, C. J. *Natl. Bur. Stand.* **1950,** *45,* 255.

[132] Lehoucq, R. B.; Sorensen, D. C.; Yang, C. *ARPACK Users' Guide: Solution of Large-Scale Eigenvalue Problems with Implicitly Restarted Arnoldi Methods;* : , 1997.

[133] http://www.caam.rice.edu/software/ARPACK/,.

[134] Wales, D. J.; Doye, J. P. *J. Phys. Chem. A* **1997,** *101,* 5111.

[135] Doye, J. P.; Wales, D. J. *J. Chem. Soc., Faraday Trans.* **1997,** *93,* 4233.

[136] Doye, J. P.; Wales, D. J. *New J. Chem.* **1998,** 733.

[137] Doye, J. P.; Wales, D. J. *J. Chem. Phys.* **1996,** *105,* 8428.

[138] Li, Z.; Scheraga, H. A. *Proc. Natl. Acad. Sci. USA* **1987,** *84,* 6611.

[139] Deaven, D. M.; Tit, N.; Morris, J. R.; Ho, K. M. *Chem. Phys. Letters* **1996,** *256,* 195.

[140] Doye, J. P.; Wales, D. J.; Miller, M. A. *J. Chem. Phys.* **1998,** *109,* 8143.

[141] Munro, L. J.; Tharrington, A.; Jordan, K. D. *Com. Phys. Comm.* **2002,** *145,* 1-23.

[142] Liu, H.; Jordan, K. D. *J. Phys. Chem.* **2005,** *109,* 5203.

[143] Kone, A.; Kofke, D. A. *J. Chem. Phys.* **2005,** *122,* 206101.

[144] Parr, R. G.; Pearson, R. G. *J. Am. Chem. Soc.* **1983,** *105,* 7512.

[145] Eigen, M.; Maeyer, L. *Proc. R. Roc. London* **1958,** *247,* 505.

[146] Eigen, M. *Angew. Chem. Int. Ed. Engl.* **1964,** *3,* 1.

[147] Schuster, P.; Zundel, G.; Sandorfy, C. *Recent Developments in Theory and Experiments. II. Structure and Spectroscopy;* North-Holland, Amsterdam: , 1976.

[148] Zundel, G.; Metzger, H. Z. *Phys. Chem.* **1968,** *58,* 225.

[149] Yang, X.; Jr., A. W. C. *J. Am. Chem. Soc.* **1989,** *111,* 6845.

[150] Christie,; Jordan, K. D. *J. Phys. Chem. B* **2002,** *106,* 8376.

[151] Christie,; Jordan, K. D. *J. Phys. Chem. A* **2001,** *105,* 7551.

[152] Tulub, A. A. *J. Chem. Phys.* **2004,** *120,* 1217.

[153] Jiang, J.-C.; Wang, Y.-S.; Chang, H.-C.; Lin, S. H.; Lee, Y. T.; Niedner-Schatteburg, G.; ; Chang, H.-C. *J. Am. Chem. Soc.* **2000,** 1398.

[154] Shevkunov, S. V.; Vegiri, A. *J. Chem. Phys.* **1999,** *111,* 9303.

[155] Ojamae, L.; Shavitt, I.; Singer, S. J. *J. Chem. Phys.* **1998,** *109,* 5547.

[156] Kozack, R. E.; Jordan, P. C. *J. Chem. Phys.* **1992,** *96,* 3131.

[157] Kozack, R. E.; Jordan, P. C. *J. Chem. Phys.* **1993,** *99,* 2978.

[158] Christie,; Jordan, K. D. *J. Phys. Chem. B* **2002,** *106,* 8376.

[159] Christie,; Jordan, K. D. *J. Phys. Chem. A* **2001,** *105,* 7551.

[160] Schmitt, U. W.; Voth, G. A. *J. Phys. Chem. B* **1998,** *102,* 5547.

[161] James, T.; Wales, D. J. *J. Chem. Phys.* **2005,** *122,* 134306.

[162] Kumar, R.; Christie, R. A.; Jordan, K. D. *J. Phys. Chem. A* **2009,** *113,* 4111.

[163] Wang, F.-F.; Jenness, G.; Al-Saidi, W.; Jordan, K. D. *in preparation* .

[164] Santra, B.; Michaelides, A.; Scheffler, M. *J. Chem. Phys.* **2007,** *127,* 184104.

[165] Kelkkanen, A. K.; Lundqvist, B. I.; Nørskov, J. K. *J. Chem. Phys.* **2009,** *131,* 046102.

[166] Baboul, A. G.; Curtiss, L. A.; Redifern, P. C.; Raghavachari, K. *J. Chem. Phys.* **1999,** *110,* 7650.

[167] Curtiss, L. A.; Raghavachari, K.; Redifern, P.; Rassolov, V.; Pople, J. A. *J. Chem. Phys.* **1998,** *109,* 7764.

[168] Huang, X.; Braaams, B. J.; Bowman, J. M. *J. Chem. Phys.* **2005,** *122,* 044308.

[169] Weigend, F.; Häser, M. *Theor. Chem. Acc.* **1997,** *97,* 331.

[170] Kumar, R.; Wang, F.-F.; Jenness, G. R.; Jordan, K. D. *J. Chem. Phys.* **2010,** *132,* 014309.

[171] Baquero, E. E.; III, W. H. J.; Choi, T. H.; Jordan, K. D.; Zwier, T. S. *J. Phys. Chem. A* **2008,** *112,* 1115.

[172] Carney, J. R.; Zwier, T. S. *J. Phys.Chem. A* **2000,** *104,* 8677.

[173] Ahlrichs, R.; Bär, M.; Häser, M.; Horn, H.; Kölmel, C. *Chem. Phys. Lett.* **1989,** *162,* 165.

[174] Jorgensen, W. L.; Chandrasekhar, J.; Madure, J. D.; Impey, R. W.; Klein, M. L. *J. Chem. Phys.* **1983,** *79,* 926.

[175] Stone, A.; Alderton, M. *Mol. Phys.* **1985,** *56,* 1047.

[176] Freitag, M. A.; Gordon, M. S.; Jensen, J. H.; Stevens, W. J. *J. Chem. Phys.* **2000,** *112,* 7300.

[177] Piquemal, J. P.; Gresh, N.; Giessner-Prettre, C. *J. Phys. Chem. A* **2005,** *107,* 10353.

[178] Gresh, N.; Piquemal, J. P.; Krauss, M. *J. Comput. Chem.* **2005,** *26,* 1113.

[179] Cisneros, G. A.; im Tholander, S. N.; Parisel, O.; Darden, T. A.; Elking, D.; Perera, L.; Piquemal, J.-P. *Int. J. Quantum Chem.* **2008,** *108,* 1905.

[180] Cisneros, G. A.; Piquemal, J.-P.; Darden, T. A. *J. Chem. Phys.* **2006,** *125,* 184101.

[181] Cisneros, G. A.; Piquemal, J.-P.; Darden, T. A. *J. Chem. Phys.* **2005,** *123,* 044109.

[182] Cisneros, G. A.; Piquemal, J.-P.; Darden, T. A. *J. Phys. Chem. B* **2006,** *110,* 13682.

[183] Cisneros, G. A.; Elking, D.; Piquemal, J.-P.; Darden, T. A. *J. Phys. Chem. A* **2007,** *111,* 12049.

[184] Mas, E. M.; Bukowski, R.; Szalewicz, K.; Groenenboom, G. C.; Wormer, P. E. S.; van der Avoird, A. *J. Chem. Phys.* **2000,** *113,* 6687.

[185] Hu, H.; Lu, Z.; Yang, W. *J. Chem. Theo. Comput.* **2007,** *3,* 1004.

[186] Lovas, F. J. *J. Phys. Chem. Ref. Data* **1978,** *7,* 1445.

[187] Jenness, G.; DeFusco, A.; Cui, J.; Jordan, K. D. *unpublished* .

[188] Rybak, S.; Jeziorski, B.; Szalewicz, K. *J. Chem. Phys.* **1991,** *95,* 6576.

[189] Mas, E. M.; Szalewicz, K.; Bukowski, R.; Jeziorski, B. *J. Chem. Phys.* **1997,** *107,* 4207.

[190] Smith, B. J.; Swanton, D. J.; Pople, J. A.; Schaefer, H. F.; Radom, L. *J. Chem. Phys.* **1990,** *92,* 1240.

[191] Bagus, P. S.; Illas, F. J. *J. Chem. Phys.* **1992,** *96,* 8962.

[192] Piquemal, J.-P.; Marquez, A.; Parisel, O.; Giessner-Prettre, C. *J. Comput. Chem.* **2005,** *26,* 1052.